

Galactic Centre observations with local mm-telescope arrays

INAUGURAL-DISSERTATION

zur
Erlangung des Doktorgrades
der Mathematisch-Naturwissenschaftlichen Fakultät
der Universität zu Köln



vorgelegt von

Devaky Kunneriath
aus Ernakulam, Indien

Köln 2010

Berichterstatter:

Prof. Dr. Andreas Eckart
Prof. Dr. J. Anton Zensus

Tag der mündlichen Prüfung: 18. Nov 2010

Abstract

Radio interferometry observations are a powerful tool to study the central regions of the Galactic centre (GC). High angular resolution observations at millimetre wavelengths can disentangle the emission of Sgr A* from the thermal emission of the circum nuclear disk (CND) and the mini-spiral surrounding it. In this thesis I present the results of radio interferometric observations of the GC region with local millimetre-telescope arrays such as CARMA and ATCA, supplemented by observations in the infrared (IR) with ESO's VLT telescopes. My goal is to analyse the emission mechanisms present in the central few parsecs of the GC region, in particular the extended thermal emission of the ionized gas and dust of the mini-spiral region and the non-thermal emission of Sagittarius A* (Sgr A*), the radio source associated with the supermassive black hole (SMBH) at the GC.

Observations were carried out in March and April 2009 at 1.3 and 3 mm with the mm telescope array CARMA in California, in June 2006 with the mid-infrared (MIR) instrument VISIR at ESO's VLT, and the NIR Br γ in August 2009 with VLT NACO. I present high angular resolution continuum maps of the GC at 3 and 1.3 mm and the highest resolution spectral index map obtained at these wavelengths. I obtain a spectral index of 0.5 ± 0.25 for Sgr A*, indicating an inverted synchrotron spectrum and a mixture of negative and positive values in the extended emission of the minispiral, including the thermal free-free emission from the ionized gas, and a possible contribution of dust at 1.3 mm. I infer the physical properties of the dust and gas in the mini-spiral by comparing the radio continuum maps to the MIR continuum map, and the Br γ line emission map in the NIR. An extinction map at NIR wavelengths for the mini-spiral region, showing extinctions ranging from 1.8-3 magnitudes, was also produced.

To study the flaring activity of Sgr A*, global coordinated multiwavelength campaigns were carried out in 2007 and 2008 using ESO's VLT and the mm telescope arrays CARMA, ATCA, and the 30 m IRAM telescope in Spain, which detected four flares in the NIR, of which three were covered later by the mm data. I develop a new method for obtaining concatenated light curves of the compact mm-source Sgr A* from single dish telescopes and interferometers in the presence of significant flux density contributions

from an extended and only partially resolved source, and model the observed flares in the NIR and mm using an adiabatic expansion model involving synchrotron source components. I derive physical quantities such as expansion velocities ranging from $v_{\text{exp}} \sim 0.005c - 0.017c$, source sizes of about one Schwarzschild radius, turnover frequencies of a few THz, flux densities of a few Janskys, and spectral indices of $\alpha=0.6$ to 1.3. These parameters suggest either a bulk motion of the adiabatically expanding source components greater than v_{exp} or a confinement of expanding material within a corona or disk in the immediate surroundings of Sgr A*.

Zusammenfassung

Radiointerferometrische Beobachtungen sind eine ausgezeichnete Methode zum Studium der zentralen Regionen des Galaktischen Zentrums (GC). Beobachtungen mit hoher Winkelauflösung im mm-Wellenlängenbereich ermöglichen die Unterscheidung der Emission von Sgr A* von der thermischen Emission der Zirkumnuklearen Scheibe und der Minispirale, welche Sgr A* umgeben. In dieser Arbeit stelle ich die Ergebnisse von radiointerferometrischen Beobachtungen des GC vor, die mit Millimeterteleskopanlagen wie CARMA und ATCA durchgeführt und für den Infrarotbereich durch Beobachtung mit den VLT Teleskopen der ESO ergänzt wurden. Mein Ziel ist die Analyse der bestehenden Emissionsmechanismen im Umkreis weniger Parsec um das Zentrum der GC-Region, insbesondere der ausgedehnten thermale Emission ionisierten Gases und Staubes im Bereich der Minispirale und der nichtthermische Emission von Sagittarius A* (Sgr A*), der Radioquelle, die dem supermassiven schwarzen Loch (SMBH) im GC zugeordnet wird.

Die Beobachtungen wurden im März und April 2009 bei 1,3 und 3,0 mm mit CARMA in Kalifornien, im Juni 2006 mit dem MIR Instrument VISIR am VLT der ESO und im NIR Br γ im August 2009 mit VLT NACO durchgeführt. Ich zeige hochaufgelöste Kontinuumsabbildungen des GC bei 3,0 und 1,3 mm und höchstauflöste Abbildungen des Spektralindex für diesen Wellenlängenbereich. Ich erhalte einen Spektralindex von 0.5 ± 0.25 for Sgr A*, der auf ein invertiertes Synchrotronpektrum hinweist, und sowohl negative als auch positiven Werten in der ausgedehnten Emission der Minispirale, die thermale frei-frei-Strahlung des ionisierten Gases und einen möglichen Beitrag vom Staub bei 1,3 mm beinhaltet. Durch den Vergleich der Karten des Radiokontinuums mit denen des mittleren Infrarotbereichs (MIR) sowie denen der Br γ Linienemission bei nahinfraroten (NIR) Wellenlängen leite ich die physikalischen Eigenschaften des Staubes und des Gases in der Minispirale ab. Es wurde ebenfalls eine Extinktionskarte für die Region der Minispirale bei NIR Wellenlängen erstellt. Sie zeigt, daß die Extinktion zwischen 1,8 bis 3 Magnituden liegt.

Um die Flare-Aktivität von Sgr A* zu studieren, wurden 2007 und 2008 koordinierte weltweite Beobachtungskampagnen bei verschiedenen Wellen-

längen durchgeführt. Verwendet wurden dafür das VLT der ESO, die mm-Teleskopanordnungen CARMA, ATCA und das 30 m Teleskop IRAM in Spanien. Sie detektierten vier Flares im NIR-Bereich, von denen drei mit Verzögerung auch in den mm-Daten wiederzufinden waren. Ich entwickle hier für Sgr A* eine neue Methode zur Verknüpfung von einzelnen Lichtkurven, die von verschiedenen Interferometern und Einzelteleskopen stammen und für die in unterschiedlichem Maße der konstanten Flußbeitrag der ausgedehnte und nur teilweise aufgelöste Umgebung von der variablen Emission getrennt werden muß. Des Weiteren interpretiere ich die beobachteten Flares im NIR und im mm-Bereich im Rahmen eines Modells für die adiabatischen Expansion von Synchrotronquellkomponenten. Für die Expansionsgeschwindigkeit erhalte ich Werte wie $v_{\text{exp}} \sim 0,005c - 0,017c$, die Quellgröße beträgt etwa einen Schwarzschildradius, die Turnover-Frequenz liegt bei einigen wenigen THz, die Flußdichten bei wenigen Jansky und die Spektralindizes reichen von $\alpha = 0,6$ bis $1,3$. Diese Parameter legen den Schluß nahe, daß sich entweder die adiabatisch expandierenden Quellkomponenten kohärent mit einer Geschwindigkeit bewegen, die größer ist als v_{exp} , oder daß die expandierende Materie im Inneren einer Korona oder Scheibe in der direkten Umgebung von Sgr A* eingeschlossen ist.

Contents

1	Introduction	9
1.1	The Galactic Centre	9
1.1.1	The Interstellar Medium	10
1.1.2	Nuclear Star Cluster	15
1.1.3	Sgr A*	16
1.1.4	Flaring activity of Sgr A*	18
1.2	This thesis	20
2	Background	21
2.1	Radio Astronomy	21
2.2	Emission processes	22
2.2.1	Continuum emission	22
2.2.2	Line emission	26
2.3	Radio telescopes	26

2.4	Interferometry	27
2.5	Telescopes and Instruments used	32
2.5.1	CARMA	32
2.5.2	ATCA	33
2.5.3	IRAM 30 m telescope	34
2.5.4	VLT	34
3	The Central Parsec of the galaxy	37
3.1	Observations and Data Reduction	37
3.1.1	mm observations	37
3.1.2	MIR observations	39
3.1.3	NIR Brackett γ	41
3.2	Results and analysis	43
3.2.1	Radio 3 mm and 1.3 mm maps	44
3.2.2	Spectral index	47
3.2.3	MIR map	50
3.2.3.1	Dust to gas ratio	52
3.2.4	NIR Brackett γ map	53

4 Flaring Model of Sgr A*	57
4.1 Modelling	57
4.1.1 Synchrotron self-Compton theory	58
4.1.2 Relativistic spot/disk modelling of NIR flares	59
4.1.2.1 Multi-component disk model	59
4.1.3 Adiabatic expansion modelling of the mm/sub-mm emission	61
4.1.3.1 Adiabatically expanding source components	61
5 Modelling of May 2007 and 2008 flares	65
5.1 Observations and data reduction	66
5.1.1 The mm data	66
5.1.2 The NIR data	72
5.2 Results and Analysis	77
5.2.0.1 Adiabatic expansion modelling	78
5.2.1 Flare events	79
5.2.1.1 The 15 May 2007 flare event	79
5.2.1.2 The 17 May 2007 flare event	83
5.2.1.3 The 19 May 2007 flare event	88
5.2.1.4 The 26 May 2008 flare event	91
5.3 Flare analysis	94

6 Summary and conclusions	95
6.1 Discussion and Outlook	96
6.1.1 Mini-spiral region	96
6.1.2 Flares of Sgr A*	97
Bibliography	106
List of Figures	109
List of Tables	111
List of Acronyms	113
Acknowledgements	115
Erklärung	117

Chapter 1

Introduction

1.1 The Galactic Centre

The theory that the centre of our galaxy, the Milky Way, and most other galactic nuclei may contain a massive black hole, and the suggestion to search for this compact synchrotron source using long baseline interferometry was first put forward by Lynden-Bell (1969) and Lynden-Bell & Rees (1971). Downes & Martin (1971) and Ekers et al. (1975) performed the first full synthesis radio observations of the Galactic Centre (GC) region and were able to resolve the emission from the region into two components, a thermal component named Sgr A West, and a non-thermal source Sgr A East, with characteristics similar to galactic supernova remnants. However, the first detection of Sagittarius A* (Sgr A*), the compact non-thermal radio source associated with the GC, was made by Balick & Brown (1974) using the Green Bank Green Bank 35 km radio interferometer (Fig. 1.1).

At a distance of only ~ 8.5 kpc (Reid 1993; Eisenhauer et al. 2005; Ghez et al. 2008) from the Solar System, Sgr A* is the closest galactic nucleus to us, making it an ideal candidate to study the physics of galactic nuclei at high spatial resolutions. Since its discovery there have been several advances in the study of the GC with convincing evidence (in the form of stellar orbits) being found for the presence of a supermassive black hole (SMBH)

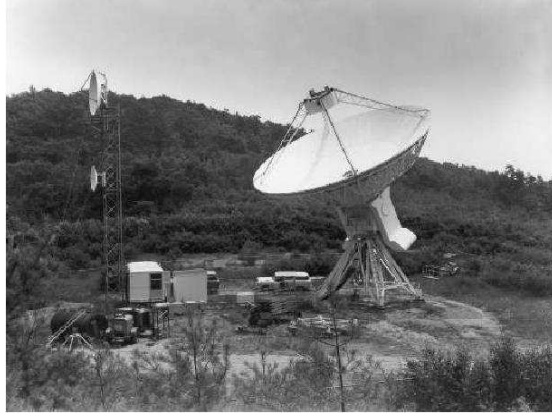


Figure 1.1: The 45 foot (~ 14 m) telescope used to make the discovery of Sgr A* (Balick & Brown 1974) at Huntersville, West Virginia. Taken from Goss et al. (2003).

of mass $\sim 4 \times 10^6 M_{\odot}$ at the position of Sgr A* (Eckart & Genzel 1996; Genzel et al. 1997, 2000; Ghez et al. 1998, 2000, 2004b,a, 2005; Eckart et al. 2002; Schödel et al. 2002, 2003; Eisenhauer et al. 2003, 2005; Gillessen et al. 2009; Ghez et al. 2009). The GC region consists of the interstellar medium (ISM) in the circum nuclear Disk (CND), the nuclear stellar cluster and the radio and infrared source Sgr A* associated with the SMBH.

The following sections describe the main components of the galactic centre region. The last part of this chapter describes in brief the work contained in this thesis and its structure.

1.1.1 The Interstellar Medium

Figure 1.2 shows a schematic diagram of the GC region as seen in the plane of the sky. The interstellar medium in this region is mostly distributed in the giant molecular clouds, but there is a concentration of dense heated gas in the inner ~ 10 parsecs of the GC, in the form of Sgr A East, Sgr A West and the circum nuclear disk (CND). Sgr A*, Sgr A West, which contains the mini-spiral, and the CND are placed inside Sgr A East, as can be seen from the figure (see also Fig.1.3).

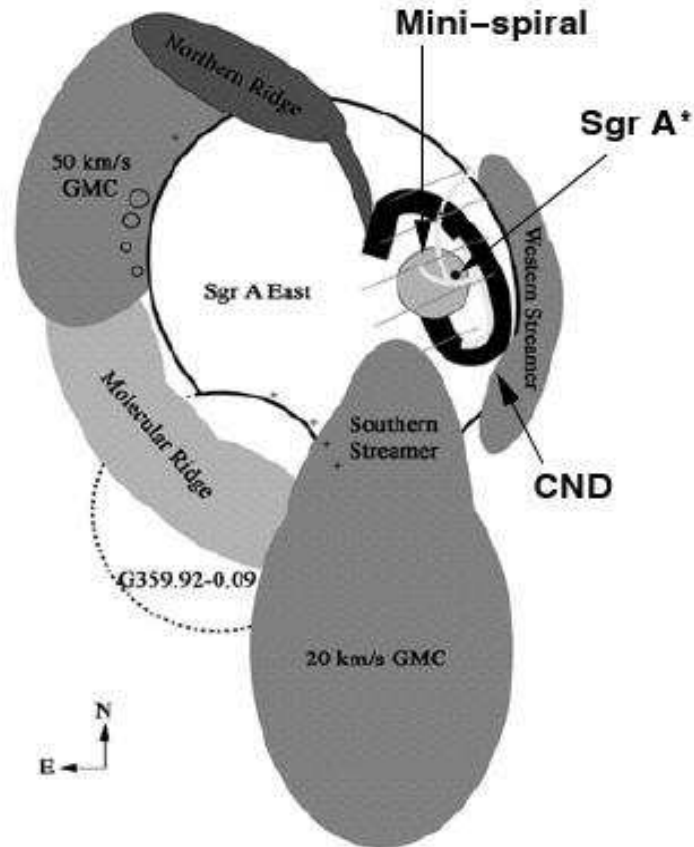


Figure 1.2: Schematic view of the Galactic Centre in the plane of the sky (Herrnstein & Ho 2005).

One of the first full synthesis radio maps of the GC at 5 GHz resolved the region into two components, Sgr A West, a thermal component with a flat spectrum, and Sgr A East, a non-thermal source with characteristics similar to galactic supernova remnants, and evidence of a shell structure (Ekers et al. 1975, 1983) (Fig. 1.3). Later interferometric observations (performed with the VLA), also at 5 GHz (Brown et al. 1981), found peaks in the radio brightness distribution at the same positions as the thermal peaks at $10\ \mu\text{m}$ reported by Becklin & Neugebauer (1975) and Becklin et al. (1978). These

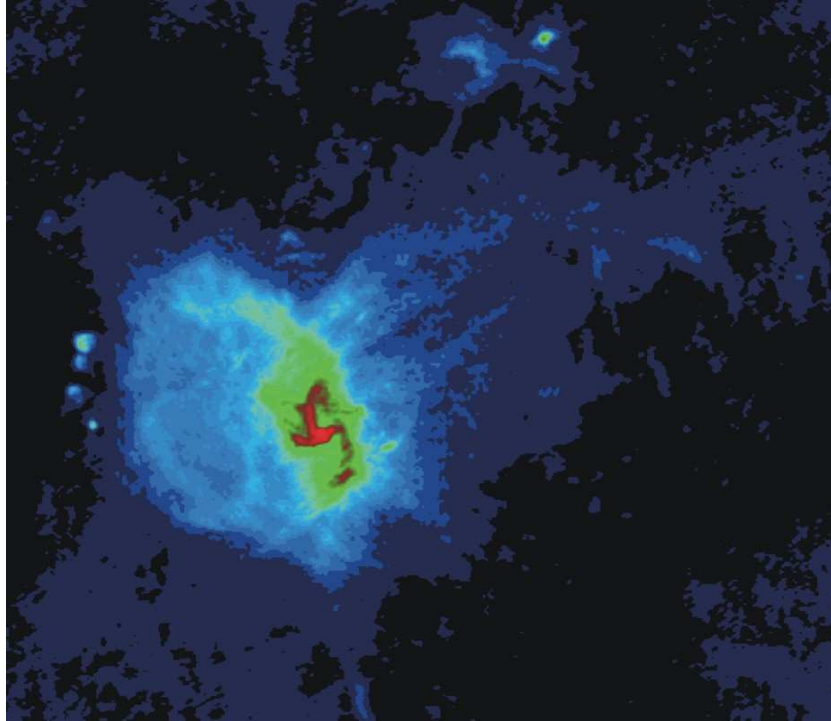


Figure 1.3: Sagittarius A complex at 6 cm: The light blue region shows Sgr A East, while the green and red mark the thermal emission of Sgr A West. Image courtesy of NRAO/AUI; F. Yusef-Zadeh and M. Morris.

thermal peaks were assumed to be emission from heated dust located within or near to HII regions.

The circum nuclear disk (CND) (Fig. 1.4) is believed to be an association of clouds/filaments of dense (10^4 - 10^7 cm^{-3}) and warm (several 100 K) molecular gas ($\sim 10^4 M_{\odot}$ of dust and gas), which orbits the nucleus in a circular rotation pattern, with a sharp inner edge at 1.5 pc and extends no further than 7 pc from the centre (Guesten et al. 1987). Observations with high density molecular tracers like HCN(3-4) and CS(7-6) show that the Northern and Southern lobes of the CND are independent structures, with different excitation levels, the Southern part being warmer than the Northern part (Fig. 1.4) (Montero-Castaño et al. 2006, 2009).

The region inside the cavity formed by the CND contains atomic and

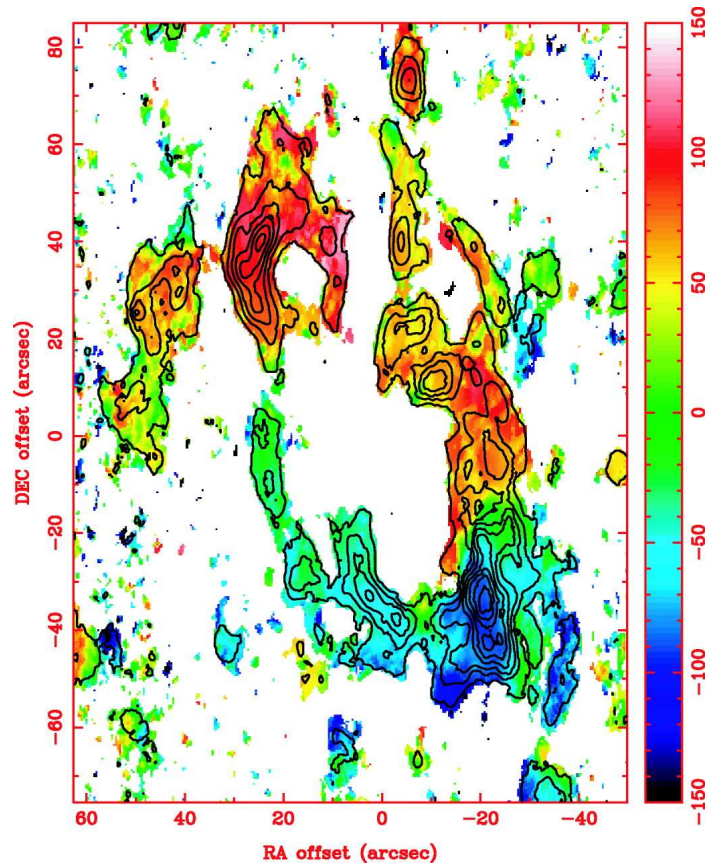


Figure 1.4: HCN emission map of the circum nuclear disk (Christopher et al. 2005).

ionized gas. High resolution interferometric observations of this central region at 6 cm identified three streams of ionized gas (Lo & Claussen 1983), which were explained as an inflow of gas, possibly from the CND, ionized by a central source, and is known as the mini-spiral (Fig. 1.5). 8.3 GHz VLA observations of the H₉₂ α line of the HII region identified three main kinematic structures, the Northern Arm, Western Arc and the extended Bar (refer Fig. 1.5), and determined a uniform electron temperature of ~ 7000 K in the HII region (Roberts et al. 1991). A fourth feature, the Eastern Arm, can also be recognised in the images of thermal emission from dust particles in the ionized cavity and the neutral gas ring (Telesco et al. 1996). These thermal structures were interpreted to be ionization fronts at the interfaces

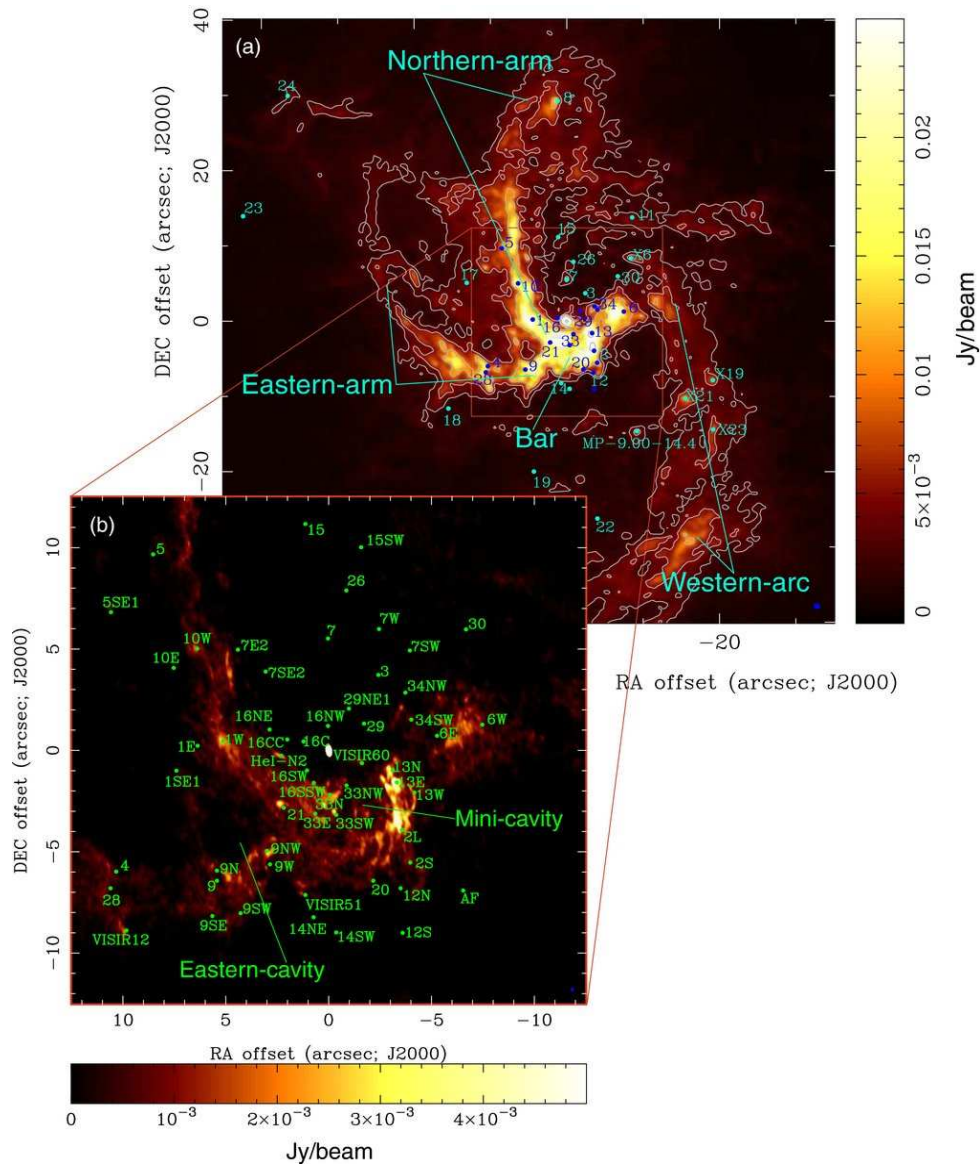


Figure 1.5: Background: VLA continuum image of Sgr A West at 3.6 cm. Inset: VLA continuum image at 1.3 cm. The mini-spiral arms and the IRS position are marked out (Zhao et al. 2009).

between the low-density and high-density regions defined by the neutral ring. Roberts et al. (1996) showed that the Northern Arm and the Western

Arc are unrelated kinematically, and that the Western Arc has the same orientation as the CND.

Far-infrared continuum measurements revealed the dust in the mini-spiral, plus an elliptical structure centred on Sgr A* and intersecting the mini-spiral at the Western Arc, which was identified as the photodissociated inner rim of the CND (Latvakoski et al. 1999). A comparison to radio maps show that the radio features are 1-3'' closer to Sgr A* than far-IR features, which is most pronounced at the Western Arc.

1.1.2 Nuclear Star Cluster

The central region of the Milky Way contains a dense star cluster with the SMBH at its dynamical center (Fig. 1.6). The distribution of stars around the black hole can be described by a broken-power law with a power-law slope of $\tau=0.19\pm0.05$ inside a break radius (projected) of $R_{\text{break}}=6''.0\pm1''.0$ and $\tau=0.75\pm0.10$ outside (Schödel et al. 2007). With the help of adaptive optics systems, observations have found a significantly lower number of late-type stars in the central few arcseconds, while there is a larger number of early-type stars in this region (Genzel et al. 2003; Eisenhauer et al. 2005). The central arcseconds contain several populations of stars: Old metal-rich M, K, G type giants (Maness et al. 2007), AGB type intermediate-bright stars (Krabbe et al. 1995; Blum et al. 1996, 2006), several bright and young objects associated with the mini-spiral such as IRS 1W, 3, 9, 10W and 21 (Becklin et al. 1978; Genzel 1996; Krabbe et al. 1995), which are mass losing and interact with the ISM in the GC (bow-shock sources, Tanner et al. (2002)). Within the inner 0.5 pc, there is a distinct population of massive young stars (Krabbe et al. 1995; Allen et al. 1990; Paumard et al. 2001; Moutaka et al. 2005; Mužić et al. 2008). Even closer to the SMBH, there exists another population of stars called the S-stars, which exhibit extremely high velocities of a few thousand km s^{-1} (Eckart et al. 1999; Eisenhauer et al. 2005; Ghez et al. 2003). Their closed orbits around Sgr A* were used to determine the mass of the black hole accurately. These S-stars are mainly B stars. The existence of young stars very near to the SMBH is puzzling, because the strong tidal forces near the black hole should inhibit star formation in these regions.

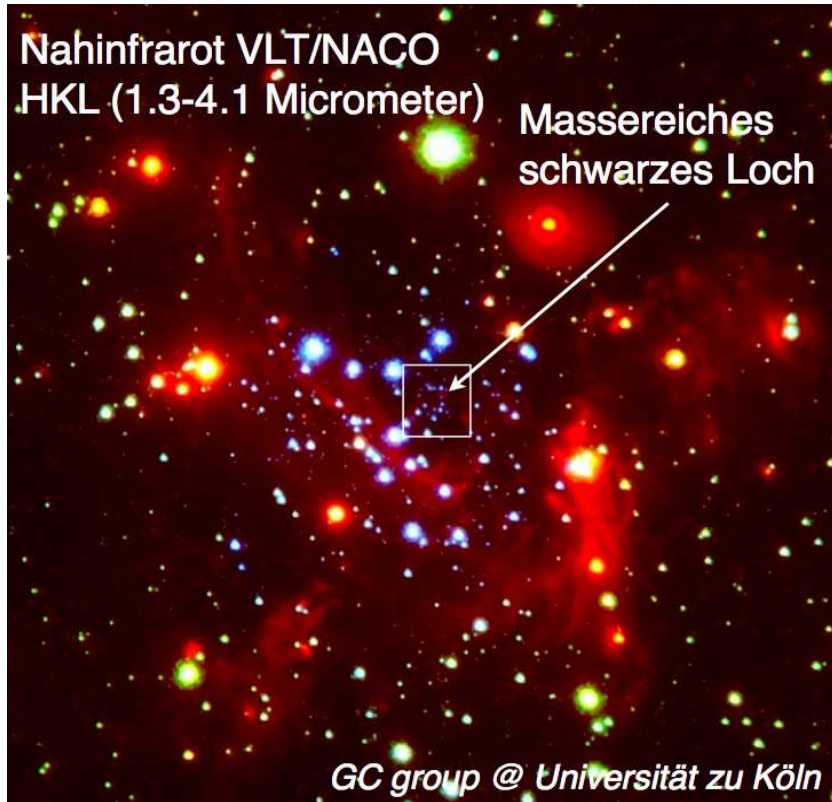


Figure 1.6: NIR HKL composite image of the central $\sim 40''$ region of the GC. Image Credit: G. Witzel.

1.1.3 Sgr A*

Sgr A* is known to radiate well below its Eddington limits at almost all wavelengths ($L_{\text{Sgr A}^*} \sim 10^{-7} L_{\text{Edd}}$). The source is visible at all times in the radio frequencies (Falcke et al. 1998; Zhao et al. 2001), while in the NIR and X-ray wavelengths, it is visible only in its flaring, or high activity states. This has been explained partly due to its low observed accretion rate. The spectral energy distribution (SED) of Sgr A* in its quiescent stage is shown in Fig. 1.7. The radio/sub-mm part of the SED is characterized by the so-called "sub-mm bump". Sabha et al. (2010) report a lower flux density limit of 2 mJy for Sgr A* in the quiescent stage, which they have modelled using synchrotron emission from a continuous or spotted accretion disk.

A large part of the quiescent state X-ray emission is reported to be from an extended thermal bremsstrahlung source coinciding with the position of Sgr A* (Baganoff et al. 2001, 2003). The SED of Sgr A* was first explained with a radiatively inefficient accretion flow such as the Advection Dominated Accretion Flow (ADAF) Narayan et al. (1995). The ADAF model (Narayan et al. 1998; Narayan & McClintock 2008; Yuan et al. 2003) involves an optically thin, geometrically thick accretion disk. Since the radial velocity and temperature of the accretion flow is much larger than in a standard thin disk, the density of accretion flow is lower, making the radiative time scales to be longer than the accretion time scale. Thus the energy of the accretion flow is not radiated away and is stored as thermal energy instead, leading to the observed low radiative efficiency.

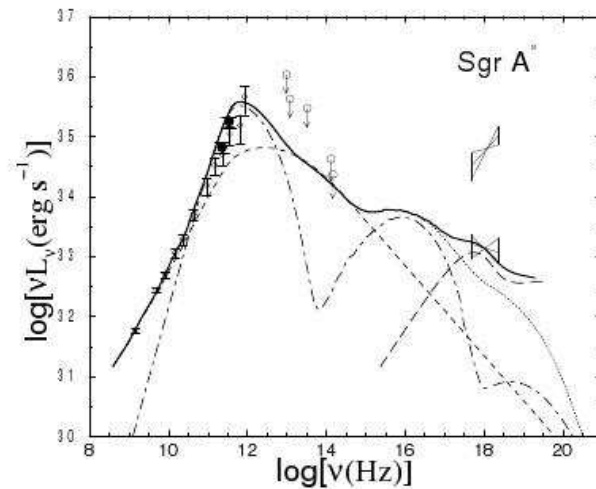


Figure 1.7: Spectral energy distribution of the quiescent emission of Sgr A*. The synchrotron and synchrotron self-Compton (SSC) emission of thermal electrons is represented by the dot-dashed line, and the non-thermal electrons by the dashed line, while the dotted line shows the total synchrotron and SSC emission. The solid line also includes Bremsstrahlung emission (Yuan et al. 2003).

1.1.4 Flaring activity of Sgr A*

Sgr A* is known to be highly variable across all wavelength regions, from the NIR/X-ray (Baganoff et al. (2001); Porquet et al. (2003); Eckart et al. (2006b)) to the radio/sub-mm wavelengths (Lo & Claussen 1983; Zhao et al. 1992; Tsuboi et al. 1999; Wright & Backer 1993; Tsutsumi et al. 1998). The variation ranges from time scales of the order of a few minutes to a few hours to a few days (Bower et al. 2002; Herrnstein et al. 2004; Zhao et al. 2003, 2004; Mauerhan et al. 2005; Eckart et al. 2006b,a; Meyer et al. 2006) and is polarized in the radio, sub-mm and IR bands (Yusef-Zadeh et al. 2008; Marrone et al. 2008; Eckart et al. 2006b, 2008a; Zamaninasab et al. 2010; Trippe et al. 2007). This variability can be used to determine fundamental parameters of the central SMBH, and give an insight into the basic emission mechanisms of the accretion disk.

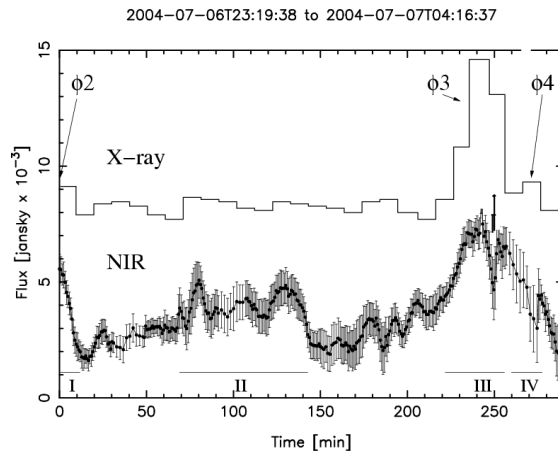


Figure 1.8: Simultaneous flaring activity in the NIR and X-ray light curves of Sgr A* (Eckart et al. 2006b).

The first simultaneous NIR/X-ray flare was observed by Eckart et al. (2004) (Fig. 1.8). Since then several such NIR/X-ray flares have been observed (Baganoff et al. 2001; Eckart et al. 2006b), along with observations of flaring activity in the radio/sub-mm regime ~ 1.5 -2 hours later (Fig. 1.9), indicating that there is a link between the flaring activity in these two

wavelength regimes (Eckart et al. 2006a, 2008b; Yusef-Zadeh et al. 2006b; Marrone et al. 2008; Yusef-Zadeh et al. 2009). Several models have been used to explain the flaring activity in Sgr A*:

- A synchrotron self-Compton model involving upscattering of sub-mm photons into NIR and X-ray wavelengths (Eckart et al. 2006b,a; Yusef-Zadeh et al. 2006a; Sabha et al. 2010; Eckart et al. 2008a).
- A model involving emission from synchrotron components with a cooling break (Dodds-Eden et al. 2009; Yuan et al. 2003).
- A jet model with a compact, weak jet structure where the jet or accretion disk instabilities cause the flaring activity (Markoff et al. 2007, 2005).
- Emission arising from statistical fluctuations in the accretion disk around the SMBH (Do et al. 2009; Meyer et al. 2008).

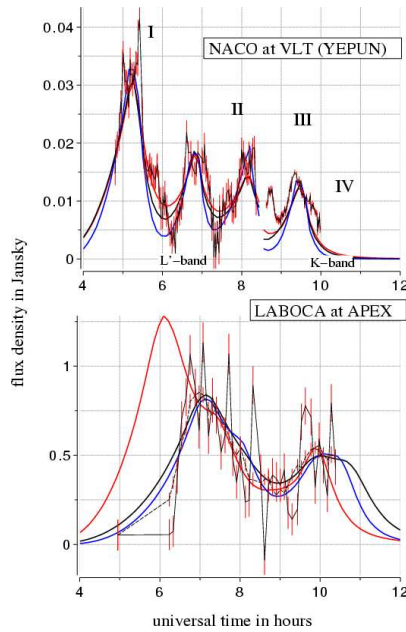


Figure 1.9: Light curves of Sgr A* showing flaring activity at the NIR and sub-mm wavelengths, with a 1.5 ± 0.5 hr delay between the NIR and sub-mm light curve (Eckart et al. 2008b).

1.2 This thesis

In this thesis, I will present results from radio interferometry observations with local mm-telescope arrays such as CARMA and ATCA, and infrared data obtained from the VLT telescopes. The basics of radio astronomy and interferometry are introduced in Chapter 2. This thesis mainly consists of two parts:

- The Galactic Centre mini-spiral region: Here I will present results from mm-wavelength observations of the GC mini-spiral and comparisons with infrared maps of the same region, along with an analysis of the interstellar medium of the region. This is described in Chapter 3 of the thesis, which contains a description of the observations, data reduction and the high resolution maps of the region, along with a spectral index analysis and analysis of derived physical properties from selected regions in the mini-spiral.
- Flaring activity of Sgr A*: Motivated by the need to constrain the properties of Sgr A* and model its flaring activity, we performed multiwavelength observations of the source in 2007 and 2008. I present results from these coordinated multi-wavelength observations of Sgr A*, in particular the radio interferometry data obtained, and the results of the modelling of the observed flares in Sgr A*. Chapter 4 describes the theoretical model in detail, and Chapter 5 presents the observations, data reduction methods, in particular the extraction of a long light curve in the mm-domain from radio interferometry data, and the modelling results and analysis of individual flares.

Chapter 6 contains a brief summary of results, conclusions and outlook.

Chapter 2

Background

2.1 Radio Astronomy

With Maxwell's equations of electromagnetic radiation, it was shown that astronomical sources could emit at different wavelengths, not just in the optical waveband. The discovery of an actual radio source in the sky was made only in the early 1930's with Karl Jansky's detection of an extraterrestrial source of radio emission, which was later identified to be the Milky Way (Jansky 1933). Further advances were made when Grote Reber in 1937 built a 9 m parabolic radio telescope and conducted the first sky survey in radio frequencies.

The Earth's atmosphere and ionosphere are transparent to two main bands, the optical/NIR and the radio frequencies, as shown in Fig. 2.1, which enables astronomers to observe astronomical sources from ground-based observatories using radio and optical telescopes. Radio telescopes generally operate between the wavelengths of about 10 metres (30 MHz) and 1 millimetre (300 GHz), where they detect radio emission from various astronomical sources like stars, galaxies, active galactic nuclei, etc. The ionosphere causes scintillation in radio waves at wavelengths longer than 20 cm and becomes completely opaque to wavelengths longer than 10 m, while atmospheric absorption creates difficulties in observing radio emission

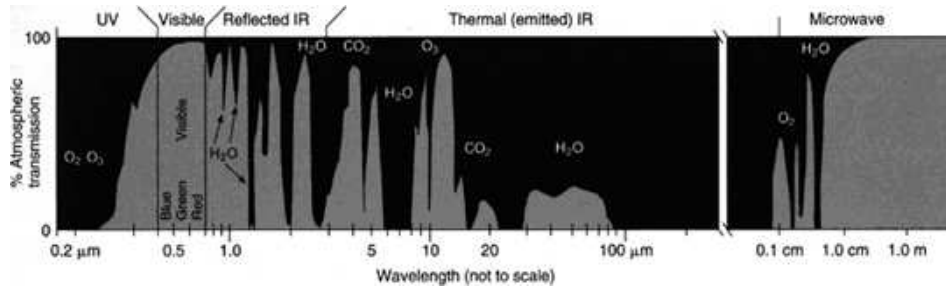


Figure 2.1: Transmission windows of Earth's atmosphere. Image from NASA Earth Observatory website.

at wavelengths shorter than 1 cm, where only very specific wavebands are absorption-free.

2.2 Emission processes

There are two main types of electromagnetic emission: Continuum emission and Line emission.

2.2.1 Continuum emission

Continuum emission is produced from the acceleration of charged particles where the photons produce a continuous spectrum, as opposed to quantised emission that gives rise to spectral lines. Continuum radio emission processes can be divided into two main types: Thermal and Non-thermal processes.

Thermal emission

These are processes which depend on the temperature of the emitter or particle distribution.

- Black body radiation

The simplest example of thermal emission is black body radiation. A black body absorbs all radiation that falls on it and emits a smooth spectrum of radiation that peaks at a frequency dependent on its temperature. The power emitted is then given by Planck's law

$$B(\nu, T) = \frac{2h\nu^3}{c^2} \frac{1}{(e^{h\nu/kT} - 1)} \quad (2.1)$$

where ν is the frequency, k is the Boltzmann's constant, T is the temperature and c is the velocity of light. For radio wavelengths, we can use the Rayleigh-Jeans approximation for energies $h\nu \ll kT$, which gives

$$B(\nu, T) = \frac{2h\nu^2 kT}{c^2} \quad (2.2)$$

Some examples of thermal black body radiation are the moon, asteroids, dust emission from the interstellar medium, etc.

- Free-free emission

Charged particles which move in a field of ionized atoms slow down by emitting photons. The particle is unbound or free before and after this interaction, and hence the process is called free-free emission or Bremsstrahlung. Larmor's formula gives the power of electromagnetic radiation produced by an accelerating electrical charge q as

$$P = \frac{2q^2\dot{v}^2}{3c^3} \quad (2.3)$$

where the acceleration \dot{v} is produced by electrostatic forces. For a distribution of charged particles, such as ionized plasma, which is in thermodynamical equilibrium, this radiation is then thermal in nature. For free-free emission from ionized hydrogen clouds (or HII regions) we can assume that only the electron-ion collisions and radiation from electrons are important. Then, assuming a Maxwell-Boltzmann velocity distribution, we can derive the opacity of the region to be

$$\tau_\nu \propto \int \frac{N_e^2}{\nu^{2.1} T^{3/2}} ds \quad (2.4)$$

where N_e gives the number density of electrons. This implies that for low frequencies where $\tau_\nu \gg 1$, the HII region is optically thick or

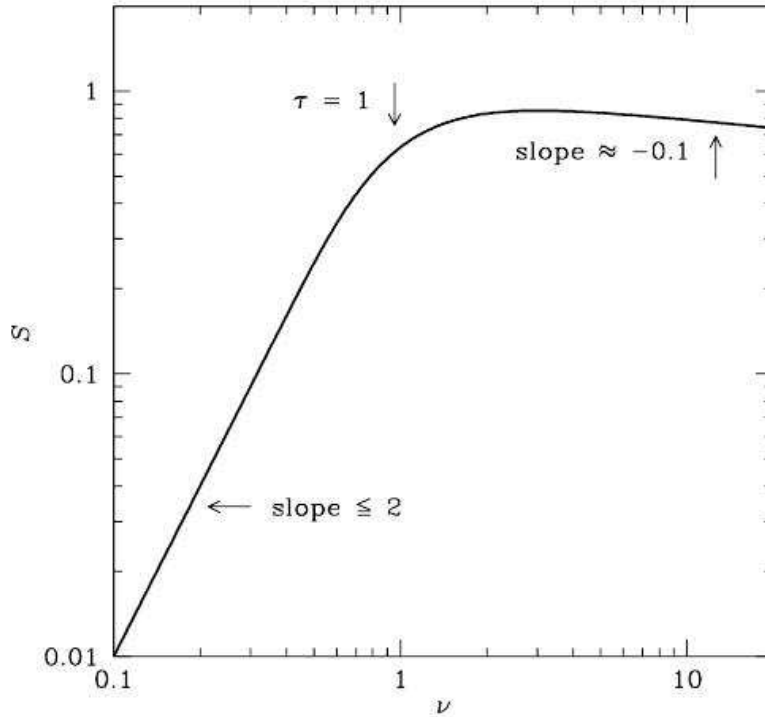


Figure 2.2: Free-free emission spectrum of a thermal distribution of particles. Image from NRAO radio astronomy lecture.

self-absorbed, its spectrum approaches that of a black body with temperature T , and flux density varies as $S_\nu \propto \nu^2$, while at higher frequencies, $\tau_\nu \ll 1$, the HII region is optically thin and $S_\nu \propto \nu^{-0.1}$, as shown in Fig. 2.2.

Non-thermal emission

The dominant source of non-thermal emission in astronomy is synchrotron emission.

- Synchrotron emission arises from the acceleration of relativistic charged particles in a magnetic field. For a power law distribution

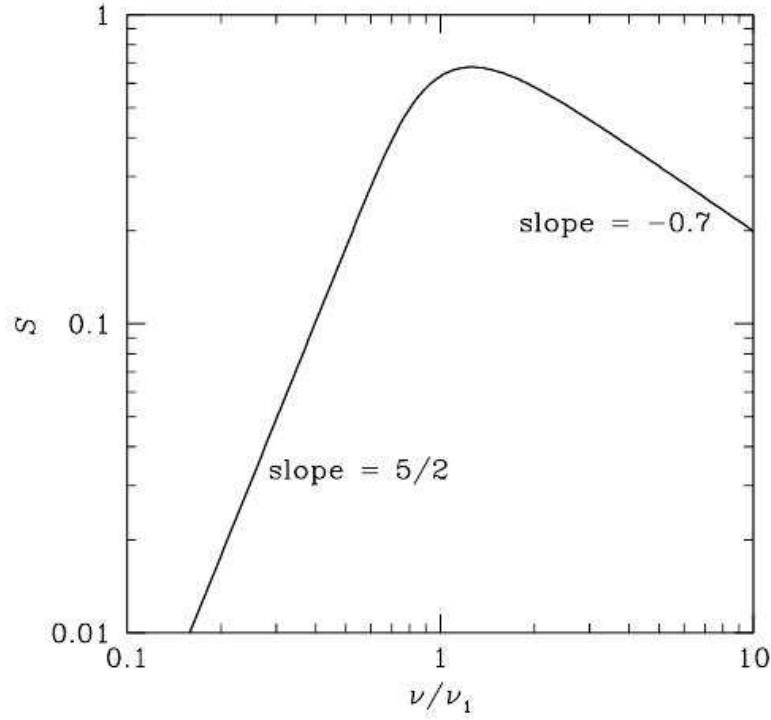


Figure 2.3: Synchrotron spectrum. Image from NRAO radio astronomy lecture.

of electrons given by

$$N(E)dE \propto E^{-\delta}dE, \quad (2.5)$$

the emissivity is then

$$\epsilon_\nu \propto B^{(\delta+1)/2}\nu^{(1-\delta)/2} \quad (2.6)$$

$$\propto B^{(\alpha+1)}\nu^{(-\alpha)} \quad (2.7)$$

where $\alpha = (\delta - 1)/2$. At a sufficiently low frequency, for a purely homogenous synchrotron source, the source becomes optically thick and the flux density becomes $S_\nu \sim \nu^{5/2}$, while at higher frequencies the source is optically thin, as shown in Fig. 2.3.

2.2.2 Line emission

Spectral line emission occurs at discrete frequencies, due to changes in the internal energy of atoms/molecules that have quantised energy levels. At radio wavelengths, they are caused by rotational transitions of molecules. The main spectral lines observed in the radio bands are the neutral hydrogen line at 21 cm, and water maser lines.

2.3 Radio telescopes

We use radio telescopes to measure the emission from the radio sources mentioned in the previous section. A typical radio telescope consists of a radio antenna with the shape of a parabolic dish. This can be pointed in the direction of the source to collect electromagnetic radiation, which is fed into a receiver. The weak signals are amplified with an amplifier and further processed. The strength of radiation is measured in units of flux density known as Jansky, given by

$$S_\nu = \int_{\text{source}} I_\nu d\Omega \quad (2.8)$$

where I_ν is the intensity of the source in units of $\text{Wm}^{-2}\text{Hz}^{-1}\text{sr}^{-1}$, and $d\Omega$ is the solid angle subtended by the source at the observer's location. Flux density is measured in units of Jansky (Jy), with $1 \text{ Jy} = 10^{-26} \text{ Wm}^{-2}\text{Hz}^{-1}$. For an extended source, the surface brightness is measured in flux density per unit surface area, which is Jy/beam for a radio map, where the beam is the area of the point source response in the map. The brightness temperature of the source is defined to be the temperature at which a pure black body source would give rise to the same radio emission per unit area as the source,

$$T_b = S_\nu \lambda^2 / 2k d\Omega \quad (2.9)$$

where k is the Boltzmann constant and λ is the wavelength of the source.

The sensitivity of the radio telescope is a function of the collecting area and the angular resolution is defined to be

$$\theta = 1.22 \lambda / D \quad (2.10)$$

where λ is the wavelength of incoming radiation and D is the aperture of the telescope. Since the aperture of a single telescope can be a limiting factor in achieving higher resolution images, interferometry techniques were introduced. Radio interferometry involves the use of a number of smaller antennas to synthesize a larger aperture. Then, in (2.9), D is replaced by B , which would be the distance between two telescopes. At a wavelength of 3 mm for a 10 m telescope, the angular resolution would be $63''$, while for two telescopes separated by a distance of 100 m, i.e. $B=100$ m, the angular resolution becomes $6.3''$.

2.4 Interferometry

The basic idea of interferometry can be understood from the Young's double slit experiment. In this experiment, waves passing through two slits generate wavelets that produce interference fringes, with constructive interference occurring when the path difference is an integral number of wavelengths.

The van Cittert-Zernike relation describes the spatial coherence function V_ν of a source subtending a solid angle of $d\Omega$ in the sky as a cross-correlation of the radiation field received at two points r_1 and r_2 . This is written as

$$V_\nu(\mathbf{r}_1, \mathbf{r}_2) \approx \int I_\nu(\mathbf{s}) e^{(-2\pi i \nu \mathbf{s} \cdot (\mathbf{r}_1 - \mathbf{r}_2)/c)} d\Omega \quad (2.11)$$

where $I(\mathbf{s})$ is the intensity of incoming radiation at frequency ν . By measuring and inverting this mutual coherence function (which has the dimension of power) using a Fourier transform, we can obtain the intensity distribution of the source and image it (Wilson et al. 2009).

Consider the case of a simple two element interferometer as shown in Fig. 2.4. Radio waves from the source reach each element of the interferometer at different times, causing changes in the path difference between the two elements. When we combine the signals from the two elements we obtain an interference fringe pattern, which gives the distribution of the source in the sky.

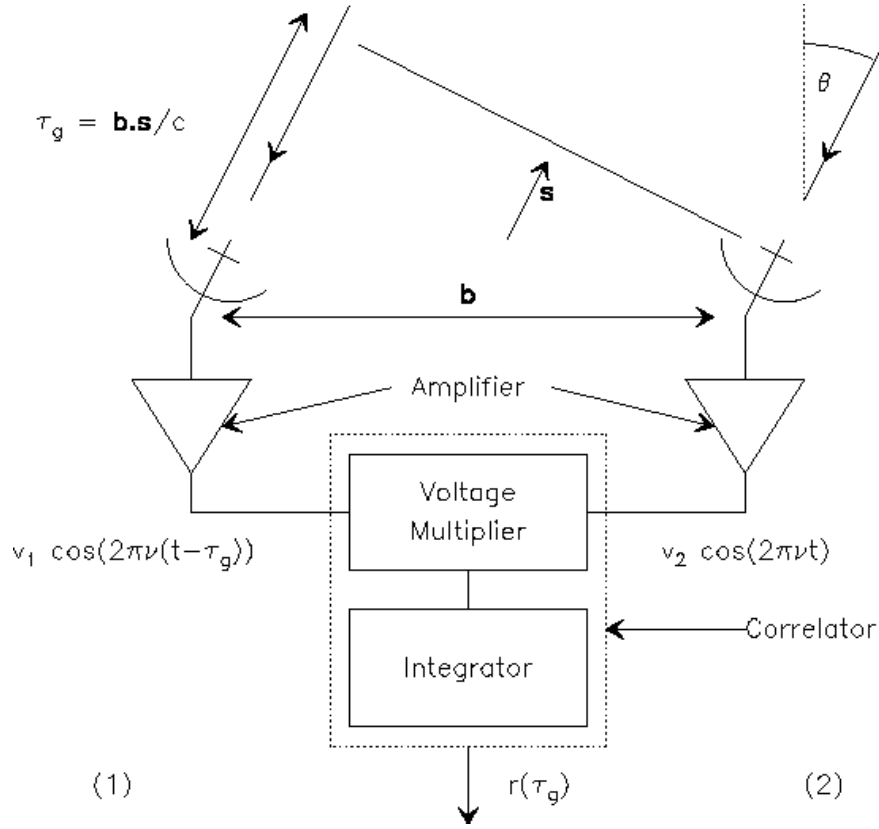


Figure 2.4: A simple two-element interferometer. Image credit: *Proceedings from IRAM Millimeter Summer School 2* edited by A. Dutrey.

Here \mathbf{b} is the baseline separation, θ gives the angle between the baseline and the wavefront propagating from the source in the sky, and

$$\tau_G = \mathbf{b} \cdot \mathbf{s} / c \quad (2.12)$$

gives the wave propagation delay (geometric). For a point source emitting monochromatic radiation, the voltage measured by the two elements are given by

$$R_1(t) = v_1 \cos[2\pi\nu(t - \tau_G)], \quad (2.13)$$

and

$$R_2(t) = v_2 \cos(2\pi\nu t) \quad (2.14)$$

The signals are multiplied by the voltage multiplier to give

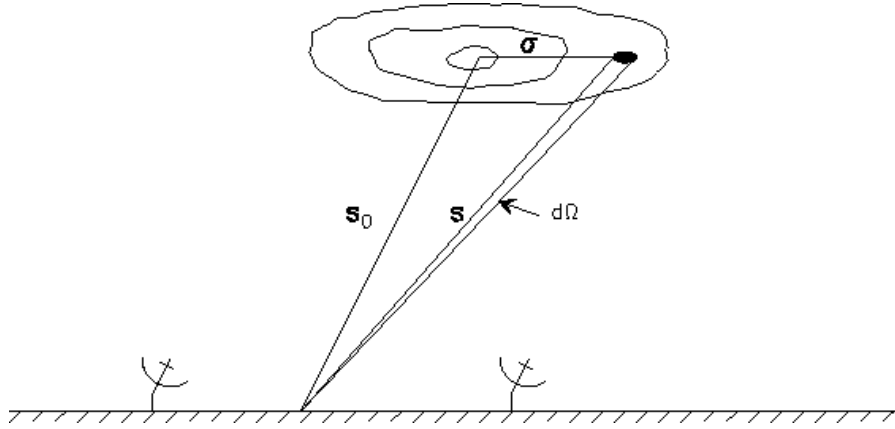


Figure 2.5: Sketch of an extended image in the sky, with position vectors used to determine the interferometer response. Image credit: Proceedings from IRAM Millimeter Summer School 2 edited by A. Dutrey.

$$r(t) = R_1(t) \times R_2(t) \quad (2.15)$$

$$= [v_1 \cos(2\pi\nu(t - \tau_G))] \times [v_2 \cos(2\pi\nu t)] \quad (2.16)$$

$$= v_1 v_2 \cos(2\pi\nu\tau_G) \quad (2.17)$$

τ_G varies slowly with the Earth's rotation, and $r(t)$ oscillates as a cosine function, called the fringe pattern. For an extended source which subtends a solid angle Ω in the sky (as shown in Fig. 2.5), the total response measured by the correlator is given by

$$R(\mathbf{b}) = \int \int_{\Omega} A(\mathbf{s}) I_{\nu}(\mathbf{s}) e^{i2\pi\nu\tau_G} d\Omega d\nu \quad (2.18)$$

where $A(\mathbf{s})$ is the effective collecting area in the direction \mathbf{s} (assumed to be the same for both antennas) and $I_{\nu}(\mathbf{s})$ is the brightness distribution of the source. Since $\mathbf{s} = \mathbf{s}_0 + \boldsymbol{\sigma}$, where \mathbf{s}_0 is defined as the centre of the source, from the above equation we obtain

$$V(\mathbf{b}) = \int \int_{\mathbf{S}} A(\boldsymbol{\sigma}) I(\boldsymbol{\sigma}) e^{i\omega\mathbf{B}\cdot\boldsymbol{\sigma}/c} d\boldsymbol{\sigma} \quad (2.19)$$

where V is defined as the visibility function of the source.

We choose a coordinate system (u, v, w) measured in units of wavelength $\lambda = 2\pi c/\omega$ such that $\frac{\omega}{2\pi c}\mathbf{B} = (u, v, w)$, and $\boldsymbol{\sigma} = (x, y, z)$, where x and y are

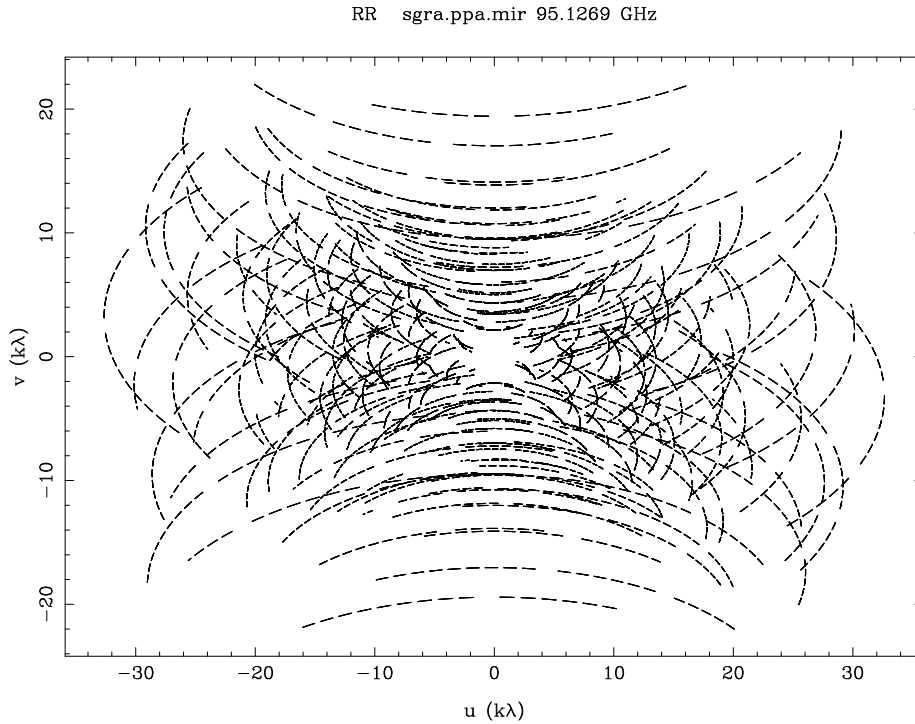


Figure 2.6: An example of the uv coverage of a telescope array.

direction cosines with respect to u and v . Thus

$$V(u, v, w)e^{-i2\pi w} = \int_{-\infty}^{\infty} \int_{-\infty}^{\infty} A(x, y)I(x, y)e^{-i2\pi(ux+vy)} dx dy. \quad (2.20)$$

An inverse Fourier transform of the above equation gives us

$$I'(x, y) = A(x, y)I(x, y) = \int_{-\infty}^{\infty} \int_{-\infty}^{\infty} V(u, v, 0)e^{-i2\pi(ux+vy)} du dv. \quad (2.21)$$

Here each observation of the source with a particular baseline and orientation provides one point in the uv plane. For an array of telescopes, the different baselines along with the rotation of the Earth fill up the uv plane, as shown in Fig. 2.6.

To avoid transmission losses at high frequencies, we use receiver systems which employ the heterodyne principle to down convert the observing radio frequency (RF) to an intermediate frequency (IF), by mixing the signal with a signal from a Local Oscillator (LO).

Basic data reduction steps for interferometry observations

In order to correct for errors introduced in our measurements due to instrumental and atmospheric effects, we have to perform certain calibration steps. We also perform a flagging where we flag bad data points or outliers in the visibilities. The three main calibrations performed are:

- **Bandpass calibration:** The instrument bandpass is corrected by measuring channel gains and offsets of an intense source, usually at the beginning of observations.
- **Phase calibration:** Determines the instrumental and atmospheric phase effects by observing a point-like source that is not variable and whose position is well-known.
- **Amplitude calibration:** Calibrates the amplitude scale by observing a source of known flux density, usually a planet like Uranus or Mars.

For mm-wavelength observations, calibrator observations are done every few minutes, to account for atmospheric effects.

Mapping

The final image is produced from the visibilities obtained after the calibration is performed. The main steps are:

- **Inverting the visibilities:** The image produced after performing an inverse Fourier transformation of the visibilities is called the *dirty image*. The incomplete sampling of the uv plane of the telescope array causes imperfections in this image. The response of the interferometer to a point-like source is given by the *dirty beam*, or the point spread function (PSF).
- **Deconvolution:** This step corrects for the sampling effects. The CLEAN algorithm (Högbom 1974; Schwarz 1978) convolves the dirty map with a *clean beam*, which is an ideal Gaussian-shaped beam, to produce a clean map.

2.5 Telescopes and Instruments used

In this section, I describe briefly the telescopes and instruments which were used to acquire the data presented in this thesis. All the radio data presented here were observed in the mm-wavelengths, with the local mm-telescope arrays CARMA and ATCA, and the IRAM 30m telescope. In addition to the radio data, the infrared data presented in this thesis were acquired at VLT.

2.5.1 CARMA

The Combined Array for Research in mm-wave Astronomy (CARMA)¹(Bock et al. 2006) is located at Cedar Flat, Eastern Cali-

¹Support for CARMA construction was derived from the states of California, Illinois, and Maryland, the Gordon and Betty Moore Foundation, the Kenneth T. and Eileen L. Norris Foundation, the Associates of the California Institute of Technology, and the National Science Foundation. Ongoing CARMA development and operations are supported by the National Science Foundation under a cooperative agreement, and by the CARMA partner universities.



Figure 2.7: CARMA telescope array. Image from CARMA website <http://mmarray.org>.

fornia. It consists of an array of 23 telescopes, nine of which are 6.1 m in diameter, six are 10.4 m in diameter and eight are 3.5 m in diameter with receivers that can observe in three wavelength bands: 7, 3 and 1.3 mm. The antennas are located at various stations in an area over 2 km in diameter, with the baselines ranging from 7 m to 2 km. There are 5 standard configurations A, B, C, D and E with resolutions ranging from $0.3''$ to $10''$ at 100 GHz.

2.5.2 ATCA

The Australia Telescope Compact Array (ATCA)² is located at the Paul Wild Observatory, about 25 km west of Narrabri, in Australia. It is an array of six 22-m telescopes, operated by the Australia Telescope National Facility (ATNF). It has seven main observing bands: 20 cm, 13 cm, 6 cm, 3 cm, 1 cm, 7 mm and 3 mm with angular resolutions ranging from $6''$ to $0.2''$.

²ATCA is operated by the Australia Telescope National Facility, a division of CSIRO, which also includes the ATNF Headquarters at Marsfield in Sydney, the Parkes Observatory and the Mopra Observatory near Coonabarabran.



Figure 2.8: ATCA telescope array. Image from ATCA website <http://www.narrabri.atnf.csiro.au>.

2.5.3 IRAM 30 m telescope

The Max-Planck Millimeter Bolometer (MAMBO 2) array is installed at the IRAM 30m³ telescope on Pico Veleta, Spain and performs observations at 250 GHz. The 37 channel bolometer contains 117 pixels, and a He-3 fridge is used to operate it at 300 mK.

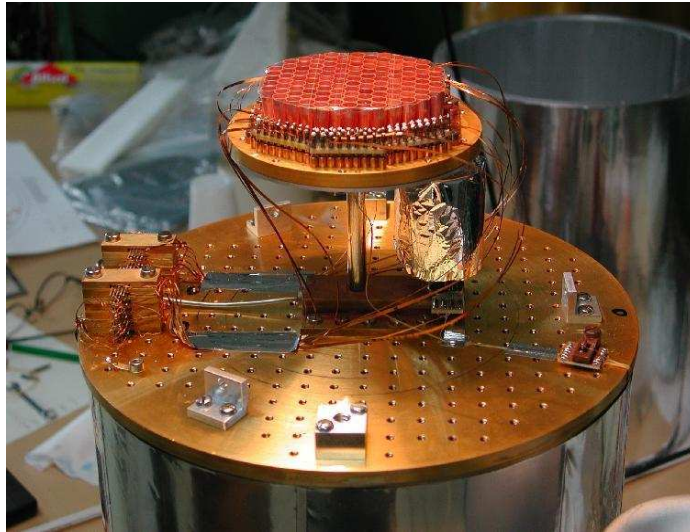


Figure 2.9: MAMBO bolometer at IRAM 30 m telescope. Image credit:IRAM website.

2.5.4 VLT

Infrared observations were carried out with the European Southern Observatory's (ESO) Very Large Telescope array (VLT) at Paranal, Chile. It consists of four main unit telescopes (UT) of 8.2 m diameter, and four movable auxiliary telescopes (AT) of 1.8 m diameter. The telescopes have a wavelength range of 300 nm to 20 μ , and contain several different instruments.

³The IRAM 30 m millimeter telescope is operated by the Institute for Radioastronomy at millimeter wavelengths - Granada, Spain, and Grenoble, France.



The VLT Array on the Paranal Mountain

ESO PR Photo 14a/00 (24 May 2000)

© European Southern Observatory



Figure 2.10: The VLT array at Paranal, Chile. Image credit: ESO.

NIR observations were carried out with the NACO (Rousset et al. 2003; Lenzen et al. 2003) instrument installed at the Nasmyth B focus of UT4 and the VLT Imager and Spectrometer for the mid-Infrared (VISIR) was used to perform MIR observations in the 8-13 μm range.

Chapter 3

The Central Parsec of the galaxy

In this chapter, I present high resolution maps from observations of the GC region performed in 2009 using CARMA. It includes the best spectral index map obtained at high resolution at millimetre wavelengths, a comparison to the MIR dust continuum and NIR Br γ emission in the same region, and an analysis of the emission processes in the mini-spiral region.

3.1 Observations and Data Reduction

3.1.1 mm observations

The radio continuum observations of the Galactic Centre were performed with the CARMA telescope, and centred on Sgr A* at $\alpha(\text{J2000.0})=17:45:40.04$ and $\delta(\text{J2000.0})=-29:00:28.09$. The 3 mm (100 GHz) data presented here were obtained with the C array configuration on the 17th of May, 2009. Intermittent observations of sources were performed for calibration purposes. The sources used were 3C279 for bandpass calibration, 1733-130 for phase calibration and Neptune for the flux calibration. The

combined grade for the quality of observations was an A+, with a good uv coverage and all 15 antennas were used to acquire data. The total opacity due to phase noise and atmospheric absorption was 0.11 at 112 GHz. Minimal flagging was applied on the data to remove shadowing effects, which arise from the shorter baselines.

The 1.3 mm (230 GHz) observations were taken using the C and D array configurations in March and April of 2009, with MWC349 for bandpass and 1733-130 for phase and amplitude calibration. The total opacity at 230 GHz was 0.61, and the combined grade for the observations was B. Due to anomalous system temperature values, antenna 7 visibility were flagged, and data from antenna 14 were flagged from 11:50.9 UT to 12:10.0 UT and 10:00.0 UT to 11:10.0 UT.

Miriad, an interferometric data reduction package, was used to perform the routine data reduction steps (refer Chapter 2), including flagging, calibration and the fourier transform of the visibilities. A CLEAN algorithm was then applied to produce the radio maps. Fig. 3.1 shows the final 3 mm image obtained after all the calibration and imaging procedures. Table 3.2 gives the beam sizes, position angles and total fluxes obtained for Sgr A* from the 3 and 1.3 mm maps using the *imfit* routine in *Miriad*.

Telescope Observing ID	Instrument/ Array	λ	UT and JD Start Time	UT and JD Stop Time
CARMA	C array	3.0 mm	2009 17 May 07:21:23.5 JD 2454968.806522	17 May 12:24:27.5 JD 2454969.016985
CARMA	D array	1.3 mm	2009 28 Mar 11:20:03.5 JD 2454918.972263	28 Mar 14:39:18.5 JD 2454919.110631
CARMA	C array	1.3 mm	2009 19 Apr 10:07:21.5 JD 2454940.921777	19 Apr 13:13:13.5 JD 2454941.050851
VLT	NACO	2.16 μm	2009 05 Aug 22:59:14.59 JD 2455049.457808	05 Aug 23:30:44.34 JD 2455049.479680
VLT	VISIR	8.6 μm	2006 05 Jun 04:55:00.0 JD 2453891.704861	05 Jun 08:01:00.0 JD 2453891.834028

Table 3.1: Log of the mm, NIR and MIR observations.

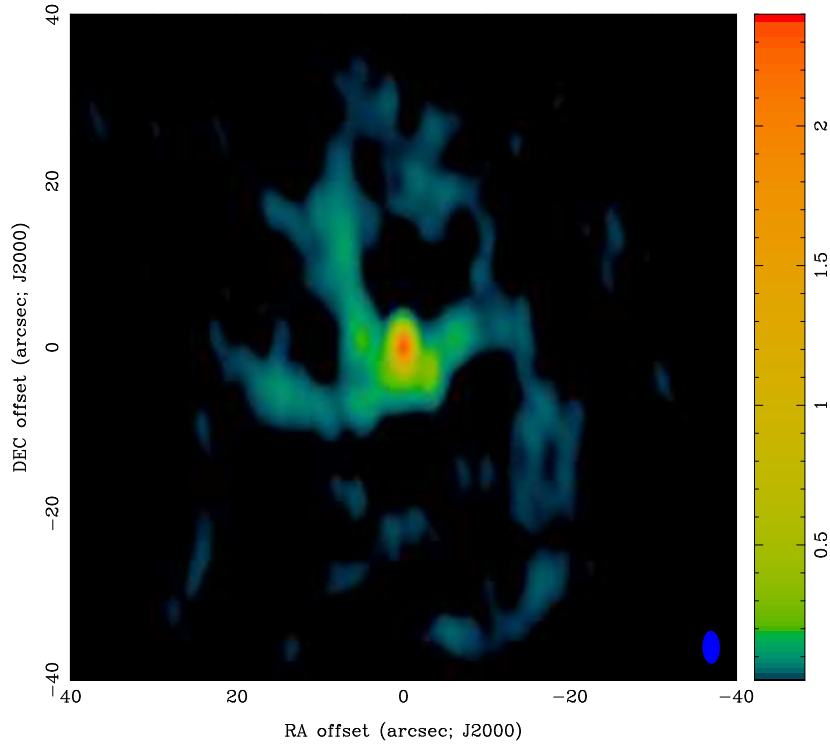


Figure 3.1: 3 mm C array map of the GC region, with a beam size of $3.96'' \times 2.09''$ ($P.A.=1.4^\circ$), indicated in the lower right part of the map. Units of flux are in Jy/beam.

λ	B_{major}	B_{minor}	PA(degrees)	Flux (Jy)
3.0 mm	3.96	2.09	1.4	2.463
1.3 mm	2.90	1.80	-1.9	2.578

Table 3.2: Fluxes of Sgr A* at 3 mm and 1.3 mm, where B_{major} and B_{minor} refer to the beam size.

3.1.2 MIR observations

The GC region was observed with the VLT Imager and Spectrometer for mid-Infrared (VISIR) at the European Southern Observatory's (ESO) Very Large Telescope (VLT) Unit 3 at $8.6 \mu\text{m}$ using the PAH1 filter (central wavelength $8.59 \mu\text{m}$ and a half-bandwidth of $\Delta\lambda=0.42 \mu\text{m}$), and a standard

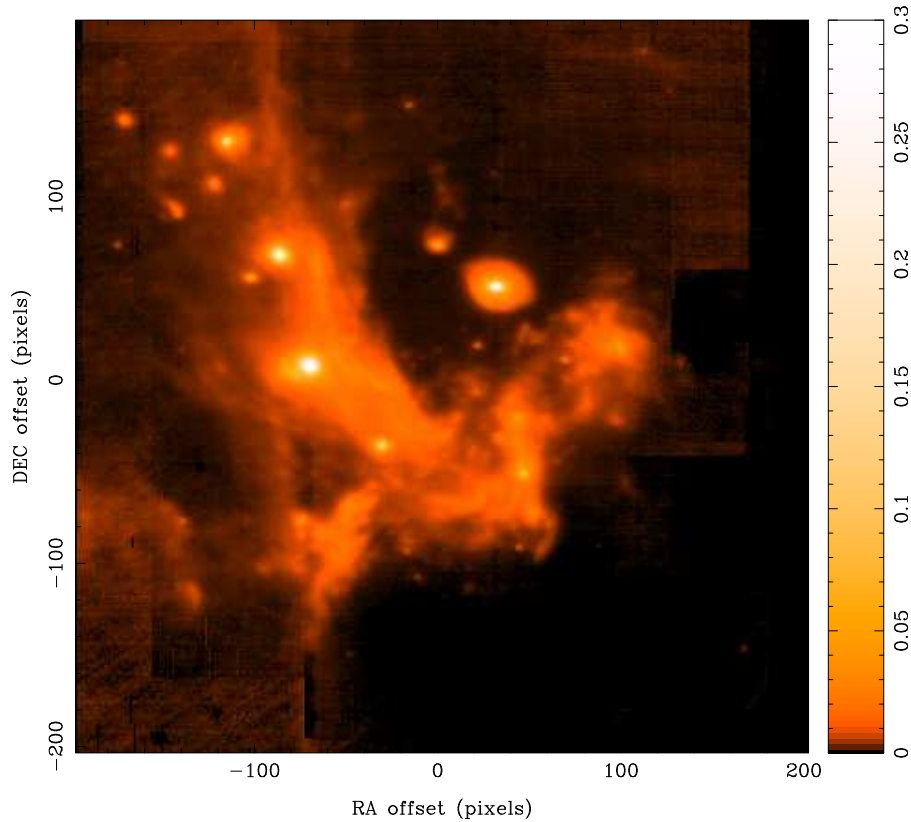


Figure 3.2: MIR map of the central $30''$ arcseconds of the galactic centre region, showing the bright IRS sources and the extended dust emission, in units of Jy/pixel.

nodding (~ 330 deg east of north) and chopping (with a chop throw of $30''$) technique. After performing a sky subtraction, the individual frames obtained by dithering were combined using a simple shift-and-add technique to produce a combined mosaic image of $30'' \times 30''$ at a pixel scale of $0.075''$ (Lagage et al. 2003). The point spread function (PSF) of $\sim 0.3''$ calculated as the full-width-at-half-maximum (FWHM) of the reference star was close to the diffraction limit of the VLT at $8.6 \mu\text{m}$, due to the good weather conditions. The standard star HD 178345 with a flux of 14.32 Jy in the PAH1 filter (Cohen et al. 1999) was used for flux calibration and as the PSF reference for image deconvolution. The MIR map of the central $30''$ is shown in Fig. 3.2. A point source subtraction was performed on this final image to remove the stellar contribution using *StarFinder* (Diolaiti et al. 2000).

Further details about the flux calibration and data reduction are given in Schödel et al. (2007).

3.1.3 NIR Brackett γ

In the near-infrared (NIR) regime, the GC was observed on August 5, 2009 with the narrow band 2.166 μm filter of the NAOS/CONICA adaptive optics system at the ESO/VLT (Lenzen et al. 2003; Rousset et al. 2003)¹. The software packages IDL and DPUSER² were used to perform standard data

¹Based on observations made by ESO telescopes at Paranal Observatory, under the programme 083.B-0390(A).

²developed by T. Ott; <http://www.mpe.mpg.de/~ott/dpuser/index.html>

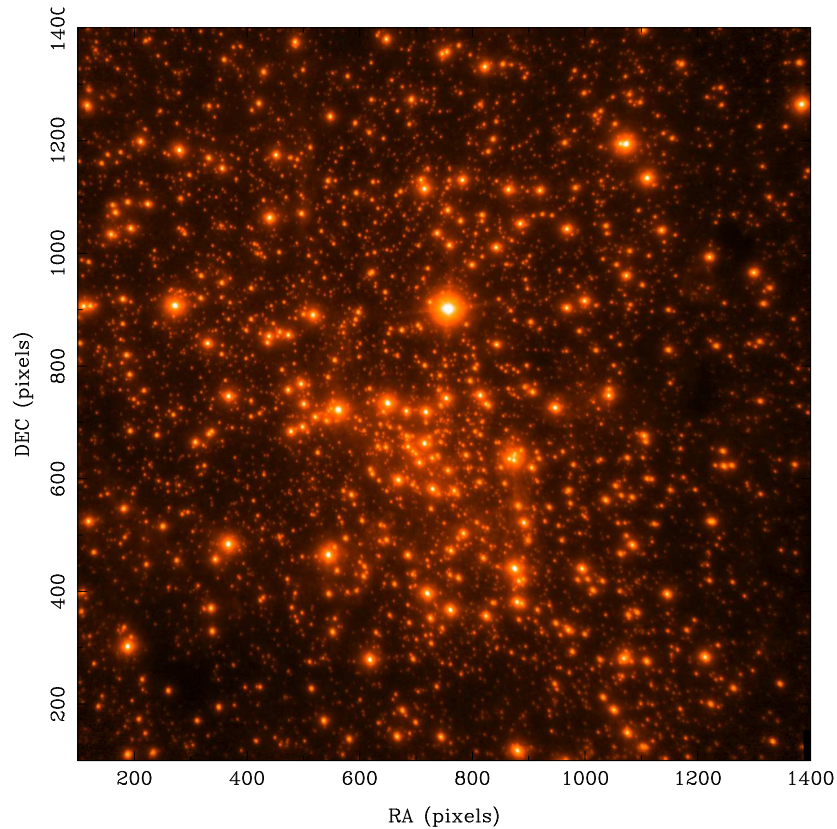


Figure 3.3: The NIR Br γ image of the central 40'' of the GC region.

reduction steps such as pixel correction, sky subtraction, flat field correction, and the detector row cross-talk correction. The reduced images were then combined using a simple shift-and-add algorithm to obtain a mosaic. The *jitter* routine (part of the ESO *eclipse* package; Devillard 1997) was used to calculate the shifts between individual exposures with a cross-correlation function and then shifted and median averaged the images. The pixel scale is $0.027''$.

StarFinder (Diolaiti et al. 2000) was used to perform the point source subtraction of the image shown in Fig. 3.3 to remove the stellar contribution from the region. The mosaic was divided into overlapping sub-images, since the field-of-view (FOV) of the $\text{Br}\gamma$ mosaic is significantly larger than the isoplanatic angles at this wavelength ($\sim 6''$), and a local PSF was extracted from each of the sub-images which was used to perform the PSF fitting and subtraction of stars (Schödel et al. 2010; Schödel 2010). The point source subtracted image is shown in Fig. 3.4. The residuals seen at the positions of bright stars are mainly due to imperfections in the PSF extraction, caused by the extreme stellar crowding in the central parsec region of the GC.

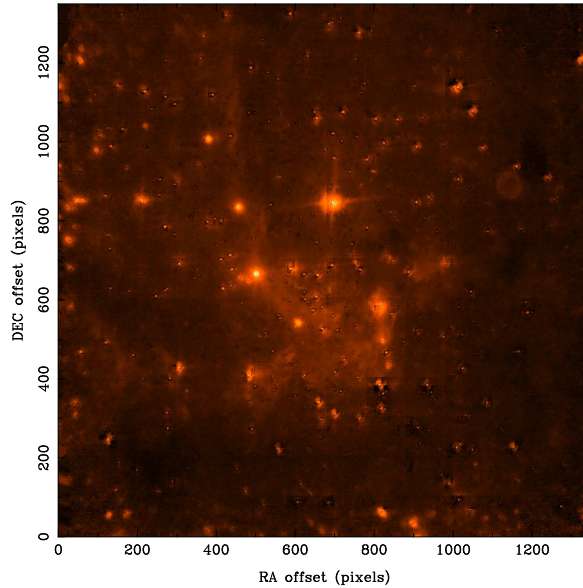


Figure 3.4: Point source subtracted NIR $\text{Br}\gamma$ image of the central $40''$ of the GC region, showing the recovered diffuse emission of the mini-spiral.

The precise K-band photometry from Schödel (2010) of 20 stars randomly distributed in the field was used to obtain the photometric zero-point, and the flux density of Vega in the K-band (Allen 1976) was used to convert the K magnitudes to flux in Jy.

3.2 Results and analysis

In order to infer different properties of the gas and dust in the mini-spiral region, fluxes must be compared at different wavelengths. For that purpose, I chose different regions in the central $20''$ of the point source subtracted $2.16 \mu\text{m}$, $8.6 \mu\text{m}$, 1.3 mm and 3 mm maps. Fig. 3.5 shows the regions marked in the 1.3 mm map. Since the beam shapes of the radio maps are elliptical, the chosen regions are elliptical in shape. This also allows to maximise aperture area on the source for a better fitting of the elongated structures in the mini-spiral, and hence prevents the loss of flux from the selected regions.

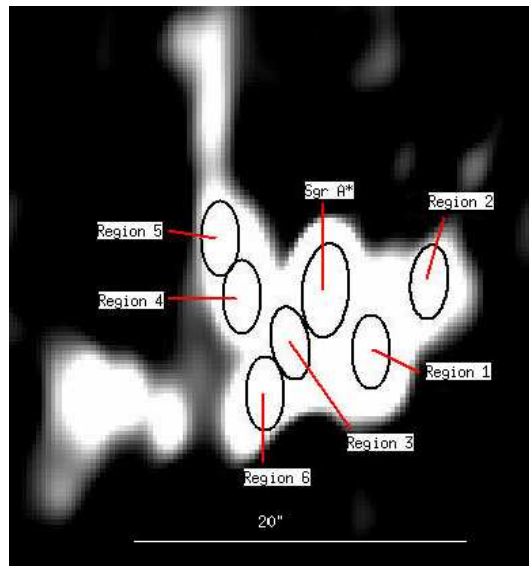


Figure 3.5: The elliptical regions used to extract fluxes from the central $20''$ region of the GC from the multi-wavelength datasets, marked on the 1.3 mm radio continuum map.

The fluxes obtained for all the regions and the corresponding values of the physical properties calculated are given in Table 3.3. The following sections describe the analysis of the dust and gas properties in the mini-spiral region.

3.2.1 Radio 3 mm and 1.3 mm maps

The main features seen in the radio continuum maps produced at 3 and 1.3 mm are: the central non-thermal source Sgr A*, the thermal emission of the mini-spiral, including the Bar, Eastern Arm and the Northern Arm (refer Fig. 1.5 in Chapter 1). The Western Arm is unresolved in the maps. At 1.3 mm a high resolution map was produced with a synthesised circular beam of size $0.90''$, shown in Fig. 3.6, which resolves several IRS sources in the mini-spiral.

The 3 mm map shown in Fig. 3.1 contains a total integrated flux of 13 Jy inside a $82.5''$ diameter area, which corresponds to the primary beam size of the CARMA array at 100 GHz. This is in good agreement with Shukla et al. (2004) who used the OVRO array at 92 GHz to obtain a $6''.95 \times 3''.47$ (P.A. = -5°) map and measured a total flux of 12 Jy from the central $85''$ region, and Wright et al. (1987) who used the Hat Creek Interferometer at 86 GHz to obtain a total flux of 12.6 Jy.

However, single dish observations at 106 GHz using the 30 m telescope at IRAM, Spain measure a total flux of 22 Jy (Mezger et al. 1989). This discrepancy in total flux measured can be explained by the fact that interferometric observations are less sensitive to the larger regions of underlying extended thermal emission of Sgr A West, and resolves it out while being more sensitive to the brighter small-scale thermal features of the mini-spiral arms and the Bar. The total amount of flux resolved out by the CARMA array is comparable to interferometric observations using other arrays. Since the amount of flux that is resolved out remains approximately the same for the two wavelengths 3 and 1.3 mm in the brighter regions of the mini-spiral, the spectral indices calculated from these two wavelengths and discussed in Sect.3.2.2 are reliable.

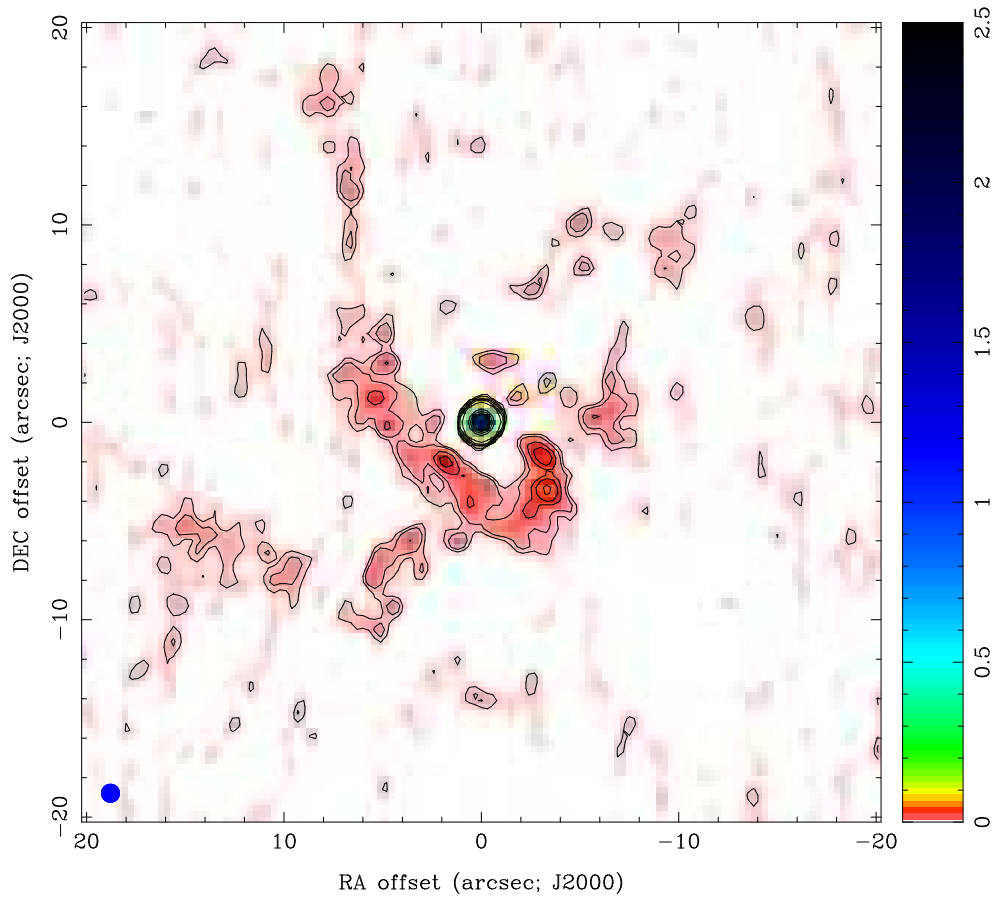


Figure 3.6: 1.3mm CD array configuration map with a synthesised circular beam size of $0.9''$. Contour levels are 0.0065, 0.01, 0.02, 0.03, 0.04, 0.05, 0.1, 0.6, 0.9, 1.2, 1.5, 2.5 Jy/beam.

The fluxes extracted from the sources marked in Fig. 3.5 in the 1.3 and 3 mm maps are tabulated in Table 3.3. The errors in the flux density measurements are derived to be

$$\sigma_{\text{flux}} = \sqrt{(\sigma_{\text{rms}}^2) + (\sigma_{\text{cal}} F_\nu)^2}, \quad (3.1)$$

where σ_{rms} gives the rms noise of the map, σ_{cal} gives the error in flux calibration and F_ν is the flux density at frequency ν . The error in flux calibration is estimated to be 15% for the CARMA array.

From Panagia & Walmsley (1978), the flux density of an optically thin thermal source emitting free-free radiation is given by

$$S_\nu = 1.001 \times 10^{-4} n_e^2 \left[\frac{V}{\text{pc}^3} \right] \left[\frac{T}{10^4 \text{ K}} \right]^{0.5} \left[\frac{D}{\text{kpc}} \right]^{-2} b(\nu, T) \text{ Jy}, \quad (3.2)$$

where

$$b(\nu, T) = 1 + 0.3195 \log(T/10^4 \text{ K}) - 0.2130 \log(\nu/1 \text{ GHz}) \quad (3.3)$$

and V is the source volume, n_e is the electron density, D is the distance to the source and T is electron temperature.

Then, for a source of angular radius θ_r , the electron density (n_e) and emission measure (EM) can be computed by

$$n_e = 3.113 \times 10^2 \left[\frac{S_\nu}{\text{Jy}} \right]^{0.5} \left[\frac{T}{10^4 \text{ K}} \right]^{0.25} \left[\frac{D}{\text{kpc}} \right]^{-0.5} b(\nu, T)^{-0.5} \theta_r^{-1.5} \text{ cm}^{-3} \quad (3.4)$$

and

$$EM = 5.638 \times 10^4 \left[\frac{S_\nu}{\text{Jy}} \right] \left[\frac{T}{10^4 \text{ K}} \right] b(\nu, T) \theta_r^{-2} \text{ cm}^{-6} \text{ pc}, \quad (3.5)$$

respectively. Zhao et al. (2010) estimated the kinetic temperatures in the mini-spiral arms using the H92 α radio recombination line and radio continuum emission at 1.3 cm to be in the range 5000-13,000 K. With the temperatures corresponding to the regions selected from the radio maps, I determined the emission measures and electron temperatures from the radio continuum fluxes using the formalism described above. Electron density values range from 0.8-1.5 $\times 10^4$ cm $^{-3}$ for the regions, with the highest electron densities and emission in the IRS 13 region, which is in agreement with previously published results (Brown et al. 1981; Zhao et al. 2010). The results are tabulated in Table 3.3.

3.2.2 Spectral index

The spectral index α is given by

$$\alpha = \frac{\log(S_1/S_2)}{\log(\nu_1/\nu_2)}, \quad (3.6)$$

where S_1 and S_2 are the flux densities at $\nu_1=230$ GHz and $\nu_2=100$ GHz, respectively. In order to obtain a spectral index map between the two wavelengths, the following steps were performed using *Miriad*:

- Convolve the maps at 3 and 1.3 mm to a common lower resolution of

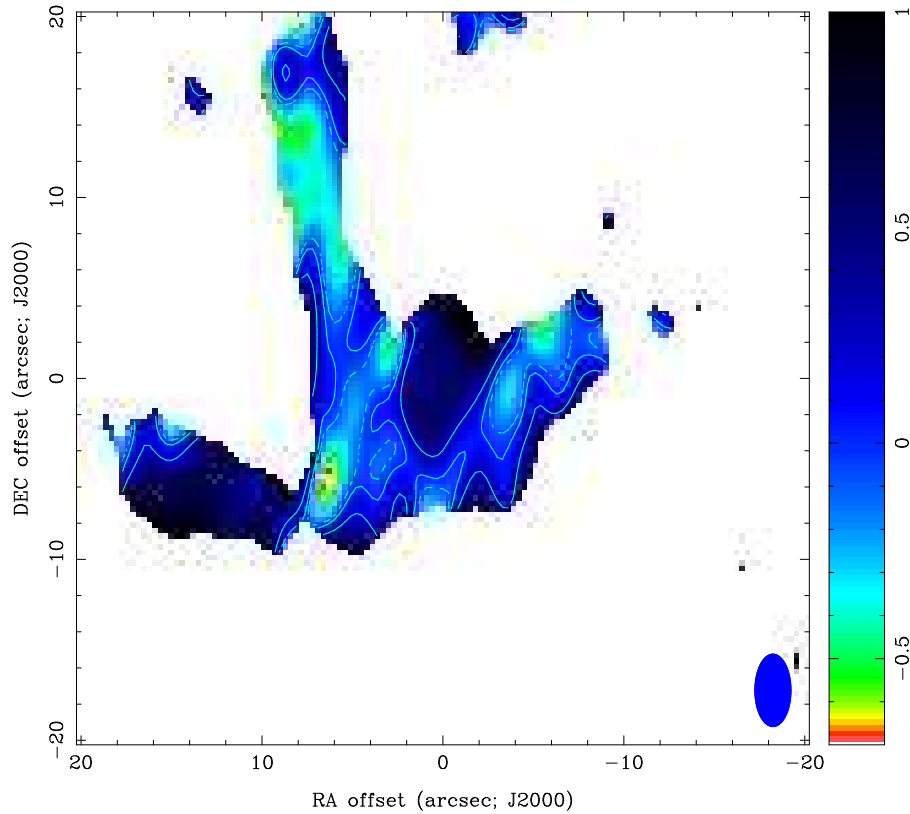


Figure 3.7: Spectral index map of the inner GC region. Contours indicate spectral indices of -0.1 (dashed), 1.0, and 0.4 (line). Sgr A* has an inverted synchrotron spectral index of 0.5.

$4'' \times 2''$ (p.a.= 0°)

- Apply a primary beam correction using the primary beam sizes of $82.5''$ and $36''$ at 3 mm and 1.3 mm, respectively
- Shift the maps to align them accurately with each other
- Create masked images at both frequencies using a flux density cutoff of 0.01 Jy, and multiply the two masked images to obtain a final masked image

Applying the final masked image to the radio maps and using the spectral index equation above, a spectral index map of the region was created, shown in Fig. 3.7. The masking process is to ensure that the flux densities and hence the spectral index values in Fig. 3.7 are well-defined at all points inside the masked region. From the above equation, the uncertainty in the spectral index values is derived to be

$$\delta\alpha = \left[\frac{1}{\ln(\nu_1/\nu_2)} \right] \times \sqrt{(\delta S_1/S_1)^2 + (\delta S_2/S_2)^2}. \quad (3.7)$$

The spectral index map covers the inner $40'' \times 40''$ of the GC region, which includes the Northern Arm, Eastern Arm, the Bar and the central bright radio source Sgr A*.

The spectral index of Sgr A* of $\alpha \approx 0.5 \pm 0.25$ is in good agreement with previously published results in Falcke et al. (1998) and Yusef-Zadeh et al. (2006b), and is indicative of an inverted synchrotron spectrum, as is expected from a non-thermal source. The mini-spiral region exhibits a more interesting spectral index behaviour with a mixture of positive and negative values. For an optically thin region emitting Bremsstrahlung, a thermal spectral index of ~ -0.1 is expected, which is seen around the Bar and parts of the Northern Arm in the spectral index map. Regions of steeper spectral index of ~ -0.5 are also seen, which are indicative of non-thermal emission. However, this could be the result of unresolved flux in the 1.3 mm map, especially in the more extended regions of the Northern Arm. The presence of a positive spectral index in most of the Eastern Arm, and around the edges of the Bar, on the other hand, is an indication of excess emission in the 1.3 mm map.

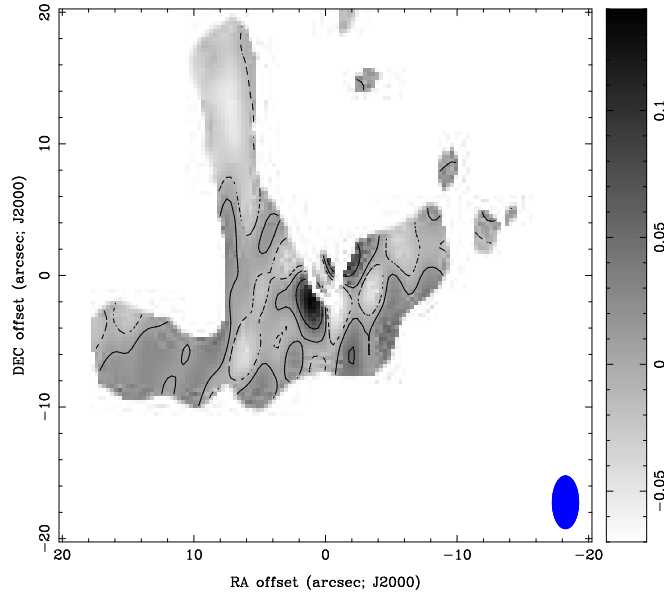


Figure 3.8: 1.3 mm excess emission (compared to Bremsstrahlung). See text for details of subtraction of free-free emission. The contour levels represent -0.01 (dashed), 0.01 and 0.05 (line) Jy/beam.

Assuming the 3 mm emission is purely free-free emission, the 3 mm map was scaled by a factor of 0.92 (obtained using the relation $S_1 = S_2(\nu_1/\nu_2)^\alpha$) to obtain a pure free-free emission map at 1.3 mm. This is subtracted from the original 1.3 mm map to produce a residual map (Fig. 3.8) which shows the regions of excess emission (compared to Bremsstrahlung) in the Eastern Arm and parts of the Bar, corresponding to the regions of positive spectral index in the spectral index map. This excess emission could be due to dust emission, which starts to become important at wavelengths ≤ 1 mm (Zylka & Mezger 1988), possibly from large dust grains (Draine & Lee 1984; Fich & Hodge 1991).

Comparison to other spectral index maps

The spectral index map presented in Fig. 3.7 is the highest resolution spectral index map obtained at mm-wavelengths so far. In the radio regime, Ekers et al. (1975) have published a spectral index map between 6 cm and

20 cm. They report a non-thermal spectral index of -0.3 for the diffuse emission from Sgr A West, and a thermal spectrum for the Sgr A West spiral, in comparison to the spectral indices in Fig. 3.7. However, the spiral features are not well-resolved and Mezger et al. (1989) show that the thermal emission could become optically thick at $\lambda \geq 6$ cm. In the sub-mm regime, García-Marín et al. (2010) presented maps of the inner 37×34 pc² of the GC region, which includes the CNB and surrounding molecular clouds. Their derived temperature maps of this region reveal dust temperatures between 10 and 20 K in the CNB and molecular clouds and spectral index maps of the same region indicate spectral indices ranging from -0.8 to 1.0, which has been explained with a combination of dust, synchrotron and free-free emission. In the regions immediately surrounding Sgr A*, they derived spectral indices of $-0.6 < \alpha < 0.0$, which was explained as a combination of 70-90% synchrotron and 10-30% dust and free-free emission. This is in good agreement with the results presented here.

3.2.3 MIR map

Thermal emission from the dust in the mini-spiral dominates the MIR continuum map at $8.6 \mu\text{m}$. The dust and ionized gas in the mini-spiral are closely associated with each other, with a strong correlation reported between the dust emission at MIR ($12.4 \mu\text{m}$) wavelengths and the ionized gas emission at radio wavelengths (VLA 2 cm) by Gezari & Yusef-Zadeh (1991). The positions of several point sources such as IRS 1, 2 and 9 coincide in both maps. However, significant displacements occur in the positions of IRS 13 and 21, which have been explained as being caused by dust displacement due to stellar winds. This correlation is confirmed by the high resolution radio continuum and MIR maps presented here, with the radio continuum map tracing out the dust features in the mini-spiral quite well (Fig. 3.9). The 3 mm radio map with a synthesised beam of size $1''$ and the $8.6 \mu\text{m}$ map were transformed to the same pixel scale of $0.075''$, and using the position of Sgr A* in the radio map and in the MIR map (from Schödel et al. (2007)), aligned with each other. The positions are accurate to within $0.075''$. Fig. 3.9 shows the MIR map overlaid with the 3 mm radio map.

From Hildebrand (1983), the dust mass of a region of flux density $F(\nu)$,

at a distance D from the observer is given by

$$M_d = \frac{F(\nu)D^2}{B(\nu, T_d)} \frac{4a}{3Q(\nu)} \rho, \quad (3.8)$$

where a , $Q(\nu)$ and ρ are the dust parameters grain size, emissivity and grain density, respectively and $B(\nu, T)$ the Planck function at dust temperature T_d . The dust grain parameters are taken to be $a=0.1 \mu\text{m}$, $\rho=2 \text{ gm}^{-3}$ and $Q(\nu)=10^{-2}$ for the mini-spiral region from Rieke et al. (1978), and an overall dust temperature of 300 K (Gezari & Yusef-Zadeh 1991) is assumed. The calculated dust masses along with the MIR fluxes are given in Table 3.3. A total dust mass of $0.01M_\odot$ was obtained for the mini-spiral region. The errors in flux density are obtained using (3.1).

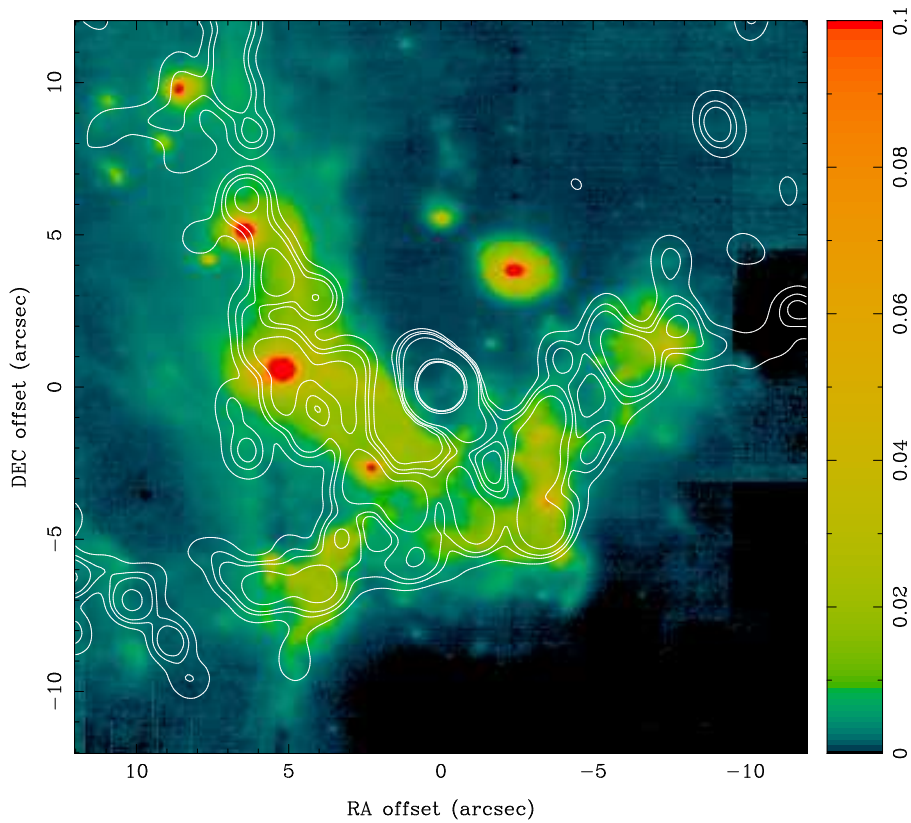


Figure 3.9: MIR $8.6 \mu\text{m}$ map (units of Jy/pixel) overlaid with a 3 mm map of synthesised circular beam size of $1''$. Contour levels are at 0.0090 , 0.015 , 0.02 , 0.035 , 0.3 , 0.4 , $0.45 \text{ Jy}/\text{beam}$.

3.2.3.1 Dust to gas ratio

Using the procedure described in the previous section, the MIR and 3 mm radio continuum maps were aligned, and by dividing the MIR map by the radio continuum map, a dust-to-gas brightness ratio map was obtained, which is shown in Fig. 3.10. The darker regions correspond to higher ratios of dust-to-gas, while the lighter regions correspond to lower ratios. The values range from about ~ 10 in the IRS 13 region to ~ 100 - 140 in the IRS 1W and 10W regions in the Northern Arm. This indicates higher amounts of dust in the Northern Arm compared to the Bar, which is consistent with the explanation that the ionized bar of the mini-spiral is dust depleted due to a combined outflow/wind from the central ionizing source Sgr A* and the stars in the region (Gezari & Yusef-Zadeh 1991).

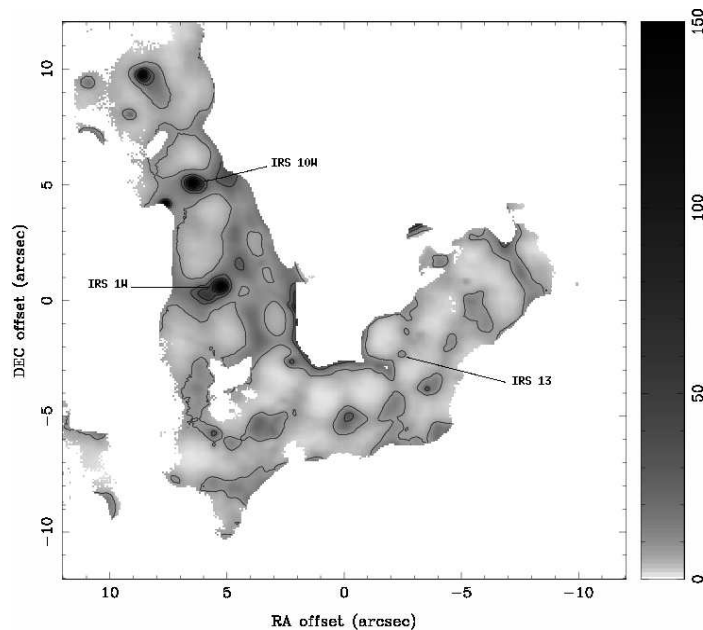


Figure 3.10: Dust to gas ratio map - High at IRS 10W, and IRS 1W (Northern Arm), low at IRS 13 (Bar).

3.2.4 NIR Brackett γ map

The Br γ emission line at $2.16\ \mu\text{m}$ traces out ionized gas in the mini-spiral region, which is the same as that seen in the radio continuum maps at 3 mm. At $2.2\ \mu\text{m}$, most of the background continuum is from the stars in the region, and the free-free emission contribution to the continuum radiation is negligible (Neugebauer et al. 1978). Hence, after removing the strong stellar sources in the Br γ map using the point source subtraction described in Sect. 3.1.3, a good estimate of the emission line fluxes in this region is obtained.

The expected Br γ line intensity can be estimated from the 5 GHz radio continuum flux density using the formula (Glass 1999)

$$I(\text{Br}\gamma) = 2.71 \times 10^{-14} \left[\frac{T}{10^4 \text{ K}} \right]^{-0.85} \left[\frac{\nu}{\text{GHz}} \right]^{0.1} F_\nu, (\text{Jy}) \text{ Wm}^{-2} \quad (3.9)$$

where T is the electron temperature and F_ν is the flux density at frequency ν .

The 3 mm map was scaled to 6 cm (5 GHz) using $S_1 = S_2(\nu_1/\nu_2)^\alpha$ by assuming an optically thin free-free emission spectral index of -0.1 between 5 GHz and 100 GHz. Using this 5 GHz map, the expected Br γ intensity map was derived. The optical depth is given by

$$\text{Br}\gamma_{\text{observed}} = e^{-\tau} \text{Br}\gamma_{\text{expected}} \quad (3.10)$$

and the extinction at wavelength $\lambda=2.16\ \mu\text{m}$ is

$$A_\lambda = 2.5\tau \log_{10} e. \quad (3.11)$$

The extinction map at $\lambda=2.16\ \mu\text{m}$ is shown in Fig. 3.11. Extinction values range from 2.5-3.2 mag in the mini-spiral region, with a mean extinction of 2.77 ± 0.23 mag. This is in good agreement with Schödel et al. (2009) and Buchholz et al. (2009), who report median extinction values of $A_{K_s}=2.74 \pm 0.30$ mag and $A_K=3.1 \pm 0.4$, respectively, using H-K colours. Brown et al. (1981) and Scoville et al. (2003) also derived extinction values from the radio continuum emission and the Br γ and Pa α line emission, respectively, which are also in agreement with the values calculated here.

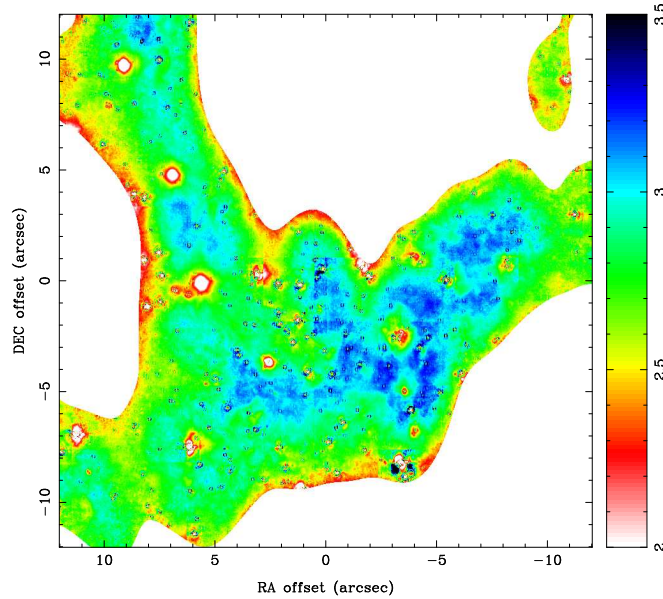


Figure 3.11: Extinction map derived from observed and expected $Br\gamma$ map (from radio continuum fluxes).

Using the relation $A_{2.2\mu\text{m}}/A_V=0.105$ (from the extinction curve of Cardelli et al. 1989), corresponding extinctions were obtained in the visual ranging from $A_V=25\text{-}32$ mag with a scaled error of 2.2 derived from the error of A_K .

Following Ho et al. (1990), the number of ionizing photons is calculated from the expected $Br\gamma$ flux densities using

$$N(\text{Lyc}) = 2.9 \times 10^{45} \left[\frac{D}{\text{kpc}} \right]^2 \left[\frac{S}{10^{-12} \text{ ergs s}^{-1} \text{ cm}^{-2}} \right], \quad (3.12)$$

which are calculated and tabulated in Table 3.3. These values ranging from $1.8\text{-}3.4 \times 10^{50} \text{ photons s}^{-1}$ are in agreement with the value of $3 \times 10^{50} \text{ photons s}^{-1}$ obtained by Zhao et al. (2010).

Region	$S_{1\text{mm}}$ $\pm 0.03\text{ Jy}$	$S_{3\text{mm}}$ $\pm 0.03\text{ Jy}$	$S_{8.6\ \mu\text{m}}$ $\pm 5\text{ Jy}$	$S_{\text{Br}\gamma}$ $\pm 0.015\text{ Jy}$	EM $\pm 0.8 \times 10^6\text{ cm}^{-6}\text{ pc}$	n_e $\pm 0.3 \times 10^4\text{ cm}^{-6}$	N_{Lyc} $\pm 0.6 \times 10^{50}\text{ s}^{-1}$	M_{dust} $\pm 0.0002\text{ M}_{\odot}$
1	0.16	0.24	20.9	0.096	9.87	1.46	3.43	0.0009
2	0.11	0.13	16.2	0.042	2.25	0.99	2.08	0.0008
3	0.19	0.16	23.6	0.080	6.62	1.19	2.57	0.0011
4	0.15	0.16	46.6	0.125	3.86	1.12	2.48	0.0022
5	0.09	0.10	21.6	0.062	2.51	0.89	1.48	0.0010
6	0.12	0.12	16.6	0.049	5.51	1.04	1.79	0.0008

Table 3.3: Fluxes from different wavelengths, calculated emission measures, electron densities, dust masses and number of ionizing photons for selected regions from the mini-spiral.

Chapter 4

Flaring Model of Sgr A*

4.1 Modelling

As mentioned in Chapter 1, Sgr A* is found to be highly variable at almost all wavelengths, from the NIR and X-ray to radio and sub-mm wavelengths. The simultaneous nature of the NIR/X-ray flares is indicative of the fact that the same population of electrons is responsible for emission at both wavelengths. And the observations of radio/sub-mm flares a few hours after the NIR/X-ray flares indicates that there is a link between the flaring activity at these wavelengths. Several models have been used to explain this flaring behaviour of Sgr A*, as explained in Chapter 1. In this thesis, I use a model with synchrotron and synchrotron self-Compton (SSC) components revolving around the SMBH on a temporary accretion disk to describe the behaviour of Sgr A* from IR to radio wavelengths. This model allows us to account for the NIR flux densities from both synchrotron and SSC components. The source components which peak in the THz domain are upscattered by SSC processes to the NIR/X-ray regimes, and expand adiabatically to give rise to a delayed radio/sub-mm emission, as will be explained below.

4.1.1 Synchrotron self-Compton theory

Using the nomenclature adopted by Gould (1979) and Marscher (1983), we assume a synchrotron source of angular size θ , with $R_s = 2R_g = 2GM/c^2 \sim 8 \mu\text{as}$, where R_s and R_g are the Schwarzschild radius and gravitational radius of the SMBH respectively. Therefore, an angular diameter of $\sim 8 \mu\text{as}$ at a distance of 8 kpc from us corresponds to a size of one R_s . We assume a standard power law distribution of electrons

$$N(E) = N_o E^{-(2\alpha+1)} (\gamma_1 mc^2 < E < \gamma_2 mc^2) \quad (4.1)$$

and an optically thin spectral index α corresponding to

$$S_\nu \propto \nu^{-\alpha}, \quad (4.2)$$

where S_ν is the flux density at frequency ν (the source becomes optically thick at a frequency ν_m known as the turnover or cutoff frequency with a flux density S_m). Then taking into account the relativistic bulk motion of the source with respect to an observer with a Doppler boosting factor $\delta = \Gamma^{-1}(1 - \beta \cos \phi)^{-1}$ where ϕ is the angle of the velocity vector to the line of sight, β is the velocity in terms of the speed of light (v/c), and $\Gamma = (1 - \beta^2)^{-1/2}$ for the bulk motion, the magnetic field strength B is given by

$$B \propto \theta^4 \nu_m^5 S_m^{-2}. \quad (4.3)$$

Scattering by the same electron population gives rise to an inverse Compton scattered flux density S_{SSC} given by

$$S_{\text{SSC}} \propto \ln(\nu_2/\nu_m) \theta^{-2(2\alpha+3)} \nu_m^{-(3\alpha+5)} S_m^{2(\alpha+2)} E_{\text{keV}}^{-\alpha}, \quad (4.4)$$

where E_{keV} is the X-ray photon energy (described in Marscher (1983)). Within the limits E_{min} and E_{max} corresponding to the wavelengths λ_{max} and λ_{min} the SSC spectrum has the same spectral index as the upscattered synchrotron components, i.e., $S_{\text{SSC}} \propto E_{\text{keV}}^{-\alpha}$. A Lorentz factor of the order of $\gamma_e \sim 10^3$ of the emitting electrons is required to produce the observed flux in the X-ray domain, for which the upper synchrotron cut-off frequency ν_2 lies within the NIR bands. Thus, most of the NIR spectrum can be explained by synchrotron emission, while the inverse Compton emission explains the X-ray emission (supported by SSC models in Markoff et al. (2001); Yuan et al. (2003); Eckart et al. (2004)).

4.1.2 Relativistic spot/disk modelling of NIR flares

The NIR light curves may be caused by a single hot spot orbiting the SMBH several times or by multiple spots with individual lifetimes shorter than one orbital period very close to the last stable orbit of the SMBH. In the case of a single spot, if this spot sinks or moves towards the centre while orbiting, then the emission of the spot will dominate the red-noise emission of the disk by causing a quasi-periodic modulation of the light curve. And in the case of multiple hot spots, the quasi-periodic modulation will exhibit a frequency closer to the frequency of the last stable orbit (see discussion in Eckart et al. 2008a and Eckart et al. 2006b). The quasi-periodic modulation is smeared out if the hot spots expand within an accretion disk or form the source of a short outflow above the disk, which may be undetectable at lower radio/sub-mm observing frequencies. This model can be linked to the adiabatic expansion of synchrotron components in the case of a source expansion, as is described in the following sections.

4.1.2.1 Multi-component disk model

Using the SSC model described above, we describe the time dependent flaring activity of Sgr A* with a multi-component disk model involving a number of synchrotron and SSC emitting source components revolving around the SMBH in a temporary accretion disk.

The low and high flux density states of the model give the boundary values for quantities of the source components such as the turnover frequency ν_m , flux density S_m and source size θ , described by a power law, as given by

$$N(S) \propto S_m^{\alpha_S}, \quad (4.5)$$

$$N(\nu) \propto \nu_m^{\alpha_\nu}, \quad (4.6)$$

$$N(\theta) \propto \theta^{\alpha_\theta}, \quad (4.7)$$

where $N(S)$, $N(\nu)$ and $N(\theta)$ are the number distributions of the components and α_S , α_ν and α_θ are the corresponding exponents.

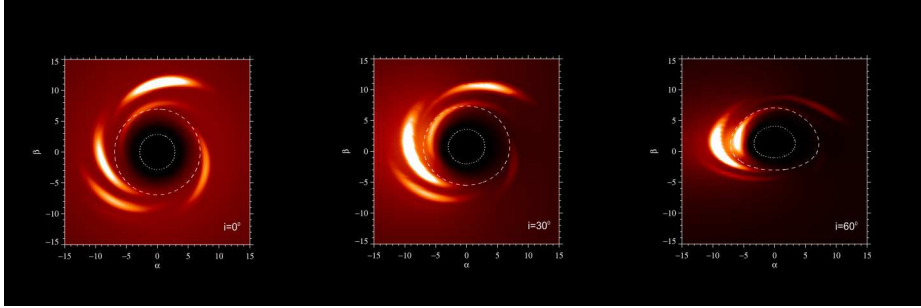


Figure 4.1: Simulated images of multiple spots revolving around a black hole, projected on the observer's image plane (α, β) , viewed at three inclination angles $i=0^\circ$, 30° and 60° , with respect to the common rotation axis. The dotted and dashed circles represent the event horizon and the marginally stable orbit, respectively (Zamaninasab et al. 2010).

Using a reference frame of an observer at the black hole, light amplification curves for each individual component orbiting the SMBH are produced by the KY-code (Dovčiak et al. (2004)). This code takes into account relativistic effects such as redshift, lensing, time delays, changes in the emission angle and polarization angle, etc. It also uses the concept of a transfer function (Cunningham 1975), which relates the flux seen by a local observer co-moving with the accretion disk to the flux seen by an observer

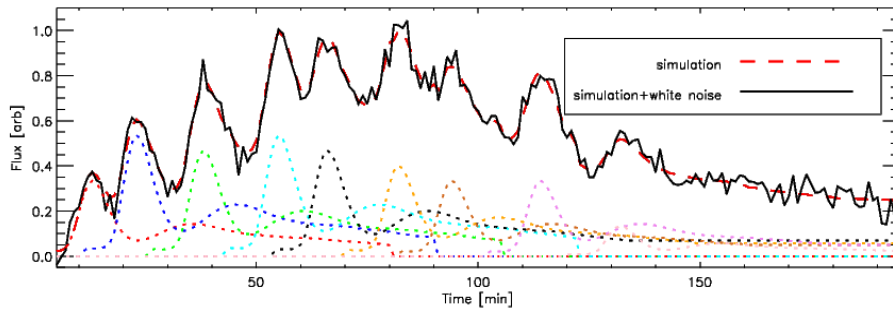


Figure 4.2: Light curve obtained from the multiple spot simulations shown above for a particular inclination, with the solid black line giving the overall light curve and different coloured dashed lines showing the contributions of individual spots (Zamaninasab et al. 2010).

at infinity. Combining these curves with the SSC model described above, we can estimate flux densities in the NIR and X-ray domain and magnetic fields. Fig. 4.1 shows snapshots of simulations of the accretion disk with multiple spots revolving around the SMBH. The light curve produced by these simulations at a particular inclination is shown in Fig. 4.2. With this model the small flux density variations (at time scales ~ 20 minutes) are produced when spots pass behind the SMBH in their first cycle around it. Then, while they shrink they get slowly disrupted by the differential rotation of the accretion disk, contributing marginally to the overall flare event.

4.1.3 Adiabatic expansion modelling of the mm/sub-mm emission

Almost all reported flare detections from multiwavelength campaigns of the Galactic centre so far have observed radio/sub-mm flares delayed by an hour or so compared to the NIR/X-ray events (Eckart et al. 2006a, 2008b; Yusef-Zadeh et al. 2009, 2006a,b, 2008; Marrone et al. 2008). If the events in the NIR/X-ray and radio/sub-mm were unrelated, we can expect to see an equal number of flares in the radio/sub-mm before the NIR/X-ray events as we would after the NIR/X-ray events. Hence we can safely assume that the radio/sub-mm events are in fact related to the higher frequency events. An adiabatic expansion of the synchrotron components used in the SSC model described in Section 4.1.1 has been used to explain the flaring activity of Sgr A* in the radio/sub-mm regime occurring with a time lag of $\sim 1.5 \pm 0.5$ hours (Eckart et al. 2006a, 2008b; Yusef-Zadeh et al. 2006a). I describe the adiabatic expansion model used to model the data in this thesis in the following section.

4.1.3.1 Adiabatically expanding source components

A quantitative description of a model involving synchrotron source components that are initially optically thick and expand with time to become optically thin at longer wavelengths was presented by van der Laan (1966).

Using this formalism we describe the adiabatic source components and develop a time-dependent model to study their behaviour at different frequencies.

We assume a compact, uniform spherical blob of radius R consisting of relativistic electrons with an isotropic velocity distribution and a power law energy distribution $n(E) \propto E^{-p}$. The blob is assumed to be optically thick at all radio frequencies initially. As the blob expands uniformly, the magnetic field declines as R^{-2} , energy as R^{-1} , and density as R^{-3} .

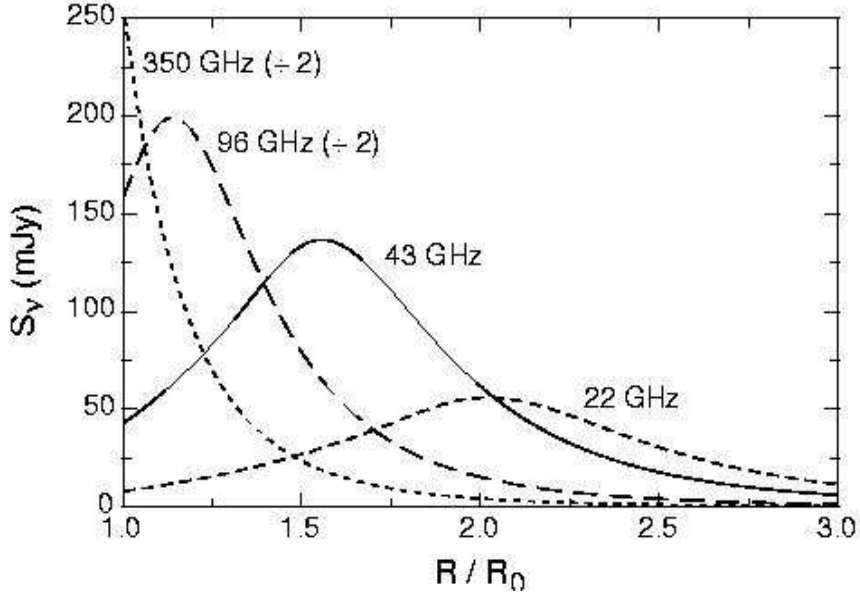


Figure 4.3: Flux behaviour for an expanding component at different frequencies in the adiabatic expansion model (Yusef-Zadeh et al. 2006b).

If ν_0 is the peak frequency or cutoff frequency at which the source becomes optically thick, R_0 , S_0 , and τ_0 give the size, flux density and the optical depth of the source at this frequency, respectively. Then the optical depth and flux density at any given frequency ν scales as

$$\tau_\nu = \tau_0 \left(\frac{\nu}{\nu_0} \right)^{-(p+4)/2} \left(\frac{R}{R_0} \right)^{-(2p+3)} \quad (4.8)$$

and

$$S_\nu = S_0 \left(\frac{\nu}{\nu_0} \right)^{5/2} \left(\frac{R}{R_0} \right)^3 \frac{1 - \exp(-\tau_\nu)}{1 - \exp(-\tau_0)}, \quad (4.9)$$

respectively. We define τ_0 to be the optical depth corresponding to the frequency at which flux density is maximum, in order to combine the SSC formalism with the adiabatic expansion model. This makes τ_0 dependent only on the particle spectral index p through the condition

$$e^{\tau_0} - \tau_0(p + 4)/5 - 1 = 0. \quad (4.10)$$

Thus, if p ranges from 1 to 3, the corresponding τ_0 ranges from 0 to 0.65. This gives us the variation in flux density at any frequency as a function of the expansion factor (R/R_0) for a given spectral index p and peak flux density S_0 at a frequency ν_0 , as shown in Fig. 4.3. Then, as the bulk of relativistic electrons expands, the emission becomes optically thin at lower frequencies and lower flux densities.

Assuming a simple linear expansion model with a constant expansion speed of v_{exp} such that $R - R_0 = v_{\text{exp}}(t - t_0)$, we can convert the dependence on radius to a dependence on time. At times $t < t_0$, the source is assumed to have an optical depth that is equal to its frequency dependent initial value τ_0 at $R = R_0$. In the optically thin part of the spectrum, the flux initially increases with increasing source size at a constant optical depth τ_0 and then decreases with decreasing optical depth as it expands. And for times $t > t_0$, the decaying flank of the light curve can be stretched to later times by increasing the turnover frequency ν_0 or the initial source size R_0 , or by decreasing the spectral index α_{synch} or peak flux density S_0 . The peak of the light curve can also be shifted to earlier times by increasing the adiabatic expansion velocity v_{exp} . At lower frequencies, flare time scales are longer and decay at a slower rate as a result of adiabatic expansion.

Chapter 5

Modelling of May 2007 and 2008 flares

Simultaneous observations of the Galactic centre at wavelengths ranging from NIR/X-ray to the radio/sub-mm is the best strategy for observing the flaring activity of Sgr A*, and understanding the physical processes behind this activity. With this objective in mind, we have organized extensive multi-frequency campaigns in May 2007 and 2008. The data I present in this thesis are from the observing campaigns in May 2007 and 2008 which included millimetre single dish and interferometer arrays such as CARMA (Bock et al. 2006), ATCA, and the MAMBO bolometer at the IRAM 30 m telescope, and the ESO VLT in the NIR. This chapter explains the data reduction steps, including a new algorithm to extract the flux density of Sgr A* from the surrounding extended emission from mm light curves, the modelling of the data using the SSC model in combination with an adiabatic expansion framework explained in the previous chapter, and summarises briefly the results obtained from the modelling.

5.1 Observations and data reduction

5.1.1 The mm data

Table 5.1 gives a log of the observations at different wavelengths in the mm regime. We observed the Galactic centre with the radio interferometer array CARMA at 3 mm (100 GHz) in May 2007 and 2008. The quasar source 3C273 was used for bandpass calibration while 1733-130 and Uranus were used for phase and amplitude calibration of Sgr A*. The ATCA observations at 3.5 mm (86 GHz) in May 2007 used the calibrator sources 1253-055, 1921-293, and Uranus for bandpass, phase, and amplitude calibration. The data reduction package *Miriad* was used to reduce and map both the CARMA and ATCA data. Fig. 5.1 shows the BCD array 3 mm map obtained from the combined 2007 and 2008 data. The 1.2 mm MAMBO 2 bolometer array data were reduced using the bolometer array data reduction, analysis and handling software package, the BoA (Bolometer Data Analysis).

Sgr A* is surrounded by the mini-spiral and the CND, which consists of gas and dust. Radio interferometric observations in the mm/sub-mm allow us to differentiate the flux density contribution of Sgr A* from the thermal emission of these extended regions.

Extracting the light curve

Even after calibrations are performed, the radio interferometric data may be influenced by residual baseline and atmospheric effects. To extract reliable light curves of Sgr A* from this data and to correct for the extended flux density contributions from the mini-spiral, I developed an algorithm using medians of baseline visibilities. This algorithm performs the following steps. From the two interferometer arrays, two pairs of orthogonal long baselines were selected and visibilities for each baseline for each day were extracted. These visibilities were calibrated with intermittent flux reference observations. The median visibility for each baseline for all four days was calculated and subtracted from each individual data set for the correspond-

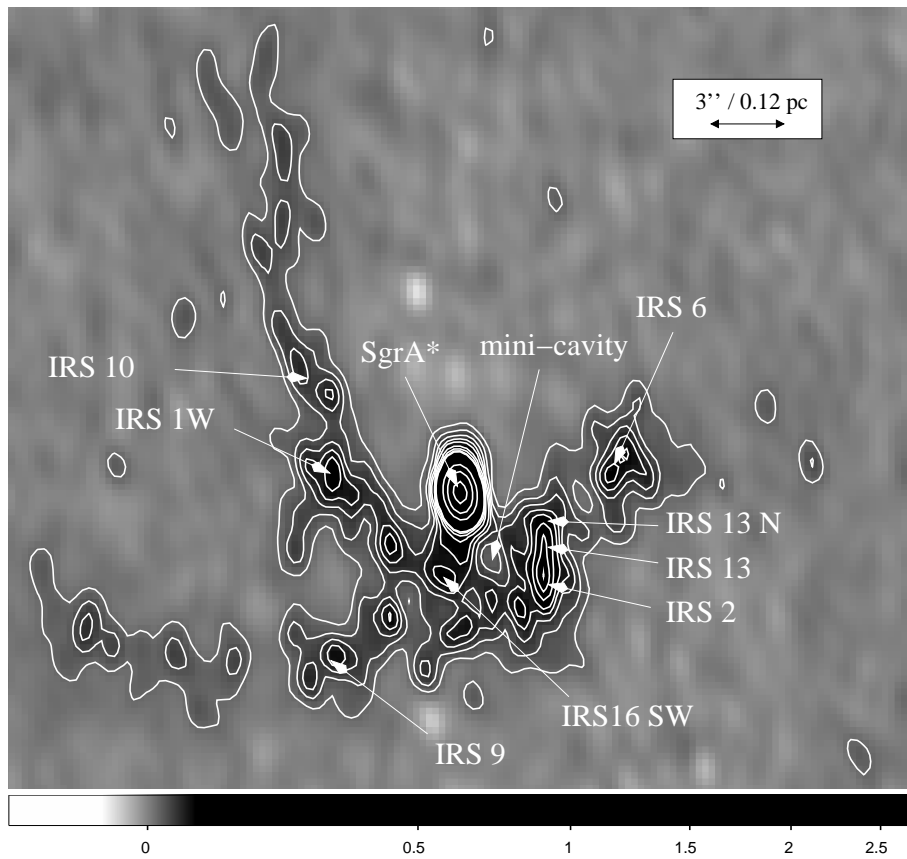


Figure 5.1: Combined BCD array 3mm map of $0.15''$ resolution (Kunneriath et al. 2010).

Telescope Observing ID	Instrument/ Array	λ (mm)	UT and JD Start Time	UT and JD Stop Time
ATCA	H214	3.5	2007 15 May 07:36:05 JD 2454235.81672	15 May 22:57:02.5 JD 2454236.45628
IRAM 30 m	MAMBO bolometer	1.2	2007 16 May 00:20:42 JD 2454236.51437	16 May 04:18:56 JD 2454236.67981
CARMA	D array	3.0	2007 16 May 07:43:31.3 JD 2454236.82189	16 May 13:27:07.8 JD 2454237.06051
ATCA	H214	3.5	2007 16 May 09:31:57.5 JD 2454236.89719	16 May 22:21:22.5 JD 2454237.43151
IRAM 30 m	MAMBO bolometer	1.2	2007 17 May 00:14:39 JD 2454237.51017	17 May 04:28:13 JD 2454237.68626
CARMA	D array	3.0	2007 17 May 07:22:46 JD 2454237.80748	17 May 13:20:43 JD 2454238.05605
ATCA	H214	3.5	2007 17 May 09:47:17.5 JD 2454237.90784	17 May 18:22:32.5 JD 2454238.26565
IRAM 30 m	MAMBO bolometer	1.2	2007 18 May 00:12:57 JD 2454238.50899	18 May 04:23:03 JD 2454238.68267
CARMA	D array	3.0	2007 18 May 07:33:21.8 JD 2454238.81484	18 May 13:19:20.3 JD 2454239.05510
ATCA	H214	3.5	2007 18 May 10:11:27.5 JD 2454238.92462	18 May 22:23:47.5 JD 2454236.67981
CARMA	D array	3.0	2007 19 May 07:30:52.3 JD 2454239.81311	19 May 13:15:42.8 JD 2454240.05258
ATCA	H214	3.5	2007 19 May 09:30:57.5 JD 2454239.89650	19 May 22:13:07.5 JD 2454240.42578
CARMA	C array	3.0	2008 26 May 06:45:13 JD 2454612.78140	26 May 13:10:43 JD 2454613.04911

Table 5.1: Log of the mm- and sub-mm observations.

ing baseline. The median of visibilities from all four baselines for each day then gives the differential flux light curve for each day.

After this procedure is completed, the variations in the light curve can then be attributed to variations in the intrinsic flux density of Sgr A*, since the contribution of extended flux remains constant and is removed by this median baseline subtraction method.

Mathematically, this can be expressed in the following way. The median baseline and time dependent visibility trend

$$D_b(t) = \mu_{\text{epoch}}(d_b(t)) \quad (5.1)$$

was subtracted from each visibility data set $d_b(t)$, where the operator μ_{epoch} represents the median over all epochs. The time-dependent differential visibilities $S(t)$ and their uncertainties $\delta S(t)$ are then given by

$$S(t) = \mu_b(d_b(t) - D_b(t)) \quad (5.2)$$

and

$$\delta S(t) = \mu_b(S(t) - (d_b(t) - D_b(t))). \quad (5.3)$$

Here the operator μ_b is the median over different baselines. Hence, $\delta S(t)$ is the median of the deviation from the median flux $S(t)$.

To be able to combine data from different frequencies in a single light curve, the spectral index of Sgr A* should not vary significantly between 86 GHz and 250 GHz. If S_1 and S_2 are the flux densities at frequencies ν_1 and ν_2 such that

$$\log S_1 = \log S_2 + \alpha (\log \nu_1 - \log \nu_2) \quad (5.4)$$

and the spectral index changes from α to $\alpha + \Delta\alpha$, the new flux density S'_1 is given by

$$\log S'_1 = \log S_2 + (\alpha + \Delta\alpha)(\log \nu_1 - \log \nu_2). \quad (5.5)$$

From the above equations,

$$\log \frac{S_1}{S'_1} = -\Delta\alpha \log \frac{\nu_1}{\nu_2} \quad (5.6)$$

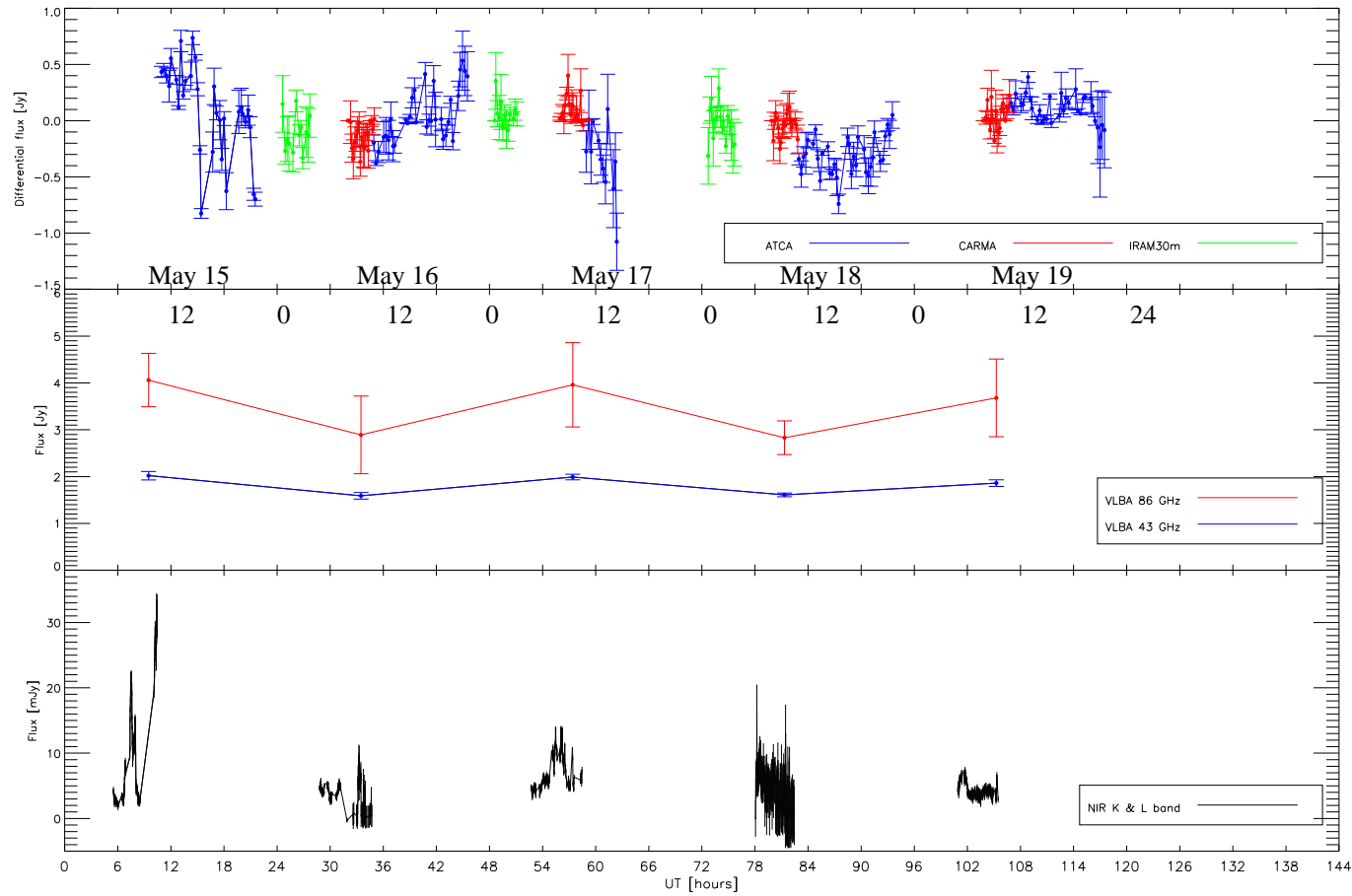


Figure 5.2: Top: Combined differential mm/sub-mm light curve of Sgr A*. Middle: Flux density averages from simultaneous VLBA observations (Lu et al. 2008, 2010). Bottom: Combined NIR light curve (K-band and L'-band). The time axis is labelled with UT hours starting at 00h on May 15.

or for $S'_1 = fS_1$

$$\log f = \Delta\alpha \log \frac{\nu_1}{\nu_2}. \quad (5.7)$$

From the radio to sub-mm measurements by Markoff et al. (2001) and Zhao et al. (2003), the spectral index variation is estimated to be $\Delta\alpha = 0.07$ between 10 GHz and 1000 GHz. The CARMA, ATCA and the IRAM 30 m telescope data covers a spectral range from 86 GHz to 250 GHz. This gives a maximum expected flux density variation of 8% in the light curve due to variations in the spectral index. The bulk of the data in which flux density variations are detected in the light curve are from the CARMA and ATCA telescope arrays, which are at frequencies 100 and 86 GHz, respectively, and follow the VLT data set in time. The 30 m telescope data, which precede the VLT data, does not exhibit significant flux density variations. Hence the maximum expected flux density variation in the light curve due to changes in spectral index can only be 0.005 Jy, which is smaller than $\delta S(t)$. The median flux density variation for each day for the CARMA and IRAM 30 m data is then $\delta S(t) \sim 0.1$ Jy and for the ATCA data $\delta S(t) \sim 0.2$ Jy. These values represent the approximate range in which these data sets can be freely shifted in flux density.

The uppermost panel in Fig. 5.2 shows the combined differential light curve from all three telescopes, along with the daily flux density averages of the 7 and 3 mm VLBA (Very Large Baseline Array) observations that were conducted in parallel with our observations in the middle panel (Lu et al. 2008; Kunneriath et al. 2008; Lu et al. 2010). The lower panel contains the combined NIR light curve consisting of K and L'-band light curves for the same epoch. The overall trend observed in the sub-mm/mm light curve obtained by CARMA, ATCA and the IRAM 30 m telescope is reflected in the VLBA light curve.

To verify the trend observed in the light curve, the following check was performed: From the CARMA data, which has the best combination of high resolution and signal-to-noise ratio of all the mm-telescopes used in this project, averaged maps for each day were produced. By subtracting a mean map (Fig. 5.3) from each averaged map, residual maps were obtained for all four days, shown in Fig. 5.4. The rms noise in these maps is of the order of 0.1 Jy/beam. These residual maps reflect the same trend seen in

the combined differential light curve (top panel in Fig. 5.2), in particular the excess flux density of ~ 0.4 Jy on May 17 and a slightly positive flux density on May 19. The mixture of negative and positive flux densities in the maps on the 16th and 18th of May 2007 corresponds to the non-detection of flaring activity in these epochs in Fig. 5.2.

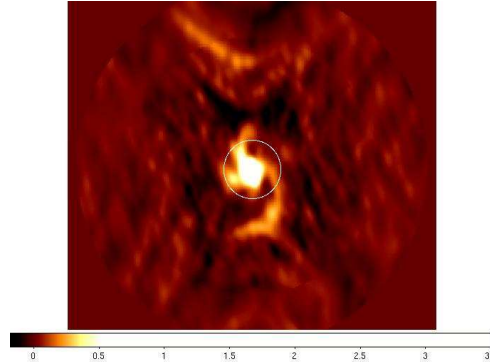


Figure 5.3: Mean map obtained from CARMA data (May 16-19).

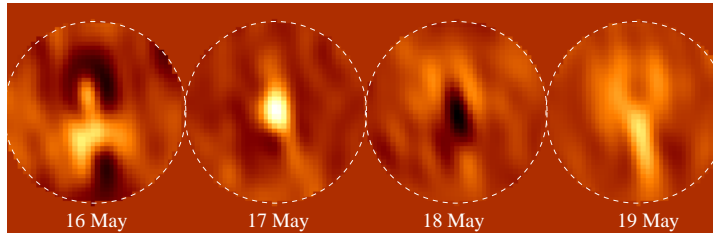


Figure 5.4: Residual maps at 3 mm of a $40''$ diameter region (shown by the dashed white line) centred on Sgr A*, obtained from the difference between full synthesis maps of the individual days of CARMA observations and the full CARMA data set as described in the text. The maps have been plotted with the same color-coding table.

5.1.2 The NIR data

The NIR observations in the K-band ($2.2 \mu\text{m}$, FWHM $0.35 \mu\text{m}$) and the L'-band ($3.8 \mu\text{m}$, FWHM $0.62 \mu\text{m}$) were taken using ESO's Very Large

Telescope (VLT) NACO infrared camera and adaptive optics (AO) system (Rousset et al. 2003; Lenzen et al. 2003) in Paranal, Chile. Table 5.2 gives the start and stop times of the observations. The integration times were $\text{NDIT} \times \text{DIT} = 200 \times 0.2 = 40$ seconds (DIT is Detector Integration Time, and NDIT is the number of DIT's) for the $3.8 \mu\text{m}$ observations and $\text{NDIT} \times \text{DIT} = 4 \times 10 = 40$ seconds for the $2.2 \mu\text{m}$ observations. The infrared wavefront sensor of NAOS was used to lock the AO loop on the NIR bright (K-band magnitude ~ 6.5) supergiant IRS 7, located about $5.6''$ north of Sgr A*. The Strehl ratio of a telescope is defined as the ratio of the observed peak intensity of a point source to the theoretical peak intensity value of the system at its diffraction limit. With a K-band diffraction limit of about 60 mas, the AO was able to provide a stable correction with a high Strehl ratio (of the order of 50%).

The standard data reduction steps of correcting for bad pixels, subtracting the sky and flat fielding were performed on the images and a point spread function (PSF) was extracted from each individual image using *StarFinder* (Diolaiti et al. 2000), after which a Lucy-Richardson (LR) deconvolution was applied. The beam was restored with a Gaussian beam with FWHM corresponding to ~ 60 mas at $2.2 \mu\text{m}$ and ~ 104 mas at $3.8 \mu\text{m}$. Aperture photometry was performed on the sources with circular apertures of radius 52 mas and extinction corrections of $A_K = 2.8$ and $A_{L'} = 1.8$ applied, to calibrate the flux with flux densities of known sources, and obtain the final flux densities of the sources in Jansky. This resulted in flux densities of the reference star S2 of 22 ± 1 mJy and 9 ± 1 mJy, respectively, which were used to measure the uncertainties in flux measurements of Sgr A*.

To combine the NIR K and L'-band data (as shown in Fig. 5.2 and Figs. 5.5 to 5.9), the L'-band data were scaled to K-band wavelengths using a scaling factor of 0.6. This scaling factor is obtained from the spectral index of -0.9 (Eckart et al. 2008b, 2009, Yusef-Zadeh et al. 2008). In the remaining figures given in this chapter, no scaling has been applied.

Telescope Observing ID	Instrument/ Array	λ (μm)	UT and JD Start Time	UT and JD Stop Time
VLT UT 4	NACO	2.2	2007 15 May 05:29:00 JD 2454235.72847	15 May 09:42:00 JD 2454235.90417
VLT UT 4	NACO	2.2	2007 16 May 04:47:22 JD 2454236.69956	16 May 07:54:41 JD 2454236.82339
VLT UT 4	NACO	2.2	2007 17 May 04:42:14 JD 2454235.69600	17 May 09:34:40 JD 2454235.89907
VLT UT 4	NACO	2.2	2007 19 May 04:55:00 JD 2454239.70486	19 May 09:28:22 JD 2454239.89470
VLT UT 4	NACO	3.8	2007 15 May 10:05:48 JD 2454235.92069	15 May 10:32:40 JD 2454235.93935
VLT UT 4	NACO	3.8	2007 16 May 08:28:34 JD 2454236.85317	16 May 10:44:04 JD 2454236.94727
VLT UT 4	NACO	3.8	2007 17 May 10:16:24 JD 2454237.92806	17 May 10:28:00 JD 2454237.93611
VLT UT 4	NACO	3.8	2007 18 May 06:03:26 JD 2454238.75238	18 May 10:29:05 JD 2454238.93686
VLT UT 4	NACO	3.8	2007 22 May 04:57:04 JD 2454242.70630	22 May 06:22:01 JD 2454242.76529
VLT UT 4	NACO	3.8	2007 23 May 04:39:08 JD 2454243.69384	23 May 10:36:24 JD 2454243.94194
VLT UT 4	NACO	3.8	2008 26 May 05:42:55 JD 2454612.73814	26 May 10:37:39 JD 2454612.94281

Table 5.2: Log of the near-infrared observations.

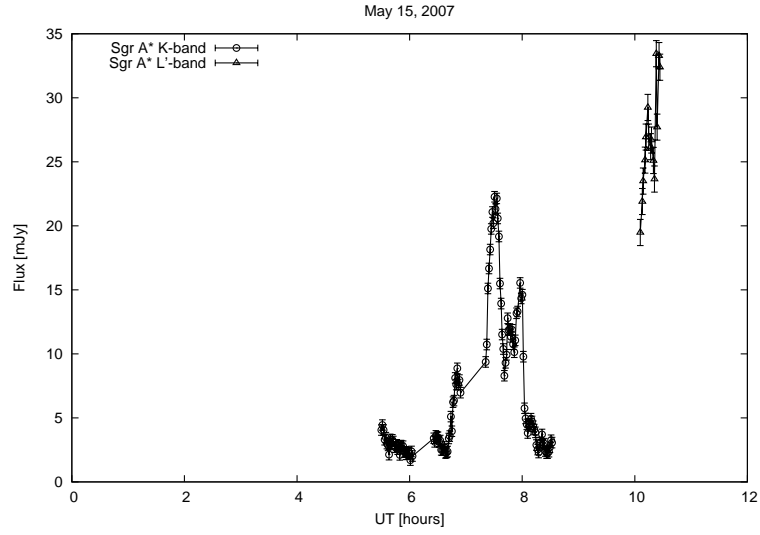


Figure 5.5: Observing time- K-band: 05:29:55 to 08:31:48, L'-band: 10:05:48 to 10:26:45.

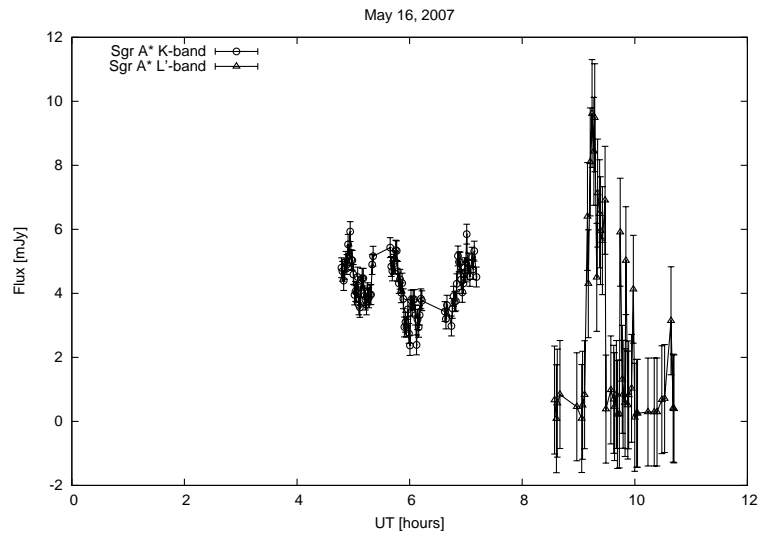


Figure 5.6: Observing time- K-band: 04:47:22 to 07:54:41, L'-band: 08:34:27 to 10:41:46.

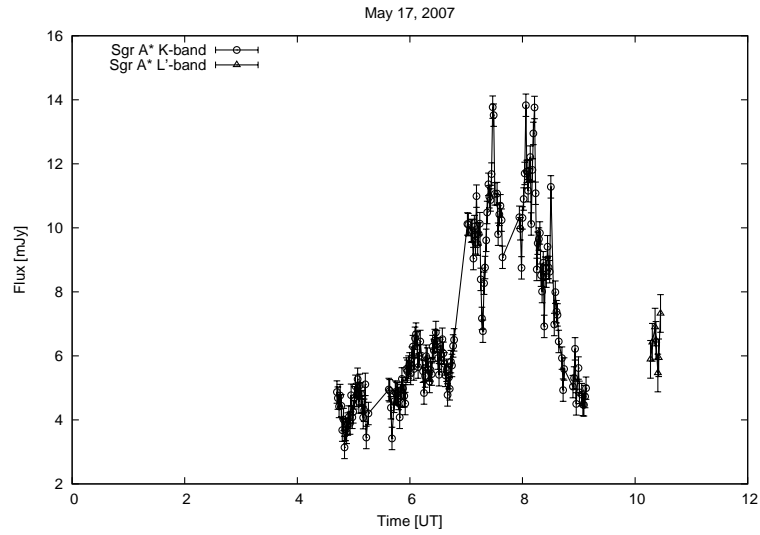


Figure 5.7: Observing time- K-band: 04:42:14 to 09:34:40, L'-band: 10:16:24 to 10:27:06.

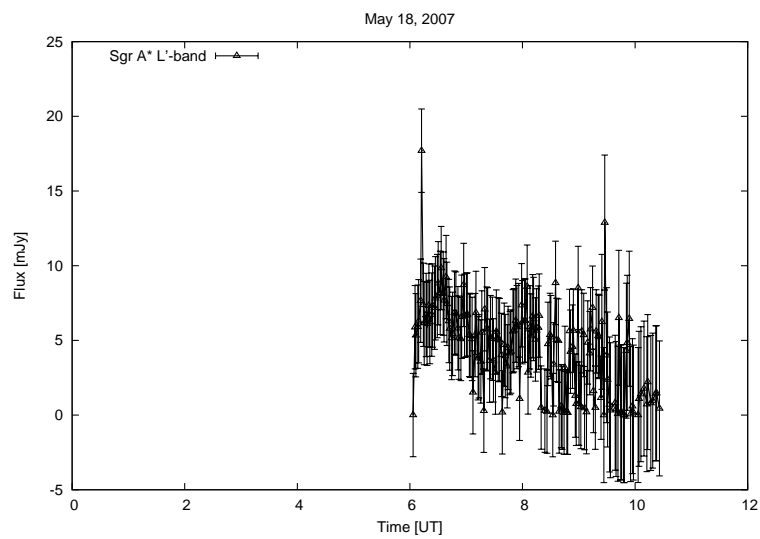


Figure 5.8: Observing time- L'-band: 06:03:26 to 10:26:00.

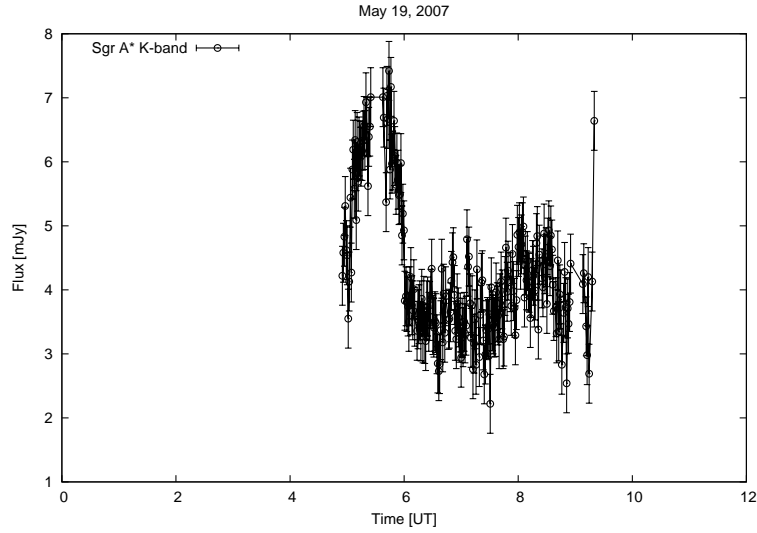


Figure 5.9: Observing time- K-band: 04:55:00 to 09:28:22.

5.2 Results and Analysis

The results of our multi-wavelength campaign are:

- A bright NIR flare on May 15 2007.
- A NIR flare on 17 May 2007 followed by a 0.4 Jy mm flare observed with CARMA.
- A NIR flare on 19 May 2007 with no flare detection in the mm light curve.
- A bright L'-band NIR light curve on 26 May 2008 with no flare detection in the mm light curve.

The above flare events were modelled using the adiabatic expansion model described in Chapter 4. The following sections describe the modelling of individual flare events, the results and analysis.

5.2.0.1 Adiabatic expansion modelling

The main parameters used in the model are the size R_0 (expressed in units of Schwarzschild radius R_s), expansion velocity v_{exp} , the optically thin spectral index α_{synch} and the flux density $S_{\text{max,obs}}$ at the cutoff or peak frequency $\nu_{\text{max,obs}}$ of the source component (adopting the nomenclature used in Eckart et al. (2006a, 2009)).

A reduced χ^2 fit was performed for the model for each flare event with a number of source components (denoted by N), which implies a total of N times 4 ($S_{\text{max,obs}}$, α_{synch} , R_0 , ν_{max}) plus a common expansion velocity v_{exp} and time offset (the time differences between the components are fixed), i.e., $4N+2$ degrees of freedom. Since certain factors like the width and peak of the light curve signature depend to a varying extent on all 4 parameters S_{max} , α_{synch} , R_0 , and ν_{max} , the model parameters cannot all be considered to be independent. Therefore a minimum number of source components were used to estimate the degrees of freedom. Since the VLT data contains ~ 10 times the number of data points in the CARMA data points in the 2007 data, the squared CARMA flux deviations and number of data points were weighted by an additional factor of 19. The χ^2 test was then performed with the sum of the squared flux deviations and data points of the VLT and CARMA datasets.

SSC modelling as an additional constraint

Since the model allows for NIR flux density contributions from both synchrotron and SSC components, an additional constraint is provided by the SSC model described in Sect. 4.1.2. The SSC contribution of the X-ray and NIR flux densities and the magnetic field can be estimated from the SSC model. A higher contribution of flux in the NIR from SSC components would violate the assumption that the synchrotron emission of the sub-mm (THz peaked) component is the main source of NIR flux density in the adiabatic expansion model, and require the modelling of the unknown X-ray flux density. The magnetic field can be calculated from

$$B \propto \theta^4 \nu_m^5 S_m^{-2}, \quad (5.8)$$

where ν_m and S_m are the synchrotron turnover frequency and flux density mentioned above. A $B \approx 70$ Gauss has been obtained from previously published results (Eckart et al. 2006a, 2008b; Yusef-Zadeh et al. 2008; Marrone et al. 2008), which should also not be violated in the model. The upper limits to flux densities of upscattered SSC components are represented by $S_{\text{NIR,SSC}}$ and $S_{\text{X-ray,SSC}}$ and the optically thin synchrotron flux density in the NIR is given by $S_{\text{NIR,synch}}$.

Adding to a single input parameter the 1σ uncertainty such that a maximum positive or negative flux density is reached results in an increase of $\Delta\chi = 1$ (from the reduced χ^2 value). A variation in the value of a single source component by its listed uncertainty results in a variation of the predicted model flux densities in the NIR and X-ray by more than 30%. Judging from the $\Delta\chi$ based on the mm-data alone, the global uncertainties for $S_{\text{max,obs}}$, α_{synch} , and R_0 may then be doubled. The flare events were modelled at a higher and lower expansion velocity labelled A and B.

5.2.1 Flare events

5.2.1.1 The 15 May 2007 flare event

The NIR data obtained on May 15 2007 did not have any overlap with the sub-mm/mm coverage which began nearly three hours after the NIR coverage ended. The NIR coverage captured a long underlying main flare with two significant flux density excursions which are termed 'sub-flares', centred at about 07:29 UT and 07:51 UT, respectively (see Fig. 5.5). The time difference of 22 minutes between these two sub-flares is consistent with previously reported sub-flare separations (Eckart et al. 2006b; Meyer et al. 2006), and the flux density levels between the two does not reach emission levels before and after the flare. The May 15 NIR flare has been extensively studied and analysed by Eckart et al. (2008a) who interpreted these substructures in the framework of spot evolution in a temporary accretion disk and Zamaninasab et al. (2010) who showed that these highly polarized sub-flares are part of the flare structure that is significant compared to randomly polarized red-noise. The brief L'-band observations at 10 UT show a NIR signal that is a factor of 2 times stronger than at other times.

The mm data begins nearly 3 hours after the NIR light curve. Flux density variations at mm wavelengths due to adiabatic expansion will not be sufficiently strong compared to median flux density variations in the data 3-4 hours after the NIR flare. Therefore, the flare can only be constrained by the NIR data. This flare was modelled using a background component β responsible for the main underlying flare and two components α and γ for the two strongest sub-flares. The expansion speed cannot be constrained in this case, but in model A a value of $0.007c$ close to the speed found for most of the modelled flares was used, and in model B, a higher speed of $0.017c$, lower spectral index and a weaker background component to obtain a good fit to the NIR data and fulfil the 100 GHz and the X-ray upper limits of flux density were used. Fig. 5.10 shows the May 15 2007 light curve fitted with the two models A and B, with the contributions of individual components highlighted in different colours. Table 5.3 summarises the model parameters described in Section 5.2.0.1, obtained from the model fits A and B.

The L'-band data at 10 UT (refer Fig. 5.5) could be correlated to the radio data, but the light curve is not long enough to justify being included in the modelling in this case. However, higher flux density levels are generally preceded by a positive flux density excursion in the mm-domain in the framework of the adiabatic expansion model, which is not evident here. This could be explained by the high L'-band flux being caused by a transient steeper infrared spectral index, indicating either a significantly higher turnover frequency or stronger synchrotron losses.

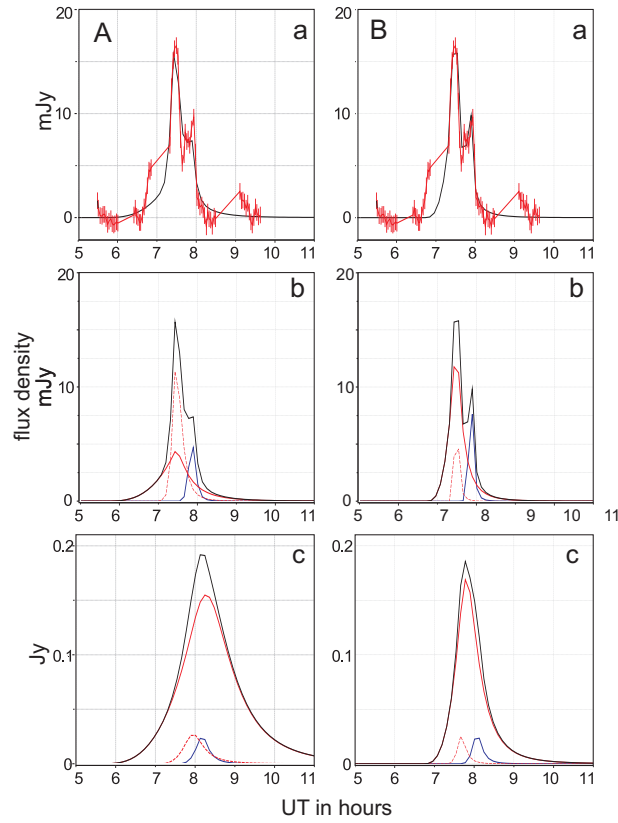


Figure 5.10: Models A and B of the 15 May 2007 NIR flare: a) Fitted NIR light curve, with the black curve corresponding to the model and the red curve corresponding to the data, b) Contribution of individual source components to NIR light curve, and c) Contribution of individual source components to mm light curve.

date	model label	source	Δt hours	v_{exp} in c	$S_{\text{max,obs}}$ [Jy]	α_{synch}	R_0 [R_s]	$\nu_{\text{max,obs}}$ [GHz]	B [G]	$S_{\text{NIR,synch}}$ [mJy]	$S_{\text{NIR,SSC}}$ [mJy]	$S_{\text{X-ray,SSC}}$ [nJy]
$1 \sigma \rightarrow$			± 1.0	± 0.001	± 0.1	± 0.1	± 0.1	± 250	± 10	± 1.0	± 1.0	± 20
15 May 2007	A	α	0.0	0.007	0.6	0.85	1.3	340	33	3.1	<0.03	<10
		β	0.0		0.3	0.60	0.3	840	29	12	<0.03	<10
		γ	0.30		0.3	0.75	0.2	840	32	5.6	<0.03	<10
15 May 2007	B	α	0.0	0.017	0.6	0.65	1.3	340	37	8.3	<0.02	<40
		β	0.0		0.3	0.65	0.3	840	30	8.4	<0.02	<40
		γ	0.37		0.3	0.65	0.35	810	32	8.4	<0.02	<40

Table 5.3: Source component parameters for the combined SSC and adiabatic expansion model of the 15 May 2007 flare. Labels A and B refer to models with lower and higher expansion velocities, respectively. The flare times Δt are given with respect to the peak of the brighter NIR flares. In addition to v_{exp} , the R_0 values are responsible for the position and width of the infrared flare peaks in time. Different values for α_{synch} are required to match the infrared flux densities.

5.2.1.2 The 17 May 2007 flare event

On May 17 2007 the NIR flare had a clear overlap with the 3 mm CARMA observations, with indications of a 0.4 Jy flare following a NIR flare. The differential light curve obtained from the four longest baselines of CARMA and ATCA along with the NIR light curve is shown in Fig. 5.11. A cross-correlation between the two shows a time lag of 1.5 ± 0.5 hours with a significant, broad and positive peak corresponding to the flares found at both wavelengths. The negative power seen in the cross-correlation is most likely due to a combination of two effects:

- The poorer signal-to-noise ratio of the differential ATCA data compared to the CARMA data, and
- Residual power on time scales of the length of the sub-mm datasets. Some amount of negative power is also expected when dealing with differential light curves which measure variation in flux with respect to a median flux level over the entire length of the dataset.

If the cross-correlation is performed with only the K-band NIR and CARMA data, a significant, broad and positive cross-correlation peak centred at 1.5 ± 0.5 hours still remains.

In order to verify that the variation in flux seen in the CARMA data is not related to a variation in calibrator flux densities, a cross-correlation between the calibrator and source fluxes from the CARMA data was performed, shown in Fig. 5.12. This therefore indicates that a 0.4 Jy 3 mm flare followed the NIR flare.

The NIR K-band data is dominated by four sub-flares, while the mm-data is dominated by a single flare that is wider than the individual NIR sub-flares, due to the expansion and subsequent overlap of sub-flares from individual source components. Since the May 17 2007 flare is constrained by the NIR and CARMA data, the time lag of 1.5 ± 0.5 hours determines the expansion velocity (Fig. 5.13). A constant flux density of 0.003 Jy was

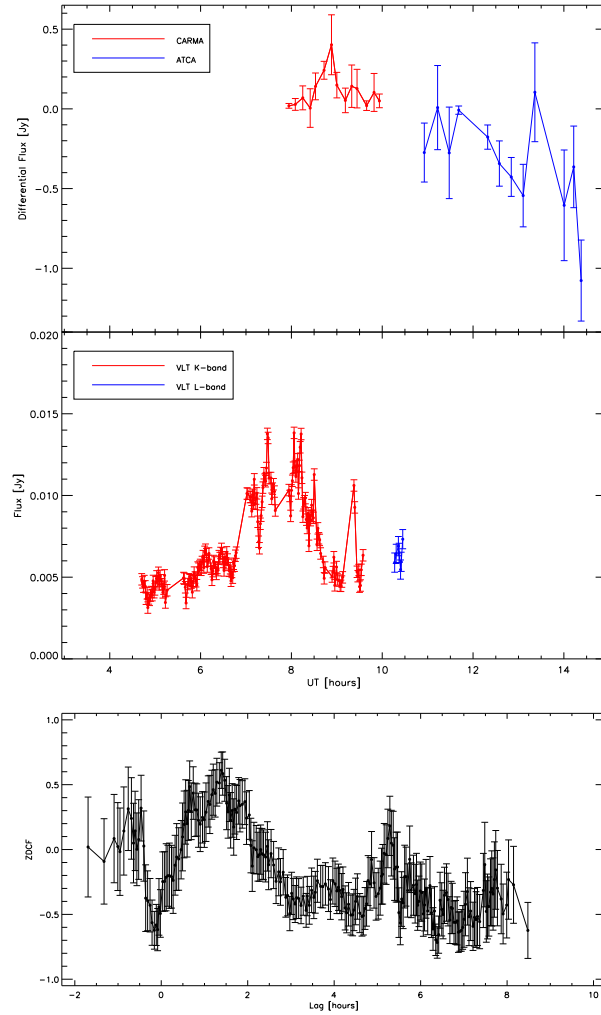


Figure 5.11: The 3 mm CARMA and ATCA (top red and blue, respectively) and K- and L'-band NIR (middle red and blue, respectively) light curves of the 17 May 2007 flare, with the cross-correlation (bottom) between the two showing that the mm flare follows the NIR flare with a time lag of 1.5 ± 0.5 hours. ZDCF stands for Z-transformed discrete correlation function.

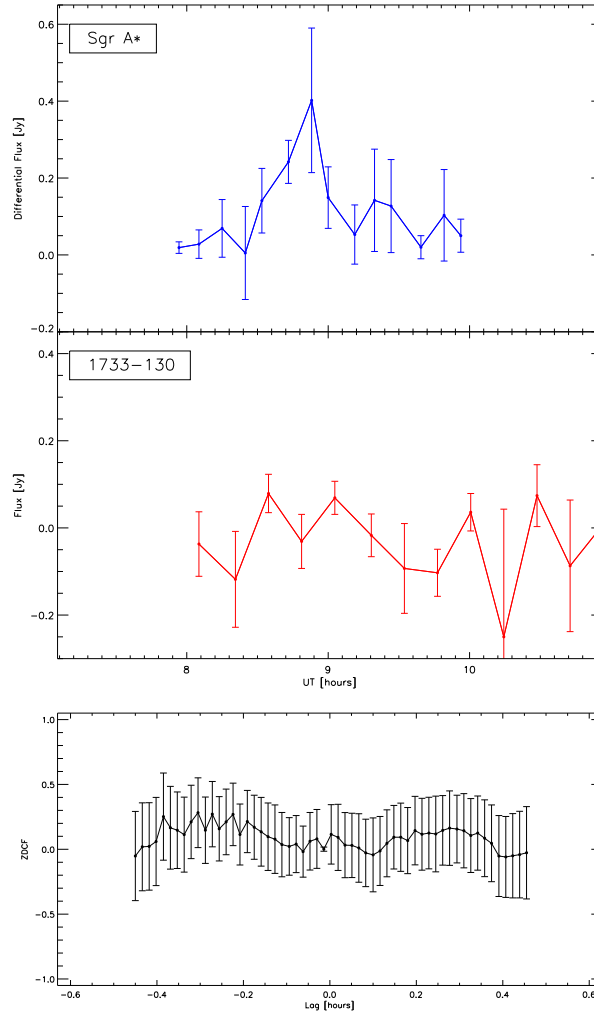


Figure 5.12: 3 mm CARMA Sgr A* (top) and calibrator (1733-130) (middle) light curves from 17 May 2007, with the cross-correlation (bottom) between the two showing zero correlation between the calibrator and the source fluxes.

date	model label	source	Δt hours	v_{exp} in c	$S_{\text{max,obs}}$ [Jy]	α_{synch}	R_0 [R_s]	$\nu_{\text{max,obs}}$ [GHz]	B [G]	$S_{\text{NIR,synch}}$ [mJy]	$S_{\text{NIR,SSC}}$ [mJy]	$S_{\text{X-ray,SSC}}$ [nJy]
17 May 2007	A	α	0.0	0.010	1.0	1.00	0.8	840	66	4.7	<0.01	<10
		β	0.45		0.5	0.97	0.3	1250	66	4.0	<0.01	15
		γ	-0.59		1.3	1.11	1.0	840	69	3.2	<0.01	<10
		δ	-0.96		0.5	1.02	0.3	1250	68	3.2	<0.01	12
17 May 2007	B	α	0.0	0.011	0.25	0.70	0.2	1360	86	8.1	<0.01	19
		β	0.36		0.25	0.70	0.2	1360	86	8.1	<0.01	19
		γ	-0.69		0.17	0.70	0.2	1360	65	5.1	<0.01	21
		δ	-1.05		0.17	0.70	0.2	1360	65	5.1	<0.01	21
		ϵ	-0.33		1.75	1.05	1.6	570	68	7.1	<0.01	<2

Table 5.4: Same as Table 5.3, but for May 17, 2007.

subtracted from the NIR data to model the sub-flare events. The two modelling approaches A and B are presented in Table 5.4. Four components α through δ representing the four sub-flares events were used in model A. For model B on the other hand, motivated by the relativistic disk

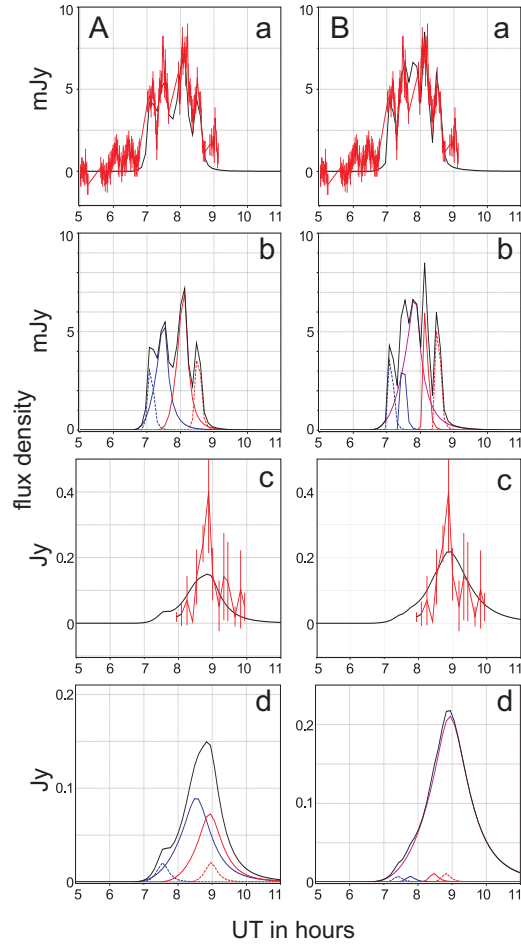


Figure 5.13: Models A and B of the 17 May 2007 NIR flare: a) Fitted NIR light curve, with the black curve corresponding to the model and the red curve corresponding to the data, b) Contribution of individual source components to NIR light curve, c) Fitted mm light curve, with the black curve corresponding to the model and the red curve corresponding to the data, and d) Contribution of individual source components to mm light curve.

modelling referred to in Sect. 4.1.2, an additional background component ϵ located close to the centre of the overall NIR flare along with additional components to model the sub-flares were used. Model B has lower values of $S_{\text{max,obs}}$ and the spectral index α_{synch} , smaller source component sizes R_0 , and higher cutoff frequencies $\nu_{\text{max,obs}}$ for components α through δ when compared to model A. The quality of the fit is comparable for models A and B.

5.2.1.3 The 19 May 2007 flare event

The 19 May 2007 flare in the NIR is only partially constrained by the CARMA mm data. In the NIR, two flare events of peak flux density 3.5 mJy and 1.1 mJy are separated by about 3 hours, with a gap in the observations when the first event reaches its peak flux density (refer Fig. 5.9 which implies that the true peak was probably missed and that the flare was probably brighter than 3.5 mJy. The mm data has an overlap of about 1.5 hours with the NIR data with no detection of a flare event brighter than 0.1-0.2 Jy.

Model A with a slower adiabatic expansion velocity of $0.007c$ allows to fit the first event (centred on the NIR at $\sim 5:30$ UT) with a single component (Fig. 5.14). For the higher velocity used in model B, a larger number of sources are needed to model the NIR data. For both models, the second flare event (centred on the NIR at $\sim 8:20$ UT) is constrained by the 3 mm CARMA data, giving upper limits of about 0.1-0.2 Jy to the flux density above which no millimetre flare event was detected for both flare components (at $\sim 5:30$ UT and $\sim 8:20$ UT). Model parameters are tabulated in Table 5.5.

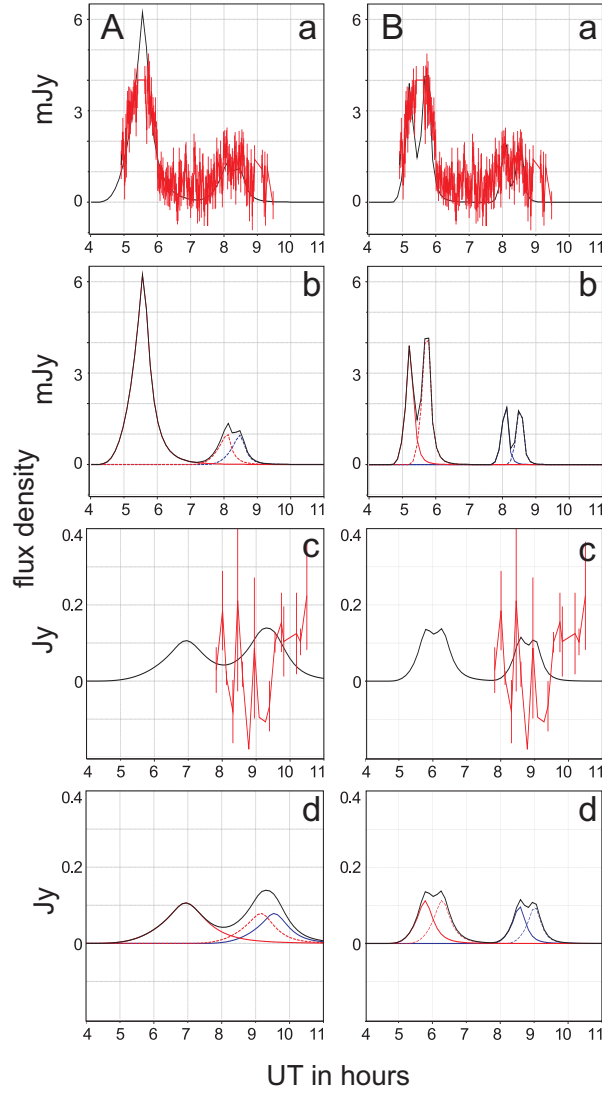


Figure 5.14: Models A and B of the 19 May 2007 NIR flare: a) Fitted NIR light curve, with the black curve corresponding to the model and the red curve corresponding to the data, b) Contribution of individual source components to NIR light curve, c) Fitted mm light curve, with the black curve corresponding to the model and the red curve corresponding to the data, and d) Contribution of individual source components to mm light curve.

date	model label	source	Δt hours	v_{exp} in c	$S_{\text{max,obs}}$ [Jy]	α_{synch}	R_0 [R_s]	$\nu_{\text{max,obs}}$ [GHz]	B [G]	$S_{\text{NIR,synch}}$ [mJy]	$S_{\text{NIR,SSC}}$ [mJy]	$S_{X\text{-ray,SSC}}$ [nJy]
19 May 2007	A	α	0.0	0.007	1.30	1.07	1.0	1360	67	3.5	<0.01	<10
		β	2.50		1.10	1.10	0.8	1360	67	0.5	<0.01	<10
		γ	2.90		1.10	1.10	0.8	1360	67	0.5	<0.01	<10
19 May 2007	B	α	0.0	0.017	1.33	1.13	1.0	720	68	2.5	<0.01	<10
		β	0.50		1.33	1.09	1.0	720	67	3.1	<0.01	<10
		γ	2.85		1.50	1.30	0.8	820	72	1.2	<0.02	<10
		δ	3.30		1.50	1.30	0.8	850	72	1.2	<0.02	<10

Table 5.5: Same as Table 5.3, but for May 19, 2007.

5.2.1.4 The 26 May 2008 flare event

The 26 May 2008 NIR flare in the L'-band is one of the brightest flares observed, with a flux density increase of about 70 mJy, followed by a plateau of almost constant flux density of 40 mJy before finally reaching the original flux density level of 20 mJy after nearly 200 minutes. The CARMA data on 26 May were taken under moderate to poor weather conditions, with the source visibility levels comparable to the 2007 observing session levels from 07:10 UT to 11:10 UT, followed by deteriorating weather conditions resulting in strong coherence losses. From 07:10 UT to 11:10 UT, however, no flare was detected within a limit of 0.2 Jy.

To be able to model the initially bright flare with sharp rising and falling

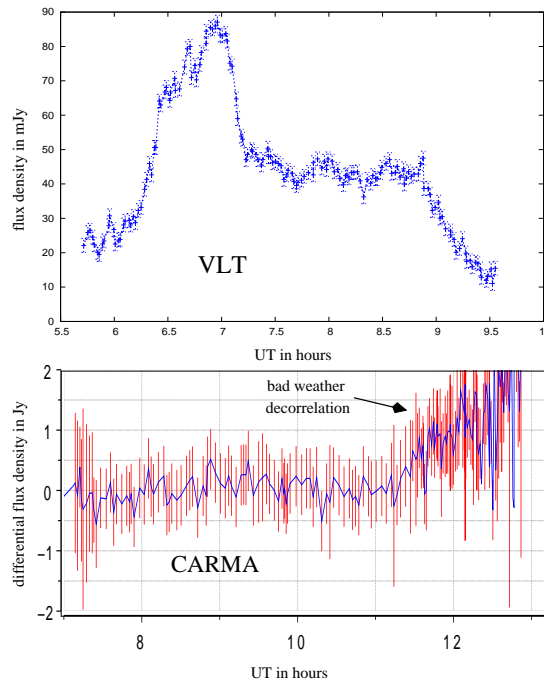


Figure 5.15: $3.8\mu\text{m}$ NIR flare (top) covered by 3 mm CARMA data (bottom) on the 26 May, 2008. The time coverage of the L'-band flare is from 05:42:55 to 10:37:39 UT.

flanks, followed by a 1.5 hour plateau requires the use of several source components each covering a maximum portion of time of about 30 minutes. A reduction in the number of sources would require much larger source components which in turn results in higher magnetic fields and a violation of the flux density limits given by the 3 mm CARMA data. Given these difficulties, the number of source components is of course not unique and the models proposed in Table 5.6 can only be taken as an example. The overall flare structure is quite similar to the flare described in Eckart et al. (2008b), observed with the APEX sub-mm bolometer and the VLT, the only difference being the continuous structure of the 26 May flare compared to the 3 June flare. Similar flare structures have been reported previously by Eckart et al. (2006a, 2009). A possible common physical structure behind these flares could be a disk structure expanded by differential rotation within the

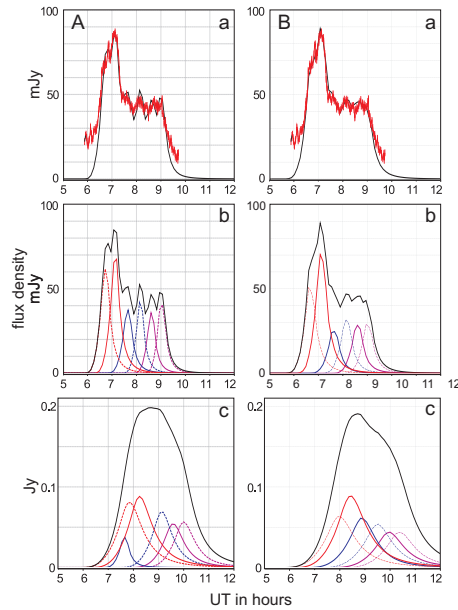


Figure 5.16: Models A and B of the 26 May 2008 NIR flare: a) Fitted NIR light curve, with the black curve corresponding to the model and the red curve corresponding to the data, b) Contribution of different source components to NIR light curve, and c) Contribution of different source components to mm light curve.

date	model label	source	Δt hours	v_{exp} in c	$S_{\text{max,obs}}$ [Jy]	α_{synch}	R_0 [R_s]	$\nu_{\text{max,obs}}$ [GHz]	B [G]	$S_{\text{NIR,synch}}$ [mJy]	$S_{\text{NIR,SSC}}$ [mJy]	$S_{\text{X-ray,SSC}}$ [nJy]
26 May 2008	A	α	0.0	0.005	1.1	0.68	0.5	1090	30	31	<0.02	41
		β	-0.45		1.0	0.68	0.5	1090	40	26	<0.02	18
		γ	0.52		1.0	0.83	0.5	1030	31	15	<0.02	17
		δ	1.03		1.0	0.80	0.5	1160	34	17	<0.03	23
		ϵ	1.48		0.8	0.77	0.5	1160	48	16	<0.01	<10
		ζ	1.90		0.8	0.77	0.5	1160	48	16	<0.01	<10
		26 May 2008	B		α	0.0	0.007	1.4	0.70	0.6	1090	44
β	-0.40			1.3	0.70	0.6		1090	56	35	<0.02	13
γ	0.52			1.1	0.77	0.6		1030	36	23	<0.02	18
δ	1.03			1.3	0.80	0.5		1160	33	23	<0.04	33
ϵ	1.48			1.0	0.77	0.5		1160	58	20	<0.01	<10
ζ	1.90			1.0	0.73	0.5		1160	56	24	<0.01	<10

Table 5.6: Same as Table 5.3, but for May 26, 2008.

disk, or accretion or magnetic field instabilities, maybe even within a jet structure (see Eckart et al. (2008b,a)). The model fits are shown in Fig. 5.16.

5.3 Flare analysis

From the adiabatic expansion modelling of the flares observed on May 15, 17 and 19 2007 and May 26 2008, I obtain expansion velocities ranging from $0.005c$ - $0.017c$, which are in agreement with previously published results (eg., Yusef-Zadeh et al. (2008); Eckart et al. (2008b)). The relativistic sound speed in orbital velocity near the SMBH is given by $c/\sqrt{3}$, which is much higher than the velocities obtained with this modelling. This could be explained by the bulk motion of source components with velocities larger than the expansion velocity v_{exp} or by a confinement of expanding material to the immediate region surrounding Sgr A* in the form of a disk or a corona. In the latter case, differential rotation within the accretion disk may cause shearing which is then responsible for the low velocities (Eckart et al. 2008b; Zamaninasab et al. 2008; Pecháček et al. 2008). As explained in Sect. 4.1.2, the expansion of several strong spots in the disk or corona can cause the smearing out of the short-term modulation observed in the NIR in the sub-mm/radio domain, implying that the quasi-periodic modulation may not be observable at all wavelengths.

Chapter 6

Summary and conclusions

In this chapter, I summarise the main results of my Ph.D thesis which have been described in detail in the previous chapters, including an outcome of the analysis of the GC mini-spiral physical properties derived from a multiwavelength dataset, and the flaring emission of Sgr A*.

After the reduction of radio interferometry observations of the Galactic Centre region at millimetre wavelengths obtained from local mm-telescope arrays such as CARMA and ATCA, and the IRAM 30 m telescope at mm-wavelengths, the main results obtained were

- High resolution maps of the mini-spiral region and Sgr A* at 100 GHz and 230 GHz from CARMA observations.
- The highest resolution spectral index map of the mini-spiral region at such high frequencies, obtained from the 100 GHz and 230 GHz maps.
- The long light curve of the compact radio source Sgr A* from the 15-19th of May, 2007 in the mm-regime obtained using a new method to combine light curves from both interferometers and single dish telescopes omitting flux density contributions from the extended emission in the galactic centre region.

By combining this data with infrared data obtained with the VLT telescopes, the results obtained were

- The physical properties of the ISM of the GC mini-spiral for selected regions, and an extinction map at the NIR K band.
- The detection and modelling of simultaneous flaring activity in the NIR and mm-regime with the May 2007 and 2008 observing campaigns using an adiabatic expansion model with a SSC formalism.

6.1 Discussion and Outlook

6.1.1 Mini-spiral region

I have studied the properties of the mini-spiral at multiple wavelengths, including radio continuum maps at 3 and 1.2 mm, MIR continuum at $8.6 \mu\text{m}$ and the Br γ line emission at $2.16 \mu\text{m}$.

The spectral index map of the region indicates a mixture of various emission mechanisms in the central few parsecs of the GC, with an inverted synchrotron spectrum of ~ 0.5 of Sgr A*, thermal free-free emission spectral indices of -0.1 , and a possible contribution of dust emission as indicated by the positive thermal indices ~ 1.0 . The positive spectral indices may be attributed to a possible dust contribution which begins to show up at wavelengths ≤ 1.2 mm, probably from large dust grains (Draine & Lee 1984).

For selected regions in the mini-spiral arms, I extract flux densities from the different wavelengths and infer the following:

- Physical properties of the ionized gas such as emission measure and electron densities ranging from $0.8\text{-}1.5 \times 10^4 \text{ cm}^{-3}$ from the 3 mm radio continuum map.
- Dust masses from the $8.6 \mu\text{m}$ MIR map, with a total dust mass contribution of $0.01 M_{\odot}$ from the mini-spiral arms, and a dust-to-gas

brightness ratio map indicating dust depletion along the Bar, with higher ratios along the Northern Arm.

- Extinctions of 1.8-3.2 at $2.16\ \mu\text{m}$ from a comparison of observed Br γ flux densities to the expected flux densities inferred from the free-free radio emission and the Lyman continuum emission rate derived from the expected Br γ flux density.

Future continuum and spectral line observations of the mini-spiral at mm/sub-mm wavelengths with arrays of high resolution and sensitivity such as ALMA will reveal more extended emission in the central few parsecs of the Galactic centre, and show more structure in the mini-spiral arms, including the mini-cavity region, and confirm the influence of dust emission at wavelengths $\leq 1.2\ \text{mm}$.

6.1.2 Flares of Sgr A*

I present results from global coordinated multiwavelength observational campaigns carried out in 2007 and 2008 using NACO at VLT in the NIR K- and L'-bands, and CARMA, ATCA, and IRAM in the mm regime.

A new method to obtain concatenated light curves of the compact mm-source Sgr A* after removing the significant flux density contributions from an extended, partially resolved source by combining data from single dish telescopes and interferometers was presented in this thesis. Consecutive datasets from each participating observatory are required for this method. Four different flaring events were discovered in the NIR, with three of these events also covered later in the mm-wavelength.

This flaring activity was modelled with an adiabatic expansion model involving synchrotron source components, to obtain spectral index values, expansion velocities, turnover frequencies and other parameters, which are consistent with previously published results from variability studies. An average time delay of 1.5 ± 0.5 hours between the NIR flares and the mm flares was obtained, with expansion velocities ranging from $0.005c$ - $0.017c$. The SSC model provides constraints for the turnover frequencies and flux

densities of the NIR flux density contributions from the synchrotron emission. The lower flux density limits obtained for the mm-regime also imply that the turnover frequencies cannot be lower than about 1.0 ± 0.3 THz and the optically thick peak flux densities at or below these turnover frequencies do not exceed about ~ 1 Jy on average. Previously reported flare detections have observed higher flux densities in the mm-regime (Yusef-Zadeh et al. 2009; Marrone et al. 2008; Eckart et al. 2008b, 2006a).

Further simultaneous monitoring of Sgr A* at different wavelengths (from the higher energy X-ray/NIR to the radio/sub-mm) and in polarised NIR/radio emission are required to improve the statistics and to place better constraints to the models describing this flaring activity. The current crop of mm and sub-mm interferometers such as CARMA, PdBI, ATCA, SMA and VLBA and future telescope arrays such as ALMA, which can distinguish the emission of Sgr A* from the thermal emission of the surrounding CND and mini-spiral, in combination with NIR telescopes such as Keck, VLT and the upcoming LBT, which can distinguish Sgr A* from the stellar population surrounding it, should provide us with higher quality data.

Imaging of the central region of Sgr A* may become possible in the near future with long baseline mm-VLBI measurements at higher angular resolutions and frequencies (≥ 230 GHz) (Doeleman et al. 2008, 2009). In combination with polarimetric NIR interferometric observations with the GRAVITY instrument at VLTI (Eisenhauer et al. 2008; Zamaninasab et al. 2010) this will enable a deeper understanding of the SMBH at the centre of our galaxy, and allow us to test current theories of emission in the region.

Bibliography

- Allen, C. W. 1976, *Astrophysical Quantities*, ed. Allen, C. W.
- Allen, D. A., Hyland, A. R., & Hillier, D. J. 1990, *MNRAS*, 244, 706
- Baganoff, F. K., Bautz, M. W., Brandt, W. N., et al. 2001, *Nature*, 413, 45
- Baganoff, F. K., Maeda, Y., Morris, M., et al. 2003, *ApJ*, 591, 891
- Balick, B. & Brown, R. L. 1974, *ApJ*, 194, 265
- Becklin, E. E., Matthews, K., Neugebauer, G., & Willner, S. P. 1978, *ApJ*, 219, 121
- Becklin, E. E. & Neugebauer, G. 1975, *ApJL*, 200, L71
- Blum, R. D., Mould, J. R., Olsen, K. A., et al. 2006, *AJ*, 132, 2034
- Blum, R. D., Sellgren, K., & Depoy, D. L. 1996, *ApJ*, 470, 864
- Bock, D., Bolatto, A. D., Hawkins, D. W., et al. 2006, in *Society of Photo-Optical Instrumentation Engineers (SPIE) Conference Series*, Vol. 6267, Society of Photo-Optical Instrumentation Engineers (SPIE) Conference Series
- Bower, G. C., Falcke, H., Sault, R. J., & Backer, D. C. 2002, *ApJ*, 571, 843
- Brown, R. L., Johnston, K. J., & Lo, K. Y. 1981, *ApJ*, 250, 155
- Buchholz, R. M., Schödel, R., & Eckart, A. 2009, *A&A*, 499, 483
- Cardelli, J. A., Clayton, G. C., & Mathis, J. S. 1989, *ApJ*, 345, 245

- Christopher, M. H., Scoville, N. Z., Stolovy, S. R., & Yun, M. S. 2005, *ApJ*, 622, 346
- Cohen, M., Walker, R. G., Carter, B., et al. 1999, *AJ*, 117, 1864
- Cunningham, C. T. 1975, *ApJ*, 202, 788
- Devillard, N. 1997, *The Messenger*, 87, 19
- Diolaiti, E., Bendinelli, O., Bonaccini, D., et al. 2000, in *Society of Photo-Optical Instrumentation Engineers (SPIE) Conference Series*, Vol. 4007, Society of Photo-Optical Instrumentation Engineers (SPIE) Conference Series, ed. P. L. Wizinowich, 879–888
- Do, T., Ghez, A. M., Morris, M. R., et al. 2009, *ApJ*, 691, 1021
- Dodds-Eden, K., Porquet, D., Trap, G., et al. 2009, *ApJ*, 698, 676
- Doeleman, S. S., Fish, V. L., Broderick, A. E., Loeb, A., & Rogers, A. E. E. 2009, *ApJ*, 695, 59
- Doeleman, S. S., Weintraub, J., Rogers, A. E. E., et al. 2008, *Nature*, 455, 78
- Dovčiak, M., Karas, V., & Yaqoob, T. 2004, *The Astroph. Journal Supp. Ser.*, 153, 205
- Downes, D. & Martin, A. H. M. 1971, *Nature*, 233, 112
- Draine, B. T. & Lee, H. M. 1984, *ApJ*, 285, 89
- Eckart, A., Baganoff, F. K., Morris, M., et al. 2004, *A&A*, 427, 1
- Eckart, A., Baganoff, F. K., Morris, M. R., et al. 2009, *A&A*, 500, 935
- Eckart, A., Baganoff, F. K., Schödel, R., et al. 2006a, *A&A*, 450, 535
- Eckart, A., Baganoff, F. K., Zamaninasab, M., et al. 2008a, *A&A*, 479, 625
- Eckart, A. & Genzel, R. 1996, *Nature*, 383, 415
- Eckart, A., Genzel, R., Ott, T., & Schödel, R. 2002, *MNRAS*, 331, 917

- Eckart, A., Ott, T., Genzel, R., & Lutz, D. 1999, in IAU Symposium, Vol. 193, Wolf-Rayet Phenomena in Massive Stars and Starburst Galaxies, ed. K. A. van der Hucht, G. Koenigsberger, & P. R. J. Eenens, 449–+
- Eckart, A., Schödel, R., García-Marín, M., et al. 2008b, *A&A*, 492, 337
- Eckart, A., Schödel, R., Meyer, L., et al. 2006b, *A&A*, 455, 1
- Eisenhauer, F., Genzel, R., Alexander, T., et al. 2005, *ApJ*, 628, 246
- Eisenhauer, F., Perrin, G., Brandner, W., et al. 2008, in Society of Photo-Optical Instrumentation Engineers (SPIE) Conference Series, Vol. 7013, Society of Photo-Optical Instrumentation Engineers (SPIE) Conference Series
- Eisenhauer, F., Schödel, R., Genzel, R., et al. 2003, *ApJL*, 597, L121
- Ekers, R. D., Fanti, R., & Miley, G. K. 1983, *A&A*, 120, 297
- Ekers, R. D., Goss, W. M., Schwarz, U. J., Downes, D., & Rogstad, D. H. 1975, *A&A*, 43, 159
- Falcke, H., Goss, W. M., Matsuo, H., et al. 1998, *ApJ*, 499, 731
- Fich, M. & Hodge, P. 1991, *ApJL*, 374, L17
- García-Marín, M., Eckart, A., Weiss, A., et al. 2010, ASP Conference series
- Genzel, R. 1996, in IAU Symposium, Vol. 174, Dynamical Evolution of Star Clusters: Confrontation of Theory and Observations, ed. P. Hut & J. Makino, 81–+
- Genzel, R., Eckart, A., Ott, T., & Eisenhauer, F. 1997, *MNRAS*, 291, 219
- Genzel, R., Pichon, C., Eckart, A., Gerhard, O. E., & Ott, T. 2000, *MNRAS*, 317, 348
- Genzel, R., Schödel, R., Ott, T., et al. 2003, *Nature*, 425, 934
- Gezari, D. & Yusef-Zadeh, F. 1991, in Astronomical Society of the Pacific Conference Series, Vol. 14, Astronomical Society of the Pacific Conference Series, ed. R. Elston, 214–218

- Ghez, A., Morris, M., Lu, J., et al. 2009, in *Astronomy*, Vol. 2010, *AGB Stars and Related Phenomena* 2010: The Astronomy and Astrophysics Decadal Survey, 89–+
- Ghez, A. M., Duchêne, G., Matthews, K., et al. 2003, *ApJL*, 586, L127
- Ghez, A. M., Hornstein, S. D., Bouchez, A., et al. 2004a, in *Bulletin of the American Astronomical Society*, Vol. 36, *Bulletin of the American Astronomical Society*, 1384–+
- Ghez, A. M., Klein, B. L., Morris, M., & Becklin, E. E. 1998, *ApJ*, 509, 678
- Ghez, A. M., Morris, M., Becklin, E. E., Tanner, A., & Kremenek, T. 2000, *Nature*, 407, 349
- Ghez, A. M., Salim, S., Hornstein, S. D., et al. 2005, *ApJ*, 620, 744
- Ghez, A. M., Salim, S., Weinberg, N. N., et al. 2008, *ApJ*, 689, 1044
- Ghez, A. M., Wright, S. A., Matthews, K., et al. 2004b, *ApJL*, 601, L159
- Gillessen, S., Eisenhauer, F., Trippe, S., et al. 2009, *ApJ*, 692, 1075
- Glass, I. S. 1999, *Handbook of Infrared Astronomy*, ed. Glass, I. S.
- Goss, W. M., Brown, R. L., & Lo, K. Y. 2003, *Astronomische Nachrichten Supplement*, 324, 497
- Gould, R. J. 1979, *A&A*, 76, 306
- Guesten, R., Genzel, R., Wright, M. C. H., et al. 1987, *ApJ*, 318, 124
- Herrnstein, R. M. & Ho, P. T. P. 2005, *ApJ*, 620, 287
- Herrnstein, R. M., Zhao, J., Bower, G. C., & Goss, W. M. 2004, *AJ*, 127, 3399
- Hildebrand, R. H. 1983, *Royal Astron. Soc. Quart. Jrn.*, 24, 267
- Ho, P. T. P., Beck, S. C., & Turner, J. L. 1990, *ApJ*, 349, 57
- Högbom, J. A. 1974, *A&A Supplement*, 15, 417
- Jansky, K. G. 1933, *Nature*, 132, 66

- Krabbe, A., Genzel, R., Eckart, A., et al. 1995, *ApJL*, 447, L95+
- Kunneriath, D., Eckart, A., Vogel, S., et al. 2008, *Journal of Physics Conference Series*, 131, 012006
- Kunneriath, D., Eckart, A., Zamaninasab, M., et al. 2010, *ASP Conference series*
- Lagage, P., Pel, J., Claret, A., et al. 2003, in *Society of Photo-Optical Instrumentation Engineers (SPIE) Conference Series*, Vol. 4841, *Society of Photo-Optical Instrumentation Engineers (SPIE) Conference Series*, ed. M. Iye & A. F. M. Moorwood, 923–931
- Latvakoski, H. M., Stacey, G. J., Gull, G. E., & Hayward, T. L. 1999, *ApJ*, 511, 761
- Lenzen, R., Hartung, M., Brandner, W., et al. 2003, in *Society of Photo-Optical Instrumentation Engineers (SPIE) Conference Series*, Vol. 4841, *Society of Photo-Optical Instrumentation Engineers (SPIE) Conference Series*, ed. M. Iye & A. F. M. Moorwood, 944–952
- Lo, K. Y. & Claussen, M. J. 1983, *nat*, 306, 647
- Lu, R., Krichbaum, T. P., Eckart, A., et al. 2008, *Journal of Physics Conference Series*, 131, 012059
- Lu, R., Krichbaum, T. P., Eckart, A., et al. 2010, *A & A*, accepted
- Lynden-Bell, D. 1969, *Nature*, 223, 690
- Lynden-Bell, D. & Rees, M. J. 1971, *MNRAS*, 152, 461
- Maness, H., Martins, F., Trippe, S., et al. 2007, *ApJ*, 669, 1024
- Markoff, S., Bower, G. C., & Falcke, H. 2007, *MNRAS*, 379, 1519
- Markoff, S., Falcke, H., Yuan, F., & Biermann, P. L. 2001, *A&A*, 379, L13
- Markoff, S., Nowak, M. A., & Wilms, J. 2005, *ApJ*, 635, 1203
- Marrone, D. P., Baganoff, F. K., Morris, M. R., et al. 2008, *ApJ*, 682, 373
- Marscher, A. P. 1983, *ApJ*, 264, 296

- Mauerhan, J. C., Morris, M., Walter, F., & Baganoff, F. K. 2005, *ApJL*, 623, L25
- Meyer, L., Do, T., Ghez, A., et al. 2008, *ApJL*, 688, L17
- Meyer, L., Schödel, R., Eckart, A., et al. 2006, *A&A*, 458, L25
- Mezger, P. G., Zylka, R., Salter, C. J., et al. 1989, *A&A*, 209, 337
- Montero-Castaño, M., Herrnstein, R. M., & Ho, P. T. P. 2006, *Journal of Physics Conference Series*, 54, 29
- Montero-Castaño, M., Herrnstein, R. M., & Ho, P. T. P. 2009, *ApJ*, 695, 1477
- Moultaka, J., Eckart, A., Schödel, R., Viehmann, T., & Najarro, F. 2005, *A&A*, 443, 163
- Mužić, K., Schödel, R., Eckart, A., Meyer, L., & Zensus, A. 2008, *A&A*, 482, 173
- Narayan, R., Mahadevan, R., Grindlay, J. E., Popham, R. G., & Gammie, C. 1998, *ApJ*, 492, 554
- Narayan, R. & McClintock, J. E. 2008, *New Astron. Rev.*, 51, 733
- Narayan, R., Yi, I., & Mahadevan, R. 1995, *Nature*, 374, 623
- Neugebauer, G., Becklin, E. E., Matthews, K., & Wynn-Williams, C. G. 1978, *ApJ*, 220, 149
- Panagia, N. & Walmsley, C. M. 1978, *A&A*, 70, 411
- Paumard, T., Maillard, J. P., Morris, M., & Rigaut, F. 2001, *A&A*, 366, 466
- Pecháček, T., Karas, V., & Czerny, B. 2008, *A&A*, 487, 815
- Porquet, D., Predehl, P., Aschenbach, B., et al. 2003, *aap*, 407, L17
- Reid, M. J. 1993, *Ann. Rev. Astron. Astrophys.*, 31, 345
- Rieke, G. H., Telesco, C. M., & Harper, D. A. 1978, *ApJ*, 220, 556

- Roberts, D. A., Goss, W. M., van Gorkom, J. H., & Leahy, J. P. 1991, *ApJL*, 366, L15
- Roberts, D. A., Yusef-Zadeh, F., & Goss, W. M. 1996, *ApJ*, 459, 627
- Rousset, G., Lacombe, F., Puget, P., et al. 2003, in *Society of Photo-Optical Instrumentation Engineers (SPIE) Conference Series*, Vol. 4839, *Society of Photo-Optical Instrumentation Engineers (SPIE) Conference Series*, ed. P. L. Wizinowich & D. Bonaccini, 140–149
- Sabha, N., Witzel, G., Eckart, A., et al. 2010, *A&A*, 512, A2+
- Schödel, R. 2010, *A&A*, 509, A58+
- Schödel, R., Eckart, A., Mužić, K., et al. 2007, *A&A*, 462, L1
- Schödel, R., Najarro, F., Muzic, K., & Eckart, A. 2009, *ArXiv e-prints*
- Schödel, R., Najarro, F., Muzic, K., & Eckart, A. 2010, *A&A*, 511, A18+
- Schödel, R., Ott, T., Genzel, R., et al. 2003, *ApJ*, 596, 1015
- Schödel, R., Ott, T., Genzel, R., et al. 2002, *Nature*, 419, 694
- Schwarz, U. J. 1978, *A&A*, 65, 345
- Scoville, N. Z., Stolovy, S. R., Rieke, M., Christopher, M., & Yusef-Zadeh, F. 2003, *ApJ*, 594, 294
- Shukla, H., Yun, M. S., & Scoville, N. Z. 2004, *ApJ*, 616, 231
- Tanner, A., Ghez, A. M., Morris, M., et al. 2002, *ApJ*, 575, 860
- Telesco, C. M., Davidson, J. A., & Werner, M. W. 1996, *ApJ*, 456, 541
- Trippe, S., Paumard, T., Ott, T., et al. 2007, *MNRAS*, 375, 764
- Tsuboi, M., Miyazaki, A., & Tsutsumi, T. 1999, in *Astronomical Society of the Pacific Conference Series*, Vol. 186, *The Central Parsecs of the Galaxy*, ed. H. Falcke, A. Coter, W. J. Duschl, F. Melia, & M. J. Rieke, 105–+
- Tsutsumi, T., Kawabata, T., Miyazaki, A., & Tsuboi, M. 1998, in *IAU Symposium*, Vol. 184, *The Central Regions of the Galaxy and Galaxies*, ed. Y. Sofue, 439–+

- van der Laan, H. 1966, *Nature*, 211, 1131
- Wilson, T. L., Rohlfs, K., & Hüttemeister, S. 2009, *Tools of Radio Astronomy*, ed. Wilson, T. L., Rohlfs, K., Hüttemeister, S. (Springer-Verlag)
- Wright, M. C. H. & Backer, D. C. 1993, *apj*, 417, 560
- Wright, M. C. H., Genzel, R., Güsten, R., & Jaffe, D. T. 1987, in *American Institute of Physics Conference Series*, Vol. 155, *The Galactic Center*, ed. D. C. Backer, 133–137
- Yuan, F., Quataert, E., & Narayan, R. 2003, *ApJ*, 598, 301
- Yusef-Zadeh, F., Bushouse, H., Dowell, C. D., et al. 2006a, *ApJ*, 644, 198
- Yusef-Zadeh, F., Bushouse, H., Wardle, M., et al. 2009, *ApJ*, 706, 348
- Yusef-Zadeh, F., Roberts, D., Wardle, M., Heinke, C. O., & Bower, G. C. 2006b, *ApJ*, 650, 189
- Yusef-Zadeh, F., Wardle, M., Heinke, C., et al. 2008, *ApJ*, 682, 361
- Zamaninasab, M., Eckart, A., Meyer, L., et al. 2008, *Journal of Physics Conference Series*, 131, 012008
- Zamaninasab, M., Eckart, A., Witzel, G., et al. 2010, *A&A*, 510, A3+
- Zhao, J., Blundell, R., Moran, J. M., et al. 2010, *ArXiv e-prints*
- Zhao, J., Goss, W. M., Lo, K., & Ekers, R. D. 1992, in *Astronomical Society of the Pacific Conference Series*, Vol. 31, *Relationships Between Active Galactic Nuclei and Starburst Galaxies*, ed. A. V. Filippenko, 295–+
- Zhao, J., Herrnstein, R. M., Bower, G. C., Goss, W. M., & Liu, S. M. 2004, *ApJL*, 603, L85
- Zhao, J., Morris, M. R., Goss, W. M., & An, T. 2009, *ApJ*, 699, 186
- Zhao, J., Young, K. H., Herrnstein, R. M., et al. 2003, *ApJL*, 586, L29
- Zhao, J., Young, K. H., McGary, R. S., et al. 2001, in *Bulletin of the American Astronomical Society*, Vol. 33, *Bulletin of the American Astronomical Society*, 1475–+
- Zylka, R. & Mezger, P. G. 1988, *A&A*, 190, L25

List of Figures

1.1	Greenbank telescope	10
1.2	Schematic view of GC region	11
1.3	Sgr A Complex at 6 cm	12
1.4	HCN emission from circum nuclear Disk	13
1.5	Mini-spiral at 3.6 and 1.3 cm	14
1.6	NIR HKL composite of GC stellar cluster	16
1.7	SED of Sgr A*	17
1.8	Simultaneous NIR and X-ray light curves of Sgr A*	18
1.9	Simultaneous NIR and sub-mm light curves of Sgr A*	19
2.1	Transmission windows of Earth's atmosphere	22
2.2	Free-free emission spectrum	24
2.3	Synchrotron spectrum	25
2.4	Two element interferometer	28

2.5	Sketch of an extended source in the sky	29
2.6	uv coverage	30
2.7	CARMA array	32
2.8	ATCA array	33
2.9	MAMBO bolometer	34
2.10	VLT array	35
3.1	3 mm C array map, May 2009	39
3.2	MIR map of GC region	40
3.3	Br γ map of GC region	41
3.4	Point source subtracted Br γ map of GC region	42
3.5	Selection of sources in mini-spiral	43
3.6	1.3 mm map of GC region	45
3.7	Spectral index map of mini-spiral and Sgr A*	47
3.8	Excess emission in 1.3 mm	49
3.9	MIR map of GC region overlaid with 3 mm contours	51
3.10	Dust to gas ratio map of GC region	52
3.11	A_K extinction map of GC region	54
4.1	Simulated images from relativistic spot/disk modelling	60
4.2	Simulated NIR light curves from relativistic spot/disk modelling	60

4.3	Flux behaviour in adiabatic expansion model	62
5.1	3 mm combined BCD array map	67
5.2	Combined differential mm/sub-mm light curve	70
5.3	Mean map at 3 mm from May 16-19, 2007	72
5.4	Residual maps at 3 mm for May 16-19, 2007	72
5.5	NIR K and L'-band light curve for May 15, 2007	75
5.6	NIR K and L'-band light curve for May 16, 2007	75
5.7	NIR K and L'-band light curve for May 17, 2007	76
5.8	NIR L'-band light curve for May 18, 2007	76
5.9	NIR K-band light curve for May 19, 2007	77
5.10	Model fits for light curves of May 15, 2007	81
5.11	Cross-correlation of NIR and mm light curves, May 17, 2007	84
5.12	Cross-correlation of Sgr A* and calibrator light curves, May 17, 2007	85
5.13	Model fits for light curves of May 17, 2007	87
5.14	Model fits for light curves of May 19, 2007	89
5.15	NIR and mm light curves for May 26, 2008	91
5.16	Model fits for light curves of May 26, 2008	92

List of Tables

3.1	Log of the mm, NIR and MIR observations.	38
3.2	Sgr A* fluxes at 3 and 1.3 mm	39
3.3	Fluxes and calculated properties of selected mini-spiral regions	55
5.1	Log of the mm- and sub-mm observations.	68
5.2	Log of the near-infrared observations.	74
5.3	Model parameters for May 15, 2007	82
5.4	Model parameters for May 17, 2007	86
5.5	Model parameters for May 19, 2007	90
5.6	Model parameters for May 26, 2008	93

List of Acronyms

A_K	Extinction in K-band
A_V	Extinction in visual band
ADAF	Advection Dominated Accretion Flow
AGB	Asymptotic Giant Branch
AO	Adaptive Optics
ATCA	Australia Telescope Compact Array
ATNF	Australia Telescope National Facility
CARMA	Combined Array for Research in Mm-wave Astronomy
CND	CircumNuclear Disk
CONICA	High Resolution IR Camera and Spectrometer
DIT	Detector Integration Time
EM	Emission Measure
ESO	European Southern Observatory
FOV	Field of View
FWHM	Full Width at Half Maximum
GC	Galactic Center
GRAVITY	General Relativity Analysis via VLT InTerferometrY
IC	Inverse Compton
IR	InfraRed
ISM	InterStellar Medium
IRAM	Institute for RadioAstronomy at Millimeter wavelengths
JD	Julian Date
Keck	W. M. Keck Observatory, two 10m telescopes
LR	Lucy-Richardson
MAMBO	MAx-Planck Millimeter BOLometer
MIR	Mid-InfraRed

NACO	NAOS/CONICA adaptive optics device/near-infrared camera at the VLT
NAOS	Nasmyth Adaptive Optics System
NDIT	Number of DIT's
NICMOS	Near Infrared Camera and Multi-Object Spectrometer (on board of the HST)
NIR	Near-InfraRed
NRAO	National Radio Astronomy Observatory
OVRO	Owens Valley Radio Observatory
PSF	Point Spread Function
QPO	Quasi-Periodic Oscillation
SED	Spectral Energy Distribution
Sgr A*	Sagittarius A*
SMBH	SuperMassive Black Hole
SNR	Signal to Noise Ratio
SSC	Synchrotron Self Compton
UT	Universal Time
VISIR	VLT Spectrometer and Imager for the mid-InfraRed
VLA	Very Large Array
VLBA	Very Long Baseline Array
VLBI	Very Long Baseline Interferometry
VLT	Very Large Telescope
VLTI	Very Large Telescope Interferometry
ZDCF	z-transformed Discrete Correlation Function

Acknowledgements

I am very grateful to my supervisor Prof. Andreas Eckart, for his support and guidance. Thank you for giving me this opportunity.

This work was financially supported by the International Max Planck Research School (IMPRS) for Astronomy and Astrophysics at the MPIfR and the Universities of Bonn and Cologne. I would like to thank Prof. Zensus for his support and encouragement, Prof. Eduardo Ros and Gabi Breuer, former coordinator and secretary of the IMPRS program for their help in sorting out every problem I faced in the first two years, and Dr. Manolis Angelakis and Simone Pott, current coordinator and secretary of the IMPRS program.

My sincerest thanks to my mentor Prof. G. Srinivasan, without whose constant support, encouragement and guidance over the last decade, I wouldn't be here today.

Many thanks to Macarena Garcia-Marin for reading and correcting my thesis, and for her general guidance and support, and Rainer Schoedel, for his always excellent advice and constant encouragement.

To the current and former members of aegroup: Thank you for providing an excellent working atmosphere and for the fun mensa lunches and group dinners. I would like to thank Christian Straubmeier, Jens Zuther, Sebastian Fischer and Steffen Rost for providing computer support. I would also like to thank the Ph1 secretaries for their help with everything.

To all the lovely friends I made at Ph1- Kora, Mohammad, Gunther, Nadeen, Monica, Maca, Sabine, Marcus, Senol, Lilia, Constanza, Maryam, Jihane, Miguel, Leo and Rene: Thank you for all the fun times!

Many many thanks to Monica, Nadeen, Gunther, Senol and Marcus for their help with the thesis, and to baby Marcos, for letting Maca read my

thesis.

Many thanks to Dr.Gangadharan and his wonderful team at Lakeshore.

To the former inhabitants (Kora Kora and Momo) of the Republic of Montenegro and Gunther: Thank you for everything.

To Shincy: For everything you've done for me right from day one in Germany, and all the fun times in Bonn, thank you!

To the former girls' office inhabitants (Monik, Sabine and Nadeen): Thanks for all the fun times and the endless supply of coffee and cookies!

To my friends from India- Reks, Sushila, Rashmi Verma, Arjun, Shirin, Kiran and Winnie: Thank you for your love and encouragement.

To Cindu C: Thank you for the phone calls, and the love and support.

To Dhananjay Anand (Dj): Thank you for the long distance support, and for not letting timezones, visas and Justvoip troubles get in the way.

To my lovely family- Amma, Achan, Dimpu and Sabacca: Thank you for the endless love and unconditional support. I love you.

Erklärung

Ich versichere, daß ich die von mir vorgelegte Dissertation selbständig angefertigt, die benutzten Quellen und Hilfsmittel vollständig angegeben und die Stellen der Arbeit – einschließlich Tabellen, Karten und Abbildungen –, die anderen Werken im Wortlaut oder dem Sinn nach entnommen sind, in jedem Einzelfall als Entlehnung kenntlich gemacht habe; daß diese Dissertation noch keiner anderen Fakultät oder Universität zur Prüfung vorgelegen hat; daß sie – abgesehen von unten angegebenen Teilpublikationen – noch nicht veröffentlicht worden ist sowie, daß ich eine solche Veröffentlichung vor Abschluß des Promotionsverfahrens nicht vornehmen werde. Die Bestimmungen dieser Promotionsordnung sind mir bekannt. Die von mir vorgelegte Dissertation ist von Prof. Dr. Andreas Eckart betreut worden.

Köln, 27. 09. 2010

Teilpublikationen

- **Kunneriath, D.**, Witzel, G., Eckart, A., Zamaninasab, M., Gießübel, R., Schödel, R., Baganoff, F.K., Morris, M. R., Dovciak, M., Duschl, W.J., García-Marín, M., Karas, V., König, S., Krichbaum, T. P., Krips, M., Lu, R.-S., Mauerhan, R., Moutaka, J., Muzic, K., Sabha, N., Najarro, F., Pott, J.-U., Schuster, K. F., Sjouwerman, L. O., Straubmeier, C., Thum, C., Vogel, S. N., Teuben, P., Weiss, A., Wiesemeyer, H., Zensus, J. A.: "*Coordinated NIR/mm observations of flare emission from Sagittarius A**",

A&A 517, A46 (2010) [arXiv:1008.1560v1].

• **Kunneriath, D.**, Eckart, A., Zamaninasab, M., Witzel, G., Schödel, R., García-Marín, M., König, S., Krichbaum, T. P., Lu, R.-S., Moutaka, J., Mužić, K., Sabha, N., Sjouwerman, L., Straubmeier, C., Vogel, S., Teuben, P. and Zensus, A.: "*The Galactic Centre in the mm-regime: Observations with CARMA*", to be published in "The Galactic Center: a Window to the Nuclear Activity of Disk Galaxies", eds. Mark Morris et al., Astron. Soc. Pacific, 2010.

• **Kunneriath, D.**, Eckart, A., Vogel, S., Sjouwerman, L., Wiesemeyer, H., Schödel, R., Baganoff, F. K., Morris, M., Bertram, T., Dovciak, M., Dowries, D., Duschl, W. J., Karas, V., König, S., Krichbaum, T., Krips, M., Lu, R.-S., Markoff, S., Mauerhan, J., Meyer, L., Moutaka, J., Muzic, K., Najarro, F., Schuster, K., Straubmeier, C., Thum, C., Witzel, G., Zamaninasab, M., Zensus, A.: "*Coordinated mm/sub-mm observations of Sagittarius A* in May 2007*", JoP: Conference Series, Volume 131, Issue 1, 2008.

Weitere Publikationen

• Zamaninasab, M., Eckart, A., Witzel, G., Dovciak, M., Karas, V., Schödel, R., Gießübel, R., Bremer, M., García-Marín, M., **Kunneriath, D.**, Mužić, K., Nishiyama, S., Sabha, N., Straubmeier, C. and Zensus, A.: "*Near Infrared Flares of Sagittarius A*: Importance of Near Infrared Polarimetry*", A&A 510, A3 (2010) [arXiv:0911.4659].

• Sabha, N., Witzel, G., Eckart, A., Buchholz, R. M., Bremer, M., Gießübel, R., García-Marín, M., **Kunneriath, D.**, Muzic, K., Schödel, R., Straubmeier, C., Zamaninasab, M., and Zernickel, A.: "*The Extreme Luminosity States of Sagittarius A**", A&A, 512, A2 (2010) [arXiv:1001.1351].

- García-Marín, M., Eckart, A., Weiss, A., Witzel, G., Bremer, M., Zamaninasab, M., Morris, M. R., Schödel, R., **Kunneriath, D.**, Nishiyama, S., Baganoff, F., Dovciak, M., Sabha, N., Duschl, W. J., Moulataka, J., Karas, V., Najarro, F., Muzic, K., Straubmeier, C., Vogel, S., Krips, M., and Wiesemeyer, H.: *"Extended sub-mm emission of the Galactic center and NIR/sub-mm variability of its super-massive black hole"*, submitted to ApJ.

- Eckart, A., Baganoff, F. K., Morris, M. R., **Kunneriath, D.**, Zamaninasab, M., Witzel, G., Schödel, R., García-Marín, M., Meyer, L., Bower, G. C., Marrone, D., Bautz, M. W., Brandt, W. N., Garmire, G. P., Ricker, G. R., Straubmeier, C., Roberts, D. A., Mužić, K., Mauerhan, J. and Zensus, A.: *"Modeling mm- to X-ray flare emission from Sagittarius A*"*, A&A 500, 3, 2009.

- Eckart, A., Schödel, R., García-Marín, M., Witzel, G., Weiss, A., Baganoff, F. K., Morris, M. R., Bertram, T., Dovciak, M., Duschl, W. J., Karas, V., König, S., Krichbaum, T. P., Krips, M., **Kunneriath, D.**, Lu, R.-S., Markoff, S., Mauerhan, J., Meyer, L., Moulataka, J., Mužić, K., Najarro, F., Pott, J.-U., Schuster, K. F., Sjouwerman, L. O., Straubmeier, C., Thum, C., Vogel, S. N., Wiesemeyer, H., Zamaninasab, M., Zensus, J. A.: *"Simultaneous NIR/sub-mm observation of flare emission from Sagittarius A*"*, A&A 492, 2, 2009.

- Eckart, A., Baganoff, F. K., Zamaninasab, M., Morris, M. R., Schödel, R., Meyer, L., Muzic, K., Bautz, M. W., Brandt, W. N., Garmire, G. P., Ricker, G. R., **Kunneriath, D.**, Straubmeier, C., Duschl, W., Dovciak, M., Karas, V., Markoff, S., Najarro, F., Mauerhan, J., Moulataka, J., Zensus, A.: *"Polarized NIR and X-ray flares from Sagittarius A*"*, A&A 479, 3, 2008.

- Lu, R.-S., Krichbaum, T. P., Eckart, A., König, S., **Kunneriath, D.**, Witzel, G., Witzel, A., Zensus, J. A.: *"High-frequency VLBI observations of Sgr A* during a multi-frequency campaign in May 2007"*, JoP: Conference

Series, Volume 131, Issue 1, 2008.

- Zamaninasab, M., Eckart, A., Witzel, G., Dovciak, M., Karas, V., Schödel, R., Gießübel, R., Bremer, M., García-Marín, M., **Kunneriath, D.**, Mužić, K., Nishiyama, S., Sabha, N., Straubmeier, C. and Zensus, A.: "*Near infrared polarimetry as a tool for testing the properties of radiation from Sagittarius A**", to be published in "The Galactic Center: a Window to the Nuclear Activity of Disk Galaxies", eds. Mark Morris et al., Astron. Soc. Pacific, 2010.

- Zamaninasab, M., Eckart, A., Meyer, L., Schödel, R., Dovciak, M., Karas, V., **Kunneriath, D.**, Witzel, G., Gießübel, R., König, S., Straubmeier, C., Zensus, A.: "*An evolving hot spot orbiting around Sgr A**", JoP: Conference Series, Volume 131, Issue 1, 2008.

- Zamaninasab, M., Eckart, A., **Kunneriath, D.**, Witzel, G., Schödel, R., Meyer, L., Dovciak, M., Karas, V., König, S., Krichbaum, T., Lu, R. S., Straubmeier, C., Zensus, J. A.: "*Flares of Sgr A*: from X-ray to mm*", Memorie della Societa Astronomica Italiana, volume 79, 1054, 2008.

- Eckart, A., Schödel, R., Baganoff, F. K., Morris, M., Bertram, T., Dovciak, M., Dowries, D., Duschl, W. J., Karas, V., König, S., Krichbaum, T., Krips, M., **Kunneriath, D.**, Lu, R.-S., Markoff, S., Mauerhan, J., Meyer, L., Moutaka, J., Muzic, K., Najarro, F., Schuster, K., Sjouwerman, L., Straubmeier, C., Thum, C., Vogel, S., Wiesemeyer, H., Witzel, G., Zamaninasab, M., Zensus, A.: "*Coordinated multi-wavelength observations of Sgr A**", JoP: Conference Series, Volume 131, Issue 1, 2008.

- Eckart, A., Schödel, R., García-Marín, M., Witzel, G., Weiss, A., Baganoff, F., Morris, M. R., Bertram, T., Dovciak, M., Downes, D., Duschl, W., Karas, V., König, S., Krichbaum, T., Krips, M., **Kunneriath, D.**, Lu, R.-S., Markoff, S., Mauerhan, J., Meyer, L., Moutaka, J., Muzic, K., Najarro, F., Pott, J.-U., Schuster, K., Sjouwerman, L., Straubmeier,

C., Thum, C., Vogel, S., Wiesemeyer, H., Zamaninasab, M., Zensus, A.: *"Probing Sagittarius A* and its Environment at the Galactic Centre: VLT and APEX Working in Synergy"*, The Messenger, vol. 133, 2008.

- Eckart, A., Witzel, G., **Kunneriath, D.**, König, S., Straubmeier, C., Bertram, T., Zamaninasab, M., Schödel, R., Muzic, K., Tremou, E., Meyer, L., Rost, S., Vogel, S., Wiesemeyer, H., Sjouwerman, L., Herbst, T.: *"Prospects for observing the Galactic Center: combining LBT LINC-NIRVANA observations in the near-infrared with observations in the mm/sub-mm wavelength domain"*, Optical and Infrared Interferometry: Proceedings of the SPIE Conference, Volume 7013, 70134L-70134L-12, 2008.

- Eckart, A., García-Marín, M., Witzel, G., König, S., **Kunneriath, D.**, Straubmeier, C., Zamaninasab, M.: *"Coordinated multi-wavelength observations of the Dark Mass at the Center of the Milky Way"*, Proceedings of "Identification of dark matter 2008". Stockholm, Sweden, 38, 2008.

Lebenslauf

Persönliche Angaben

Name: Devaky Kunneriath
Anschrift: I. Physikalisches Institut, Universität zu Köln
Zülpicher Str. 77, 50937 Köln
Email: devaky@ph1.uni-koeln.de
Geburtsdatum und -ort: 17.03.1983 in Ernakulam, Kerala, Indien

Ausbildung

Seit Mai 2007 Promotionstudentin an der Universität zu Köln und dem
Max-Planck-Institut für Radioastronomie
wiss. Betreuer: Prof. Dr. Andreas Eckart
2004 - 2006 Master der Physik an der Annamalai University,
Chidambaram, India
2000 - 2003 Bachelor der Physik an der St. Joseph's College of Arts and Science,
Bangalore, India
1989 - 2000 SBOA Public School
Ernakulam, India

Stipendium

Seit Mai 2007 Stipendium der *International Max Planck Research School (IMPRS)*
for Astronomy and Astrophysics